

$b\bar{b}$ PRODUCTION IN $p + p$ COLLISIONS AT $\sqrt{s} = 510$ GeV
IN THE PHENIX DETECTOR AT RHIC

by

TRISTAN OLIVER SCOTT HASELER

Under the Direction of Xiaochun He, Ph.D. and Murad Sarsour, Ph.D.

ABSTRACT

Heavy flavor quarks are an important probe of the initial state of the Quark Gluon Plasma formed in heavy-ion collisions. Bottom and charm quarks are produced early in the collision, primarily through hard interactions, and experience the full time evolution of the medium. Understanding bottom quark production in $p + p$ collisions gives a baseline reference for studying larger collision systems. The measurement of the $b\bar{b}$ cross section can directly test pQCD predictions and $\Delta\phi$ correlations gives insight into the b quark production mechanisms.

The $b\bar{b}$ signal can be isolated by taking advantage of the properties of B^0 oscillations in the invariant mass region of 5-10 GeV. Measuring like-sign dimuons within this mass range provides an enriched bottom signal with a minimal amount of open charm background and

without any contributions from quarkonia or Drell-Yan pairs. $b\bar{b}$ will be measured through the semi-leptonic decay like-sign dimuon signal, in the rapidity range $1.2 < |y| < 2.2$ and at $\sqrt{s} = 510$ GeV from data recorded in 2013 at the PHENIX experiment. The measured total cross section is $\sigma_{b\bar{b}} = 14.9 \pm 0.7(stat) \pm 2.0(type\ B\ sys.) \pm 3.4(type\ C\ sys.)[\mu b]$.

INDEX WORDS: nuclear physics, RHIC, PHENIX, heavy flavor, bottom quark, $p + p$, dimuon, cross section, correlations

$b\bar{b}$ PRODUCTION IN $p + p$ COLLISIONS AT $\sqrt{s} = 510$ GeV
IN THE PHENIX DETECTOR AT RHIC

by

TRISTAN OLIVER SCOTT HASELER

A Dissertation Submitted in Partial Fulfillment of the Requirements for the Degree of

Doctor of Philosophy

in the College of Arts and Sciences

Georgia State University

2018

Copyright by
Tristan Oliver Scott Haseler
2018

$b\bar{b}$ PRODUCTION IN $p + p$ COLLISIONS AT $\sqrt{s} = 510$ GeV
IN THE PHENIX DETECTOR AT RHIC

by

TRISTAN OLIVER SCOTT HASELER

Committee Co-Chair:	Xiaochun He
Committee Co-Chair:	Murad Sarsour
Committee:	Megan Connors
	Steven Manson
	Russel White

Electronic Version Approved:

Office of Graduate Studies

College of Arts and Sciences

Georgia State University

August 2018

DEDICATION

To my parents.

ACKNOWLEDGMENTS

I would like to thank my advisors, Dr. Xiaochun He and Dr. Murad Sarsour for their steady guidance and encouragement over the years. They brought me into the field of High Energy Nuclear Physics, taught me the necessary skills needed to thrive and helped me become a successful scientist. It has been a pleasure to be a member of the Nuclear Physics Group at Georgia State University for the past five years under their advisement. I would also like to thank the many GSU Nuclear Physics Group Members that I have had the pleasure of calling my fellow colleagues and friends. My committee: Dr. Megan Connors, Dr. Steven Manson and Dr. Russel White for their insightful conversation and challenging questions about my thesis and defense. Finally, I would like to thank the PHENIX collaboration for their many comments and suggestions on my work.

TABLE OF CONTENTS

ACKNOWLEDGMENTS	v
LIST OF TABLES	ix
LIST OF FIGURES	x
LIST OF ABBREVIATIONS	xviii
1 INTRODUCTION	1
1.1 The Standard Model	2
1.2 Heavy Flavor Physics	5
1.2.1 <i>Heavy Flavor Production</i>	5
1.2.2 <i>Heavy Flavor Fragmentation</i>	7
1.2.3 <i>Bottom Physics</i>	8
1.3 Quark Gluon Plasma	10
1.4 $b\bar{b}$ Measurement	14
2 EXPERIMENT	19
2.1 RHIC	19
2.2 PHENIX	23
2.2.1 <i>Beam Beam Counter</i>	25
2.2.2 <i>Muon Arm Detectors</i>	27
2.2.3 <i>Data Acquisition and Processing</i>	32
3 DATA ANALYSIS	39
3.1 Dataset	39
3.1.1 <i>Quality and Assurance</i>	40
3.1.2 <i>Data Quality and Assurance Cuts</i>	41
3.1.3 <i>Acceptance and Reconstruction Efficiency</i>	56

3.2 Signal Extraction	59
<i>3.2.1 Combinatorial Background</i>	59
<i>3.2.2 Hadronic Background</i>	66
4 SYSTEMATIC UNCERTAINTIES	72
4.1 Acceptance and Reconstruction Efficiency	72
4.2 Muon Arm Detector Efficiencies	77
4.3 Signal Extraction	77
4.4 BBC Event Rate	78
4.5 Hadronic Background	81
4.6 Fit Function	85
4.7 Simulation Inputs: $\alpha(m)$ and β	85
<i>4.7.1 $\alpha(m)$</i>	86
<i>4.7.2 β</i>	87
4.8 BBC Efficiency	88
4.9 Scale Factor	88
5 RESULTS	90
5.1 Differential Cross Section	91
<i>5.1.1 Mass dependence</i>	91
<i>5.1.2 Event Rate dependence</i>	93
<i>5.1.3 $\Delta\phi$ Dependence</i>	95
5.2 Total Cross Section	96
6 SUMMARY	101
Appendices	102
A Kinematics	103
<i>1 Transverse Momentum, p_T</i>	103
<i>2 Invariant Mass, m</i>	103

<i>3</i>	<i>Rapidity, y and Pseudorapidity, η</i>	103
B	PHENIX CVS code locations	105
C	List of Runs Used	106
D	PYTHIA 6 Tune A Hadron Simulation Set Up	109
E	PYTHIA 8 MB Simulation Set Up	110
F	PYTHIA 6 J/ψ Embedding Simulation Set Up	111
REFERENCES		112

LIST OF TABLES

Table 1.1 Dominant physics processes that can contribute to dimuon signal in specified mass range and charge correlation.	16
Table 3.1 Event, track and dimuon selection cuts used for the second QA	41
Table 3.2 Event, track and dimuon selection cuts as determined with the J/ψ signal.	49
Table 3.3 Final event, track and dimuon selection cuts used in the analysis	55
Table 4.1 Summary of all systematic uncertainties	73
Table 4.2 Values of β as found using PYTHIA 6, PYTHIA 8 and MC@NLO	87
Table 4.3 Values of the scale factor as found using PYTHIA 6, PYTHIA 8 and MC@NLO	88
Table D.1 PYTHIA Tune A configuration used to extract hadronic contributions from MB simulation	109
Table F.1 PYTHIA 6 J/ψ configuration file used for the $A\epsilon$ embedding study.	111

LIST OF FIGURES

Figure 1.1 The elementary particles as described by the Standard Model [1].	3
Figure 1.2 Leading Order processes diagrams, collectively known as Pair Creation. From left to right is gluon fusion, quark fusion and gluon fusion with gluon emission.	6
Figure 1.3 Next to Leading Order processes diagrams. From left to right is flavor excitation, gluon splitting and flavor excitation with the emission of a gluon.	7
Figure 1.4 The flavor changing weak decay processes and their relative decay modes [2].	8
Figure 1.5 B^0 oscillation as understood in the Standard Model framework.	9
Figure 1.6 The history of the universe starting with the Big Bang on the left and the modern era on the right. The scale along the diagonal axis includes time, temperature and energy [3].	11
Figure 1.7 The QCD phase diagram. Baryon chemical potential versus temperature [4].	12
Figure 1.8 The heavy ion collision evolution from colliding species up to chemical freeze out.	13
Figure 1.9 pQCD calculations of $\sigma_{b\bar{b}}$ as a function of \sqrt{s} . The left side is 20-70 GeV and the right side is 20-14,000 GeV. The calculation has a central value and an associated error band based on calculation inputs [5].	15
Figure 1.10 Correlated muon pairs from the primary/secondary B decays. Here, B and \bar{B} are generic open bottom hadrons; X, Y, and X' are arbitrary decay products [6].	17
Figure 1.11 Correlated primary muon pairs from B^0 decays due to oscillations. Here, B is a generic open bottom hadron and B^0 can be either B_d^0 or B_s^0 ; X and X' are arbitrary decay products [6].	17
Figure 2.1 An aerial view of the RHIC complex at BNL. Overlaid on the picture are lines which the particles travel as they are produced and fed into the RHIC ring [7].	20

Figure 2.2 RHIC collision summary of all collision energies, species and their average store luminosity. The vast array of collision energies and species is unique to RHIC [8].	21
Figure 2.3 RHIC delivered luminosity of all polarized $p + p$ Runs [8].	23
Figure 2.4 The planned CAD Run 13 schedule as of May 3, 2013.	24
Figure 2.5 The PHENIX detector configuration for the 2012-2013 runs. The top panel is a view of the central arms as seen by looking along the axis of the beam direction. The bottom section highlights the two muon arms as seen from the side, perpendicular to the beam axis.	26
Figure 2.6 A drawing of one of the two BBC detectors.	27
Figure 2.7 A drawing of one of the two muon arm detectors. The three components can be seen, they are the MuTr (grey), MuID (green) and Muon Arm Magnet (yellow and magenta).	28
Figure 2.8 The field lines of the PHENIX magnet systems. The radial magnetic field can be seen in the Muon Arms.	29
Figure 2.9 The south arm MuTr system with a cutout showing the three stations within the Muon Magnet and the beam pipe going through the center. . . .	30
Figure 2.10 Schematic of Iarocci tubes used to makeup the MuID detector “two-pack”.	32
Figure 2.11 Layout of panels within the MuID detector	33
Figure 2.12 DAQ flow chart.	34
Figure 2.13 Diagram showing the definition of the DG0 and DDG0 cut parameters. The track coming from the left is from the MuTr and enters the MuID [9]. . .	38
Figure 3.1 DAQ status marked by shift leader.	42
Figure 3.2 Dimuon event rate for each run.	42
Figure 3.3 Dimuon mean p_T per run for the south arm (open blue circles) and for the north arm (closed red circles).	43
Figure 3.4 Dimuon mean y per run for the south arm (open blue circles) and for the north arm (closed red circles).	43

Figure 3.5 Dimuon mean mass per run for the south arm (open blue circles) and for the north arm (closed red circles).	44
Figure 3.6 Dimuon ratio (north/south) per run.	44
Figure 3.7 The mean of the single muon DG0 distributions for the north arm (closed red circles) and the south (open blue circles).	45
Figure 3.8 The mean of the single muon DDG0 distributions for the north arm (closed red circles) and the south (open blue circles).	45
Figure 3.9 The mean of the single muon χ_{vtx}^2 distributions for the north arm (closed red circles) and the south (open blue circles).	46
Figure 3.10 The mean of the single muon χ_{Tr}^2 distributions for the north arm (closed red circles) and the south (open blue circles).	46
Figure 3.11 The mean of the single muon N_{TrHits} distributions for the north arm (closed red circles) and the south (open blue circles).	47
Figure 3.12 The mean of the single muon N_{IDHits} distributions for the north arm (closed red circles) and the south (open blue circles).	47
Figure 3.13 The mean of the single muon p_z distribution for the north arm (closed red circles) and the south (open blue circles).	48
Figure 3.14 The ratio of J/ψ signal with DG0 cut to J/ψ signal without DG0 cut for the north arm (left) and south arm (right). The data are shown in solid black circles while the simulations are shown in empty red circles.	50
Figure 3.15 The ratio of J/ψ signal with DDG0 cut to J/ψ signal without DDG0 cut for the north arm (left) and south arm (right). The data are shown in solid black circles while the simulations are shown in empty red circles.	50
Figure 3.16 The ratio of J/ψ signal with χ_{Tr}^2 cut to J/ψ signal without χ_{Tr}^2 cut for the north arm (left) and south arm (right). The data are shown in solid black circles while the simulations are shown in empty red circles.	51
Figure 3.17 The ratio of J/ψ signal with χ_{ID}^2 cut to J/ψ signal without χ_{ID}^2 cut for the north arm (left) and south arm (right). The data are shown in solid black circles while the simulations are shown in empty red circles.	51
Figure 3.18 The ratio of J/ψ signal with N_{TrHits} cut to J/ψ signal without N_{TrHits} cut for the north arm (left) and south arm (right). The data are shown in solid black circles while the simulations are shown in empty red circles.	52

Figure 3.19 The ratio of J/ψ signal with N_{IDHits} cut to J/ψ signal without N_{IDHits} cut for the north arm (left) and south arm (right). The data are shown in solid black circles while the simulations are shown in empty red circles.	52
Figure 3.20 The ratio of J/ψ signal with p_z cut to J/ψ signal without p_z cut for the north arm (left) and south arm (right). The data are shown in solid black circles while the simulations are shown in empty red circles.	53
Figure 3.21 The ratio of J/ψ signal with single p_T cut to J/ψ signal without single p_T cut for the north arm (left) and south arm (right). The data are shown in solid black circles while the simulations are shown in empty red circles.	53
Figure 3.22 The ratio of J/ψ signal with χ_{vtx}^2 cut to J/ψ signal without χ_{vtx}^2 cut for the north arm (left) and south arm (right). The data are shown in solid black circles while the simulations are shown in empty red circles.	54
Figure 3.23 The ratio of J/ψ signal with dimuon p_T cut to J/ψ signal without dimuon p_T cut for the north arm (left) and south arm (right). The data are shown in solid black circles while the simulations are shown in empty red circles.	54
Figure 3.24 Input kinematics of dimuon generator simulation.	56
Figure 3.25 BBC_z vertex distribution from run number 397293.	57
Figure 3.26 Single and dimuon kinematic distributions comparison between data (solid red circles) and embedded simulation (empty blue circles) from the north (left) and south (right) arms. These variables include DG0, DDG0, χ_{vtx}^2 , p_z , p_T and y	58
Figure 3.27 $A\epsilon$ for like-sign dimuons as a function of mass (left) and as a function of $\Delta\phi$ (right). The south arm is shown in solid red circles while the north arm is shown in empty blue circles.	58
Figure 3.28 The invariant mass spectra for like-sign pairs from the same event (solid black circles) and mixed-events (red band) for the north (left) and south (right) arms after applying the normalization factor to the mixed-events spectrum.	61
Figure 3.29 The invariant mass spectra for like-sign pairs from the same event (solid black circles) and mixed-events (red band), and the difference (empty blue sign) for the north (left) and south (right) arms after applying the normalization factor to the mixed-events spectrum. The figure also shows the $b\bar{b}$ spectrum (green points)	62

Figure 3.30 The mixed-events normalization factor, R , for the different iterations studied for the north (solid red squares) and south (empty blue squares) arms. The insert shows a zoom in on higher iterations.	63
Figure 3.31 The invariant mass spectra for like-sign pairs from the same event (solid black circles), mixed-events (red band), and the difference (empty blue sign) for the north (left) and south (right) arms after applying the normalization factor to the mixed-events spectrum. The figure also shows the $b\bar{b}$ spectrum (green points).	64
Figure 3.32 Left: Like-sign spectra after subtracting the mixed-events background for the north (solid red circles) and south (empty blue circles) arms. Right: The weighted average of the two arms.	64
Figure 3.33 Like-sign pairs from the same event (solid red circles) and mixed-events (empty blue circles) for the north (left) and south (right) arms after applying the normalization factor to the mixed-events spectrum.	65
Figure 3.34 Left: Like-sign spectra after subtracting the mixed-events background for the north (solid red circles) and south (empty blue circles) arms. Right: the weighted average of the two arms.	66
Figure 3.35 Generated single hadrons spectra (left) and reconstructed spectra (right) as a function of p_T for the north (red) and south (blue) arms.	67
Figure 3.36 Generated hadrons spectra (empty symbols) compared with UA1 data fits (solid lines). The open red circles are for pions while the open blue squares are for kaons.	68
Figure 3.37 Single hadron survival probability for the north arm as a function of p_T . The red line shows a third order polynomial fit while the error band represents a 95% confidence level of the fit. The green line shows the results of a similar fit to Run 9 data.	68
Figure 3.38 Single hadron survival probability for the south arm as a function of p_T . The red line shows a third order polynomial fit while the error band represents a 95% confidence level of the fit. The green line shows the results of a similar fit to Run 9 data.	69
Figure 3.39 Left: Dihadron mass spectra of the foreground pairs (left) and the normalized mixed-events pairs (blue). Right: correlated dihadron pairs. The top row is for the south arm while the bottom row is for the north arm.	70
Figure 3.40 Fitted hadronic background in the north arm (solid red line) and the south arm (dashed blue line) as a function of dihadron mass.	71

Figure 3.41 Left: Hadronic background is the north arm (empty blue circles), south arm (empty red squares) and their weighted average as a function of the dihadron mass. Right: the weighted average fitted with an exponential.	71
Figure 4.1 Data with both the trigger emulator and the dimuon live trigger applied.	74
Figure 4.2 Comparison of p_T dependent J/ψ $A\epsilon$ between PYTHIA simulation and dimuon generator output.	75
Figure 4.3 Comparison of single muon candidate tracks azimuthal distributions from J/ψ . The structure of the distributions are due to the eight octants of the MuTr detector.	76
Figure 4.4 Like-sign pairs spectra after mixed-events subtraction using different normalization windows (left) and their exponential fits (right).	78
Figure 4.5 BBC rate distribution of the runs used in the analysis. The dashed green line shows where the runs are divided into low and high rate.	79
Figure 4.6 Dimuon mass spectra for high (solid red circles) and low (empty blue circles) BBC rate for the north arm (left) and south arm (right).	80
Figure 4.7 The ratio of high to low BBC rate mass spectra in the north arm (left) and south arm (right) fitted by a zeroth order polynomial.	81
Figure 4.8 The ratio of high to low BBC rate mass spectra in the north arm (left) and south arm (right) fitted by a zeroth order polynomial.	82
Figure 4.9 Hadron survival probabilities. The points are the probability as determined using the GHEISHA package with a fit (red curve, with statistical error band). The remaining curves are determined with the combination of interaction package and fit function. The green curve is the survival probability as determined with the Run 9 simulation set up. On the left hand is the probability as determined for the south arm and the right is for the north arm.	83
Figure 4.10 Weighted dihadron pairs using the FLUKA hadronic interaction package and an exponential fit to the single hadron survival probability. The left is the foreground pairs in red and the mixed-event background pairs in blue. The right is the correlated pairs. The top is for the south and the bottom for the north arm.	83

Figure 4.11 Weighted dihadron pairs using the GHEISHA hadronic interaction package and an polynomial fit to the single hadron survival probability. The left is the foreground pairs in red and the mixed-event background pairs in blue. The right is the correlated pairs. The top is for the south and the bottom for the north arm.	84
Figure 4.12 Weighted dihadron pairs using the GHEISHA hadronic interaction package and an exponential fit to the single hadron survival probability. The left is the foreground pairs in red and the mixed-event background pairs in blue. The right is the correlated pairs. The top is for the south and the bottom for the north arm.	84
Figure 4.13 Left: Fits to different correlated dihadrons as determined through single particle survival using different hadronic interaction packages: FLUKA and GHEISHA. Right: The mass dependent systematic uncertainties associated with the cross section.	85
Figure 4.14 Different fits to the like-sign dimuons from open bottom decay.	86
Figure 4.15 β shown as a function of mass in the MC@NLO (left) and PYTHIA8 (right).	87
Figure 4.16 Distributions used to determine the scale factor.	89
Figure 5.1 Left: The dimuon mass dependent differential cross section before subtracting the hadronic background. Right: The dimuon mass dependent differential cross section after subtracting the hadronic background. The open blue circles are for the south arm and the closed red circles are for the north arm.	91
Figure 5.2 The weighted average of the differential cross section from the north and south arms as a function of dimuon mass.	92
Figure 5.3 Fraction of like-sign dimuons from B^0 meson oscillation ($\alpha(m)$) from MC@NLO (blue points), PYTHIA 6 (magenta points) and PYTHIA 8 (green points) within the PHENIX Muon Arms acceptance. Cyan data points are the RMS average of the three model calculations. The shaded boxes are the associated errors based on the three model calculations. The red curve is a second-order polynomial fit to the RMS data points.	94
Figure 5.4 The differential cross section multiplied by $\alpha(m)/\beta$ (open red diamonds) compared to the differential cross section before multiplying by $\alpha(m)/\beta$ (black diamonds).	95

Figure 5.5 The differential cross section multiplied by $\alpha(m)/\beta$ fitted by an exponential to extract the total cross section.	96
Figure 5.6 The differential cross section as a function of dimuon mass. The shaded boxes show the associated systematic uncertainties.	97
Figure 5.7 The differential cross section as a function of dimuon mass for the high (empty blue circles) and low (solid red circles) rates.	98
Figure 5.8 The difference between the differential cross sections of the high and low rate data sets.	99
Figure 5.9 Left: The dimuon $\Delta\phi$ dependent differential cross section before subtracting the hadronic background. Right: The dimuon $\Delta\phi$ dependent differential cross section before (solid red circles) and after (empty blue circles) subtracting the hadronic background.	99
Figure 5.10 Panel a shows world data of the total bottom cross section shown alongside pQCD calculation. Panel b shows the ratio of the measurements to the pQCD calculation [5, 10–17].	100
Figure A.1 Pseudorapidity, η . $\eta = 0$ is in the +y-axis direction at PHENIX and the beam pipe is along $\eta \rightarrow \infty$ [18].	104

LIST OF ABBREVIATIONS

QCD - Quantum ChromoDynamics

AGS - Alternating Gradient Synchrotron

BNL - Brookhaven National Lab

RHIC - Relativistic Heavy Ion Collider

QGP - Quark Gluon Plasma

PHENIX - Pioneering High Energy Nuclear Interaction eXperiment

QED - Quantum ElectroDynamics

pQCD - perturbative QCD

LHC - Large Hadron Collider

LO - Leading Order

NLO - Next to Leading Order

PC - Pair Creation

FE - Flavor Excitation

GS - Gluon Splitting

CKM Matrix - Cabibbo-Kobayashi-Maskawa Matrix

HNM - Hot Nuclear Matter

CNM - Cold Nuclear Matter

$p + p$ - proton-proton collision

MC - Monte Carlo

PDF - Parton Distribution Function

GEANT - GEometry ANd Tracking

PISA - PHENIX Integrated Simulation Application

STAR - Solenoid Tracker At RHIC

LINAC - LINear Accelerator Complex

EBIS - Electron Bean Ion Source

IR - Interaction Region

DOE - Department of Energy

CAD - Collider and Accelerator Deparment

BBC - Beam Beam Counter

MB - Minimum Bias

MuTr - Muon Tracker

MuID - Muon IDentifier

DAQ - Data Acquisition

PRDF - PHENIX Raw Data File

DST - Data Summary Tape

QA - Quality and Assurance

$A\epsilon$ - Acceptance \times Efficiency

1

INTRODUCTION

High energy nuclear physics is the study of nuclear matter at extreme energy (GeV), density (GeV/fm) and temperatures (MeV). This goal is currently accomplished by smashing nuclei together at speeds close to the speed of light (99.9995% c) and examining the fragments from the collision. In this process one can grasp an understanding of the nuclei before, during and after a collision has occurred. Comprehension of the interactions, through the strong force, is explained using quantum chromodynamic (QCD) theory. Experimentally performing this task is no easy feat requiring large complex systems and a huge amount of manpower.

The electronvolt (eV) is a unit of energy equal to the work done by moving an electron through a potential difference of one volt and the femtometer (fm), or a fermi, is a unit of distance with an order of magnitude of 10^{-15} . The size of the proton, in reference to a fm, is ≈ 1 fm in charge radius. The center of mass collision energies, \sqrt{s} , is the sum of the four momentums of the colliding nuclei.

One of the original particle accelerators is the Alternating Gradient Synchrotron (AGS) which is located at Brookhaven National Lab (BNL) on Long Island, New York. It was at this accelerator complex that Nobel Prize winning work was done. The J/ψ meson particle, the ν_μ neutrino particle and “ CP violation”, and the idea that the universe is not symmetrical, were all discovered using the AGS. The complex was further built up to include the Relativistic Heavy Ion Collider (RHIC) to study particle properties and the state of matter known as the Quark Gluon Plasma (QGP). This substance is created when nuclei

collide and break down into a deconfined state of fundamental particles made up of quarks and gluons. There are many observables of this state of matter that can give insight into how the QGP interacts with itself. One experiment studying the QGP is the Pioneering High Energy Nuclear Interaction eXperiment (PHENIX) at BNL.

The outline of this thesis is as follows: The remainder of this chapter outlines the physics contained within the remainder of the document. Chapter 2 will discuss the RHIC complex, the PHENIX experiment and the detector subsystems used to make the measurement. Chapter 3 will explain the methods used to extract the measurement. Chapter 4 documents the systematic uncertainties within the procedure and Chapter 5 presents the final results. Finally, Chapter 6 will conclude this thesis with a brief discussion.

1.1 The Standard Model

Our fundamental understanding of the world around us is almost fully contained within the Standard Model. A theory that was pieced together in the 1970s, it incorporates three of the four fundamental forces, their force carrying particles and the elementary building blocks of the known universe. The Standard Model systematically organizes all the known particles. They are separated into sub categories including the fermions (which includes quarks and leptons) and the bosons, as shown in Figure 1.1. It is currently the most robust model we have to explain the physical world.

For the fermions, there are six quarks (or “flavors”), each with a corresponding anti-particle (carrying the opposite electric charge). The quarks carry fractional charge and are

spin half particles with varying masses. The leptons include the electron, the muon and the tau particle as well as their corresponding neutrinos. These have integer charge and are also spin half particles with varying masses. Another categorization of the model is the three generations. Each generation contains two quarks and two leptons where one quark has an electric charge of $2/3$ and the other has $-1/3$. The leptons have electric charge -1 and the other is neutral charge (the neutrino). The first generation is what makes up ordinary everyday matter such as protons and neutrons in combination with electrons.

Standard Model of Elementary Particles

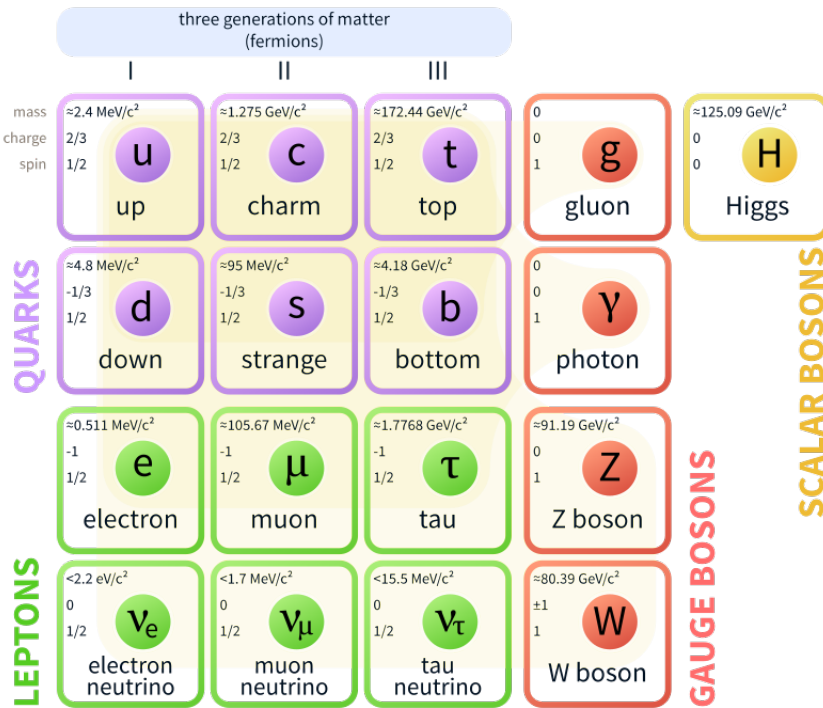


Figure 1.1: The elementary particles as described by the Standard Model [1].

Bosons are the force carrying particles and their defining quality is that they have integer spin. The photon has zero mass and charge and is the field particle that carries the electro-

magnetic force described by quantum electrodynamics (QED). The weak force is carried by the W and Z bosons and is responsible for flavor changing quark decays. The electromagnetic and weak forces can be combined into a unified theory known as the electroweak theory. The gluon is the field particle carrying the strong force and has no charge and is massless. Quarks and gluons also have an additional feature known as “color” charge to help settle any issues arising from the Pauli Exclusion Principle [19]. The recently discovered Higgs Boson is a scalar boson with a large mass but no electric charge and is spin zero. It is credited with giving particles mass through the Higgs Mechanism [20]. Gravity is the missing force from the Standard Model but is described by the General Theory of Relativity [21].

QCD is the theory used to describe the interactions between quarks and gluons. These particles interact via the strong force which is carried by the gluons. Unlike in QED, the force carrying gauge boson in QCD can interact with itself. Defining features of the strong force are the properties of asymptotic freedom and confinement. Asymptotic freedom is the idea that as quarks move closer to one another and as the energy scale increases the force between them decreases. Confinement is the idea that all quarks are found in composite particles, known as hadrons, such as mesons (quark anti-quark pairs), baryons (three quarks) and other exotic multi-quark particles that are colorless. Hadrons are colorless such that in baryons each quark carries one of the three color charges (red, green and blue OR anti-red, anti-green and anti-blue)¹. In mesons, one quark carries the color charge and the other anti-color charge (of the other), again making a color neutral composite particle.

The Standard Model continues to be compared to results from current experiments and

¹Color charge names are only convention

is thriving as a theory to explain the universe on the microscopic level. There are many ways to test the Model. One such way is with heavy flavor physics.

1.2 Heavy Flavor Physics

Heavy flavor physics is the study of quarks that have a mass greater than one GeV/c^2 (greater than the mass of the proton, $0.938 \text{ GeV}/c^2$). This includes the charm ($1.29 \text{ GeV}/c^2$), bottom ($4.18 \text{ GeV}/c^2$) and top ($173.3 \text{ GeV}/c^2$) quarks. The charm and bottom quarks are classic probes for studying the hot and dense medium because they are produced early in the collision process and can transverse the full time evolution of the QGP system. The top quark is too massive making it extremely unstable and unable to form bound states. It is therefore not a functional tool to study the QGP. It is also not produced at RHIC energies. Heavy flavor can be studied with “open heavy flavor,” mesons made up of one charm (D mesons) or bottom (B mesons) quark or with quarkonia, a meson pair made up of one quark and its anti-quark. To use heavy flavor quarks as probes of the medium their production and fragmentation must be understood.

1.2.1 Heavy Flavor Production

The production of heavy flavor pairs is not well understood but not due to a lack of trying. Perturbative QCD (pQCD) is used to describe and model production because heavy flavor masses are larger than the QCD scale, $m_{c,b} \gg \Lambda_{QCD} \approx 200 \text{ MeV}$ but comes up short when compared to data. pQCD allows for calculations of production cross sections which wouldn’t otherwise be possible with low mass quarks. Often, at lower energies, theory underestimates

the heavy flavor production cross sections but not so much at higher energies like those found at the Large Hadron Collider (LHC) which are on the TeV scale [17, 22, 23].

Production predominantly occurs at Leading Order (LO) and Next to Leading Order (NLO) within the perturbative framework. The LO processes are known as Pair Creation (PC) and are thought to dominate production at RHIC energies [24]. LO production are $2 \rightarrow 2$ processes where both heavy quarks participate in the hard scattering and includes gluon-gluon fusion and quark anti-quark annihilation. The production diagrams for LO can be seen in Figure 1.2.

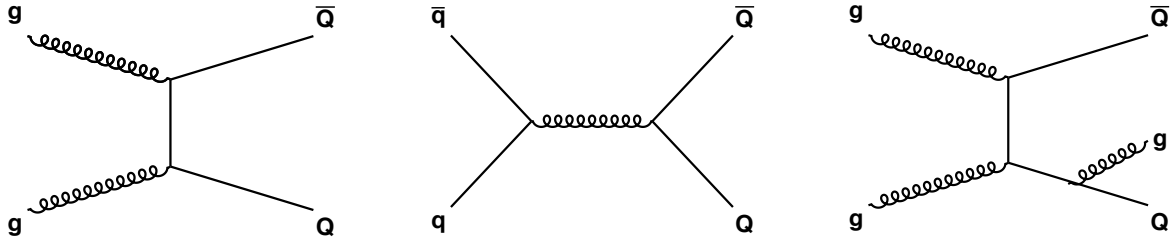


Figure 1.2: Leading Order processes diagrams, collectively known as Pair Creation. From left to right is gluon fusion, quark fusion and gluon fusion with gluon emission.

NLO order processes include Flavor Excitation (FE) and Gluon Splitting (GS). In FE process, only one quark participates in the hard scattering process and in GS neither quark is involved in the scattering process. NLO production mechanisms have $2 \rightarrow 3$ topologies. At RHIC energies ($\sqrt{s} = 200$ GeV), FE is found to be a larger contribution than GS in the overall production of heavy flavor quark pairs [24]. NLO order production diagrams are

shown in Figure 1.3.

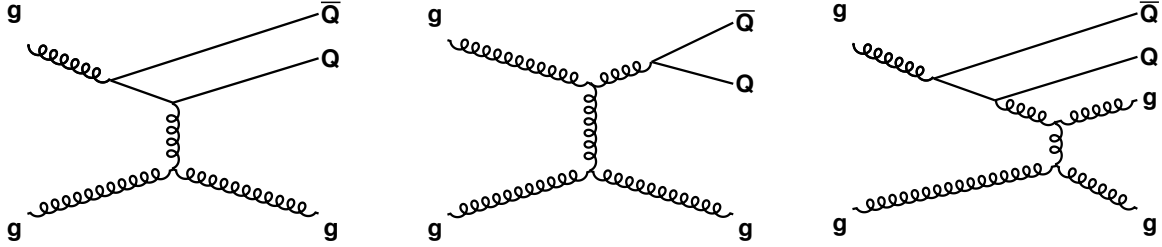


Figure 1.3: Next to Leading Order processes diagrams. From left to right is flavor excitation, gluon splitting and flavor excitation with the emission of a gluon.

1.2.2 Heavy Flavor Fragmentation

Heavy flavor particles are not stable and therefore must decay. Once created the heavy flavor quarks will hadronize and then decay into a smaller mass quarks, via the weak force, following the probabilities laid out in the Cabibbo-Kobayashi-Maskawa Matrix (CKM). The CKM matrix is [25]:

$$\begin{bmatrix} V_{ud} & V_{us} & V_{ub} \\ V_{cd} & V_{cs} & V_{cb} \\ V_{td} & V_{ts} & V_{tb} \end{bmatrix} = \begin{bmatrix} 0.974 & 0.225 & 4.09 \times 10^{-3} \\ 0.220 & 0.995 & 40.5 \times 10^{-3} \\ 8.2 \times 10^{-3} & 40.0 \times 10^{-3} & 1.01 \end{bmatrix}$$

The CKM Matrix magnitudes, V_{ij} , are related to the quarks decay probability from $q_i \rightarrow q_i'$. We can see that along the diagonal these are the more likely decay processes, specifically $d \rightarrow u$, $c \rightarrow s$ and $t \rightarrow b$. A visual representation of the probabilities of decay and exchange of the W boson is shown in Figure 1.4.

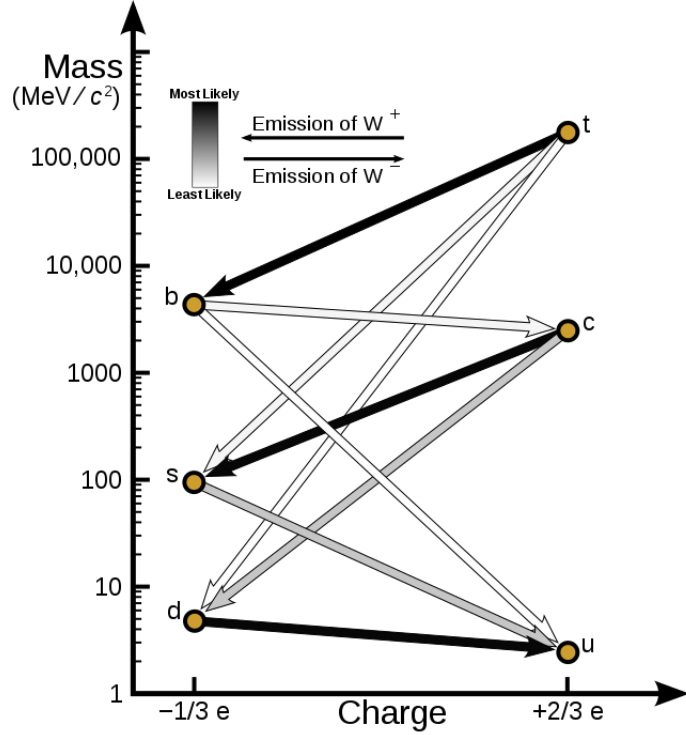


Figure 1.4: The flavor changing weak decay processes and their relative decay modes [2].

1.2.3 Bottom Physics

The bottom quark (or “beauty”) was theorized in 1973 by Toshihide Maskawa and Makoto Kobayashi to explain CP violation in relation to the CKM Matrix and experimentally confirmed at Fermi Lab in the USA in 1977 by the E288 experiment [26, 27]. It is the second largest of the quarks at $4.18 \text{ GeV}/c^2$ and the largest “down-like” quark (third generation). It is a background in the study of the top quarks as well as the top quarks primary decay product. When it decays it must do so to another generation of quarks since it is the smaller of the two within its own generation. Commonly, this decay is $b \rightarrow c$ [28].

Neutral charge B mesons, B^0 , ($B_d^0 \bar{B}_d^0$ and $B_s^0 \bar{B}_s^0$) have an added property of being able to oscillate between their particle and anti-particle state similar to K^0 oscillations [29]. This

flavor changing process occurs through the exchange of a W boson and an “up-like” quark. The diagram describing this exchange is shown in Figure 1.5. The time-integrated probability that a B^0 meson will oscillate to a \bar{B}^0 meson before decay (and vice versa) is described by the mixing parameter

$$\chi = \frac{Prob(B^0 \rightarrow \bar{B}^0 \rightarrow l)}{Prob(B^0 \rightarrow B^0 \rightarrow l)} = \frac{(\Delta m/\Gamma)^2}{[2 + (\Delta m/\Gamma)^2]} \quad (1.1)$$

where Δm is the mass difference between the light and heavy mass eigenstates and Γ is the decay width. For the B_d^0 system $\chi_d \sim 0.17$ and for the B_s^0 system $\chi_s \sim 0.49$ [29].

In many experiments, the two B^0 meson states can not be separated. The mixing parameter ($\bar{\chi}$) can be calculated as the weighted average of the two B^0 meson mixing parameters χ_d and χ_s .

$$\bar{\chi} = f_d \chi_d + f_s \chi_s = 0.12, \quad (1.2)$$

where $f_d = 0.401$ and $f_s = 0.113$ are the branching fractions of the $b \rightarrow B_d^0$ and $b \rightarrow B_s^0$ mesons, respectively.

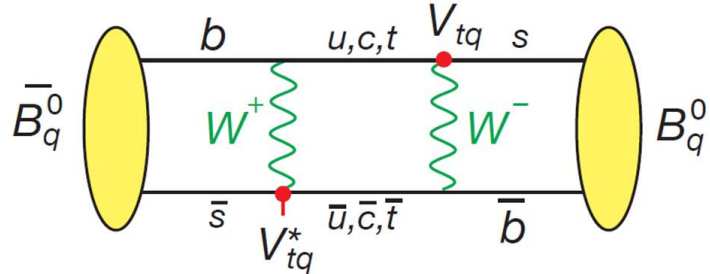


Figure 1.5: B^0 oscillation as understood in the Standard Model framework.

1.3 Quark Gluon Plasma

The state of matter thought to have existed in the first microseconds after the Big Bang is the QGP. It is a hot and dense state of matter in which quarks and gluons are in a deconfined state and act like a near perfect fluid. The particles have energies on the order of $170 \text{ MeV}/c^2$ each with the medium having a temperature on the order of 10^{12} Kelvin and an energy density, $\varepsilon \approx 1 \text{ GeV}/fm^3$ [30]. Its lifetime (in the laboratory setting) is $\approx 7 \text{ fm}/c$. In the diagram showing the History of the Universe (Figure 1.6) the QGP can be seen after inflation occurs. The axis is both time and temperature of the universe. At the top of the diagram are marked the regions that we believed that we can probe with modern day experiments.

The QGP is also shown on the QCD phase diagram seen in Figure 1.7. This phase diagram, much like the one of water, shows nuclear matter in different conditions. The specific states are found at different temperatures and baryonic potentials. At low temperatures and baryonic potentials exists everyday matter (protons, neutrons) comprising confined quarks and gluons in composite particles described as hadron gas. There is then a first order phase transition as with increasing temperature or baryon chemical potential, or both. The color superconductor phase is analogous to superconducting metal but isn't of importance here and therefore not discussed in this thesis. More importantly at high temperatures the QGP occurs. The highlighted regions can access this state of matter at RHIC and LHC energies. There is an ongoing hunt for the critical point at which the first order phase transition occurs by tweaking the initial conditions of the collisions and scanning at many center of mass

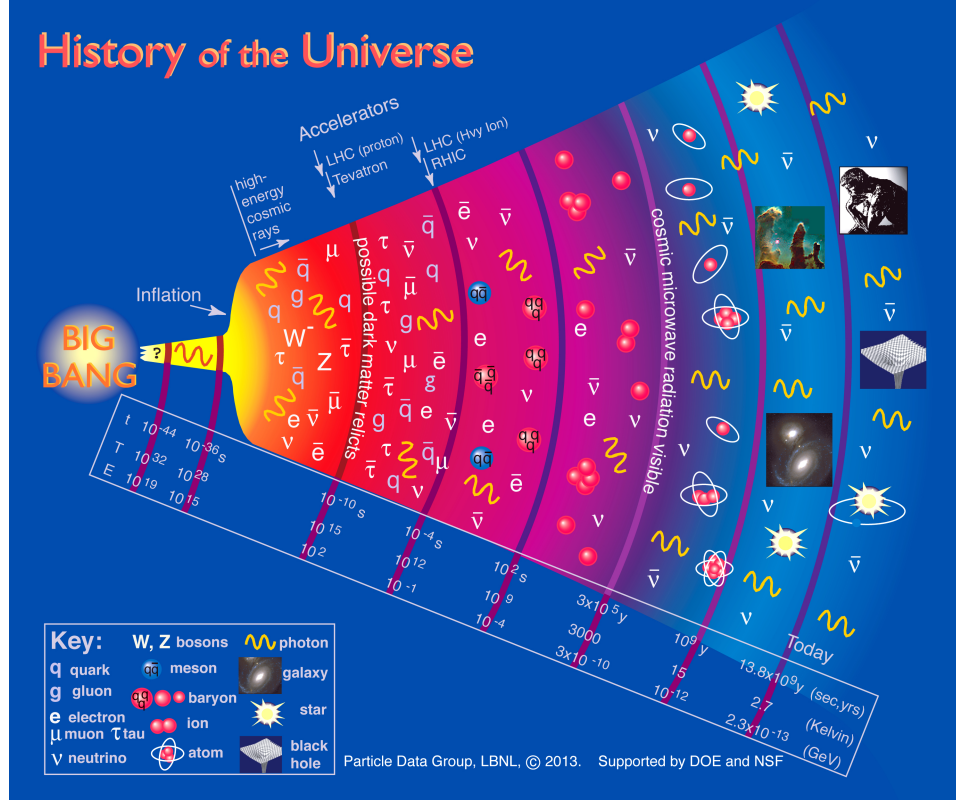


Figure 1.6: The history of the universe starting with the Big Bang on the left and the modern era on the right. The scale along the diagonal axis includes time, temperature and energy [3].

energies.

We study the QGP in the laboratory by creating what we call “little bangs”. These are performed by smashing together heavy ions at $99.9995\%c$ and recreating this medium from the early universe, 13.8 Billion years ago. The process is complicated and requires a full understanding of the evolution of the system from pre-collision beam conditions all the way until chemical freeze out at which point particles can be measured.

A schematic of the collision process can be seen in Figure 1.8. The diagram shows the full time evolution of the system from incoming beams, pre-equilibrium, QGP, hydrodynamic

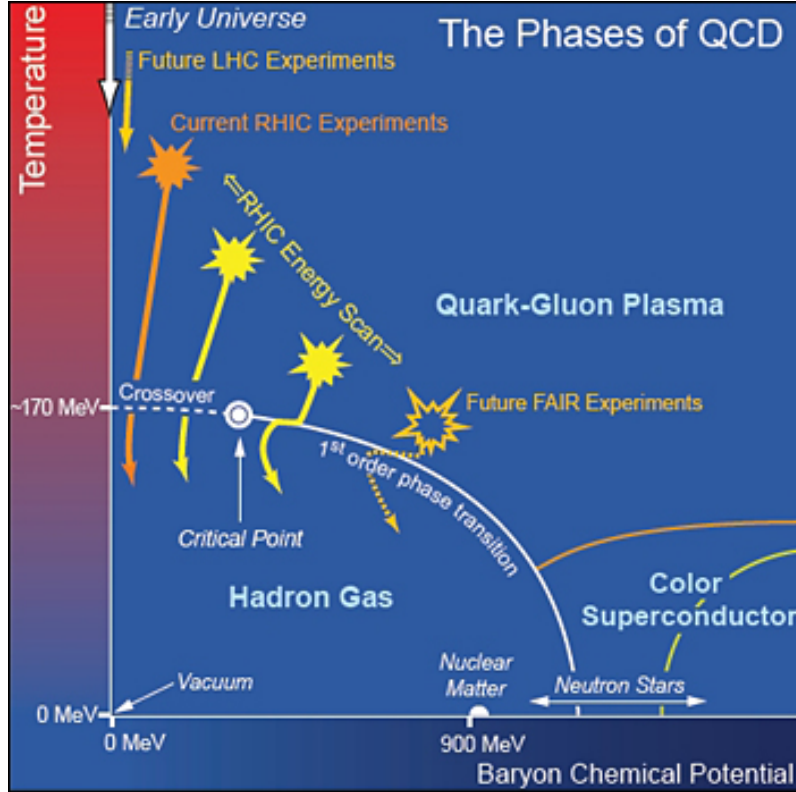


Figure 1.7: The QCD phase diagram. Baryon chemical potential versus temperature [4].

evolution to the hadron gas and eventually chemical freeze out where stable particles emerge.

There are several ways to quantify and study QGP based on its many signatures. The major ones are:

- **Flow** which studies the collective medium and how it evolves over time. It gives a big picture of the bulk properties.
- **Jets** which are collimated beams of high momentum particles that occur due to partonic fragmentation. It is thought that in the QGP jets are “quenched” and insights into energy loss of the system can be studied.

Relativistic Heavy Ion Collisions: little bang

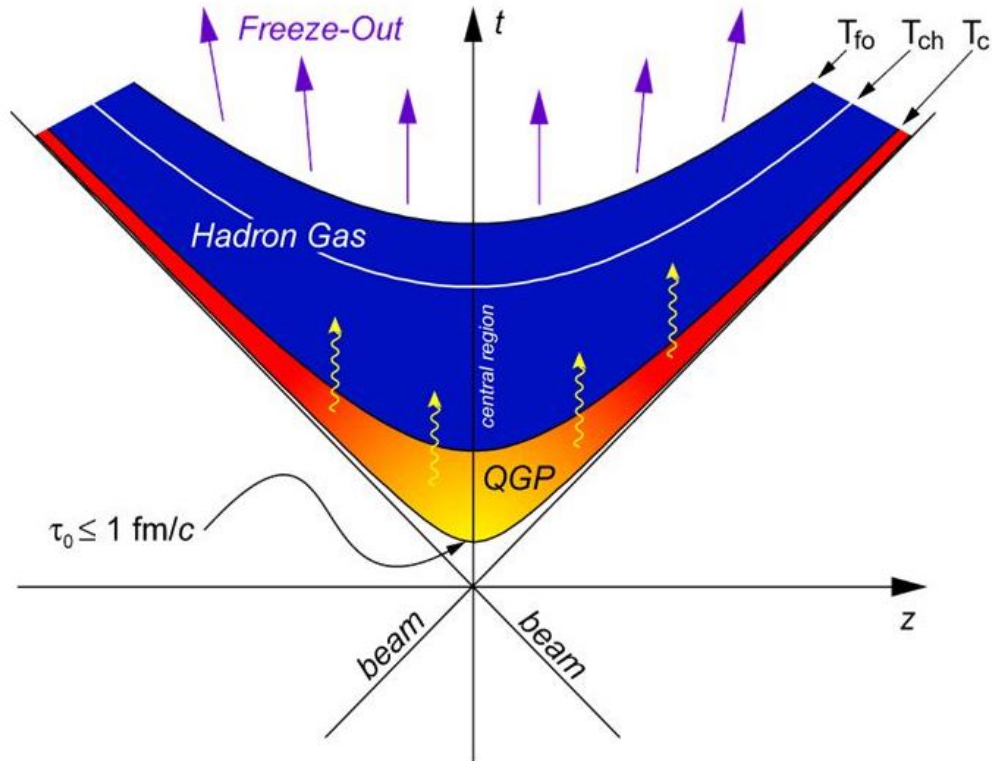


Figure 1.8: The heavy ion collision evolution from colliding species up to chemical freeze out.

- **Quarkonia** measurements are useful in determining the temperature of the system. Knowing the binding energy of the mesons and at which energy they disassociate can prove useful.
- **Low mass vector mesons** are important in understanding the initial state of the system, soft processes and provide further insights into strangeness enhancement.
- **Open heavy flavor** which is the study of mesons with constituents containing either

a bottom or a charm quark. These are good probes of the QGP because they are produced early in the collision system, can transverse the medium but interact via scattering, providing information on the density of the system.

Of course it's not that easy; there are both Hot Nuclear Matter (HNM) effects and Cold Nuclear Matter (CNM) effects that need to be disentangled. HNM effects are those that exist due to the presence of the QGP medium, while CNM effects are those due to the presence of normal nuclear matter in a collision process. CNM effects are determined in smaller and typically asymmetric collisions systems. These need to be taken into consideration when studying the QGP to isolate the contributions of the HNM. Another consideration is what happens in the simplest processes: collision between two protons, which provides a baseline for both CNM and HNM effects. An understanding of open bottom production in $p + p$ collisions is the objective of this work.

1.4 $b\bar{b}$ Measurement

In this thesis, the $\sigma_{b\bar{b}}$ is measured in $p + p$ collisions. $\sigma_{b\bar{b}}$ is the production cross section of the $b\bar{b}$ reaction. It is a measure of the relative yield of bottom quark, anti-quark pairs in relation to the $p + p$ collision process. It is center of mass collision energy (\sqrt{s}) dependent quantity and pQCD theory calculations of $\sigma_{b\bar{b}}$ can be seen in Figure 1.9. The calculation is dependent upon the assumed mass of the b -quark [5]. There have been many measurements over the years in the range of fixed target experiments up to current LHC energies with varying measurement methods and levels of success in comparison to the pQCD calculation.

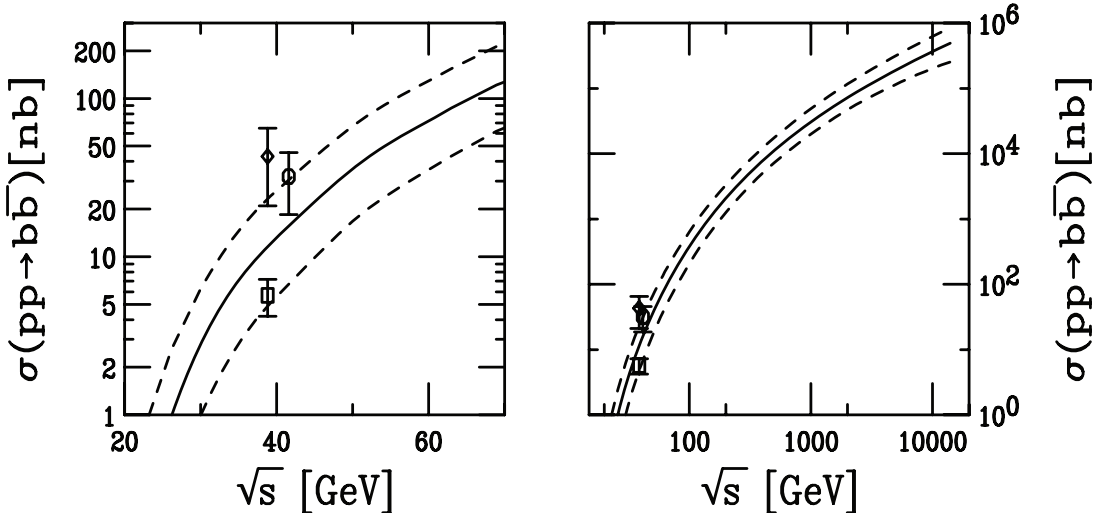


Figure 1.9: pQCD calculations of $\sigma_{b\bar{b}}$ as a function of \sqrt{s} . The left side is 20-70 GeV and the right side is 20-14,000 GeV. The calculation has a central value and an associated error band based on calculation inputs [5].

The measurement in this thesis is accomplished by separating out the signal from semi-leptonic decays of B mesons into like-sign dimuon pairs. B mesons decay semi-leptonically $\approx 10\%$ of the time [31]. Typically, with quark anti-quark pairs, a pair of unlike-sign pair leptons would emerge, l^+l^- , but due to the $B^0\bar{B}^0$ oscillation like-sign pairs $l^\pm l^\pm$ are possible as well. Table 1.1 shows the total contributions to the di-lepton spectrums. The columns are for unlike-sign and like-sign pairs while the rows separate the contributions into mass regions. The mass region separates out the different quarkonia states as well as some differences in the decay kinematics of the b -quarks. In the like-sign lepton contributions are pairs coming from either the feed down process of $b \rightarrow c$ or from $B^0\bar{B}^0$ oscillation. These dominate in the higher mass region. Of course there are light hadronic contributions in all cases. The

source of like-sign dimuon pairs from open bottom contributions, in the high mass region, are shown in Figures 1.10 and 1.11.

Table 1.1: Dominant physics processes that can contribute to dimuon signal in specified mass range and charge correlation.

	N^{+-}	$N^{\pm\pm}$
$m_{\mu\mu} < 4 \text{ GeV}$	Quarkonia ($J/\psi, \psi'$) b -decay chain (same b) $b\bar{b} \rightarrow \mu\mu$ $c\bar{c} \rightarrow \mu\mu$ Drell-Yan	c -decay chain b -decay chain (diff b)
$m_{\mu\mu} > 4 \text{ GeV}$	Quarkonia (Υ family) b -decay chain (diff b) $b\bar{b} \rightarrow \mu\mu$ $c\bar{c} \rightarrow \mu\mu$ Drell-Yan	$b\bar{b} \rightarrow \mu\mu$ (prompt with osc) b -decay chain (diff b)

The measurements discussed in this thesis take advantage of the $B^0\bar{B}^0$ oscillation properties in the high mass dimuon region ($> 4 \text{ GeV}/c^2$). This is a solid approach at separating charm and bottom contributions in the di-lepton spectra from one another which can otherwise be problematic. We measure like-sign dimuons within the PHENIX muon arm detector acceptance which are used to get a total $B^0\bar{B}^0$ yield. Combinatorial background is estimated using mixed-event dimuons with an iterative normalization technique. Hadronic background sources are approximated from the dimuon spectra and removed. The “yields”, or differential yields, are the yields within a give kinematic window as measured with PHENIX.

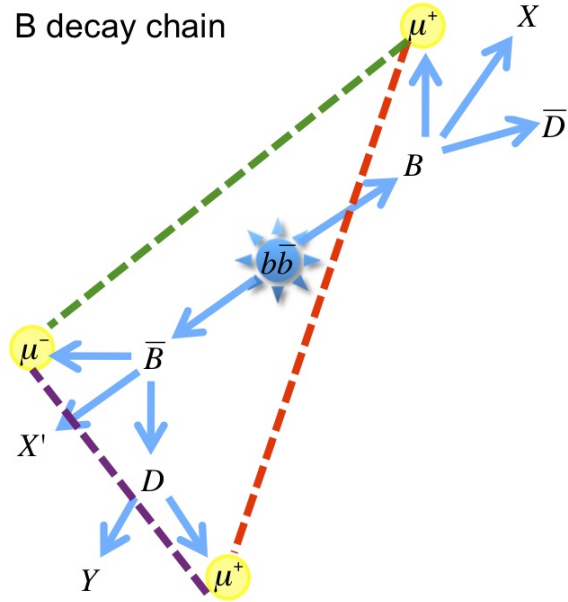


Figure 1.10: Correlated muon pairs from the primary/secondary B decays. Here, B and \bar{B} are generic open bottom hadrons; X , Y , and X' are arbitrary decay products [6].

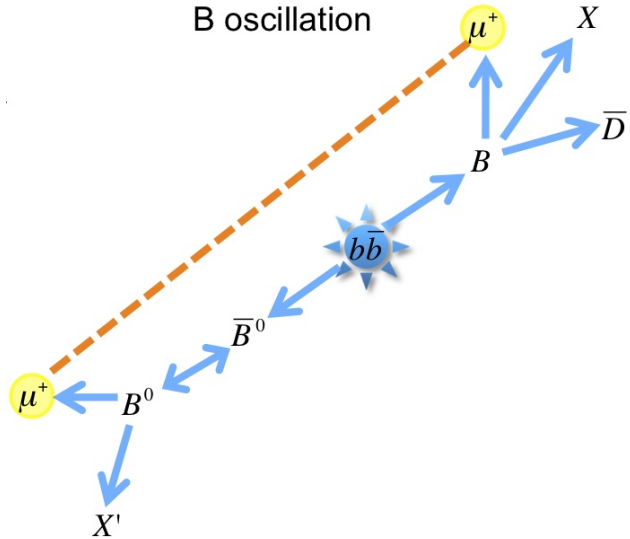


Figure 1.11: Correlated primary muon pairs from B^0 decays due to oscillations. Here, B is a generic open bottom hadron and B^0 can be either B_d^0 or B_s^0 ; X and X' are arbitrary decay products [6].

They are converted into differential cross sections, again, the cross section in reference to given kinematic windows. Then, using Monte Carlo (MC) based event generators (such as PYTHIA and MC@NLO [32–34]), we can separate out the contribution strictly from B^0 meson oscillations. We further extrapolate to the full dimuon signal, regardless of pair charge, and finally extrapolate to full phase space.

We use MC simulation to model collisions of $p + p$ at $\sqrt{s} = 510$ GeV center of mass energies. The model samples known parton distribution functions (PDF) and uses known cross sections from data to reproduce the whole collision processes. PDFs are probability distribution functions of quarks and gluons within hadrons and are fractional momentum (of quark or gluon in the hadron) and energy transfer dependent. MC simulation is used throughout the analysis with both pure simulation as well as simulation with sampled event vertices from real data, run through the PHENIX GEometry ANd Tracking (GEANT 4) simulation, known as PHENIX Integrated Simulation Application (PISA), and then matched with corresponding detector backgrounds (again from data). This procedure is known as embedding simulation.

2**EXPERIMENT**

This chapter will outline the experimental setup used to make the measurements presented in this dissertation. The first section explains the RHIC accelerator complex. The second outlines the PHENIX experiment and detector subsystems as well as the process of collecting data up to the point at which an data analysis can begin.

2.1 RHIC

The RHIC is located at BNL in Upton NY, USA. An aerial view of the complex (at BNL) is shown in Figure 2.1. It was designed to study the QGP and the spin of the proton in $p + p$ collisions. It is the world's first polarized $p + p$ collider. It is an extremely versatile machine that is capable of colliding a variety of collision species in a range of 8 – 510 GeV center of mass energies. All the possible collision runs since the beginning of the RHIC are shown in Figure 2.2. The ability to control the system size at varying energies will help determine the critical point at which the QGP is formed.

There were originally four experiments located on the RHIC ring: PHENIX, STAR, PHOBOS and BRAHMS, each having its own physics motivations (goals). At the time of this writing, only STAR was running. The PHOBOS experiment was designed to study rare processes through the use of silicon vertex detectors for precision particle tracking and subsequent measurement of correlated angular distributions of particles to help determine those processes. BRAHMS was built with the intention of exploring hadronic production within the collision and the QGP medium. Both of these smaller experiments ran from 2000,

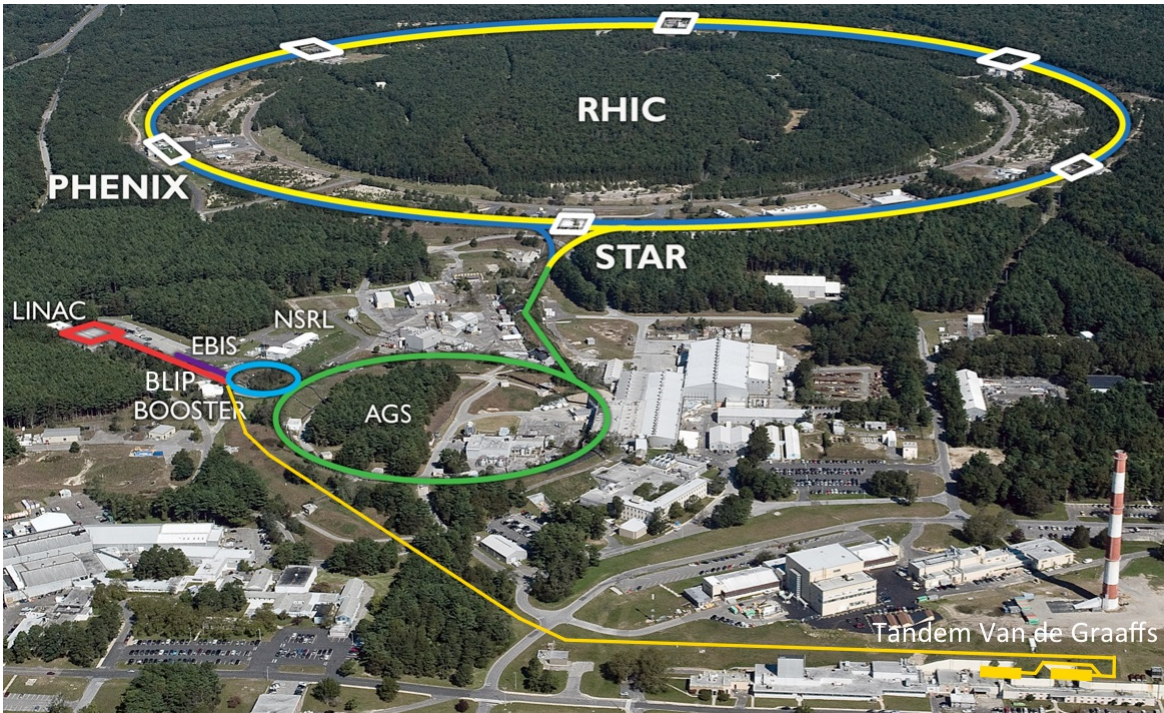


Figure 2.1: An aerial view of the RHIC complex at BNL. Overlaid on the picture are lines which the particles travel as they are produced and fed into the RHIC ring [7].

the start of RHIC, to 2006 when they were both decommissioned. STAR is one of the two larger experiments on the RHIC ring and stands for Solenoid Tracker At RHIC. Much like PHENIX, STAR is a multi purpose experiment to study nuclear structure, QGP, and to unwrap the proton spin puzzle. STAR measurements are complimentary to the PHENIX measurements and vice-versa.

The RHIC complex consists of many components in order to get collision species from source to collision point. They are listed here in order of beam progression. The Linear Accelerator Complex (LINAC, proton source) gets polarized hydrogen ions up to 200 MeV energies. The tandem Van de Graaf accelerators (for heavy ion sources) were replaced in 2012 with the Electron Beam Ion Source (EBIS) which gets ions up to 2 MeV/amu energies [35].

RHIC energies, species combinations and luminosities (Run-1 to 17)

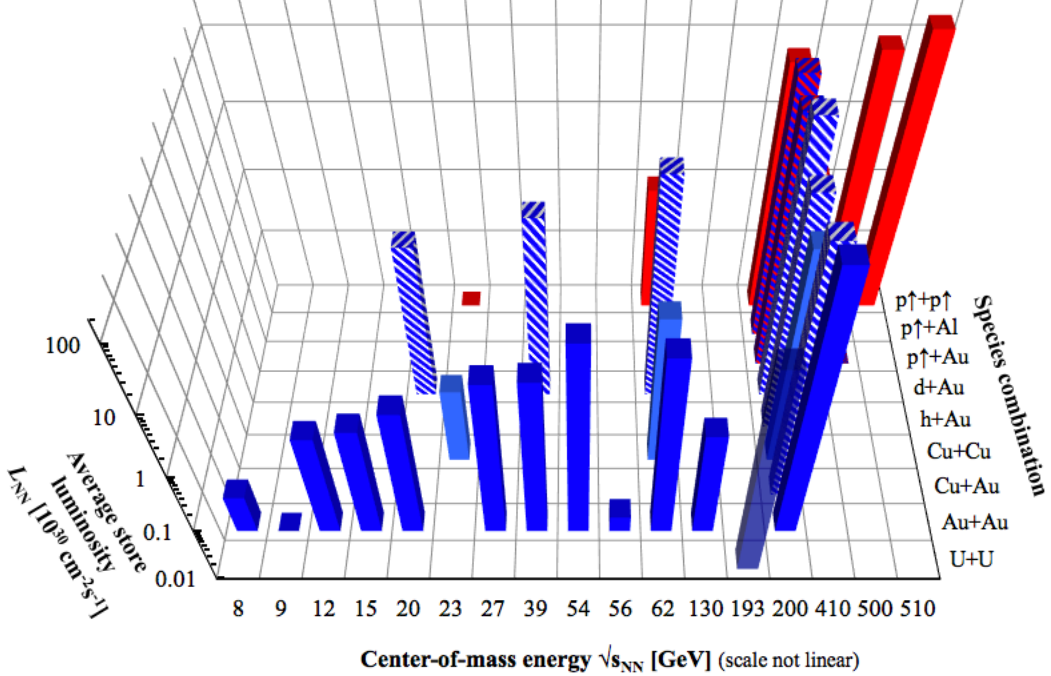


Figure 2.2: RHIC collision summary of all collision energies, species and their average store luminosity. The vast array of collision energies and species is unique to RHIC [8].

These are then injected into the booster ring which gets the beam energies up to 1500 MeV. The booster ring is responsible for the AGS being able to accelerate ions larger than silicon (atomic mass 28) which was its previous limitation [36]. Beams are then injected into the AGS, after the booster, which supplies the RHIC ring with a 2.4 mile circumference. Once a heavy ion beam is brought up to full speed in the RHIC ring, the ions are fully stripped of their electrons. See Figure 2.1 to follow this progression.

RHIC consists of two rings in which 111 bunches of particles (the beam) are stored for hours at a time. They are called the “yellow” and “blue” rings and they intersect at six interaction points. A collision occurs at these interaction points every 109 nanoseconds.

The bunches consist of 185×10^9 protons each (Run 13) [37]. These interaction regions (IR), where collisions occur, are where the experiment’s detectors are located. The white boxes in Figure 2.1 highlight these interaction points. The RHIC control room provides a global clock to the experiments to be used for event timing information. In order to ramp the beam up to their peak energies and to keep the particles inside the rings, a collection of superconducting magnets is used. There are 1740 magnets in total each of which requires cryogenic helium to be kept at 4.5 K.

Ultimately, RHIC can collide heavy ions at center of mass energies up to 100 GeV per ion and protons up to 255 GeV per proton. A summary of the all the $p + p$ Runs provided by RHIC over the years is shown in Figure 2.3. A “Run” is defined as the data collection period, numbered progressively, which happens to be the calendar year the data collection occurred. The summary shows the energies of the collisions as well as the percentage of polarization of the beams. Visible is the dominance of the Run 13 data set, with the Integrated Polarized Proton Luminosity more than double all the previous years’ $p + p$ Runs due to upgrades of the RHIC complex. This is the data set analyzed in this thesis.

Data collection requires more than just flipping an “on” switch! Large amounts of funding (from the U.S. Department of Energy (DOE)), planning and organization are required to run RHIC and the experiments. The Collider and Accelerator Department (CAD) is responsible for providing the beam to each of the experiments, while the experiments each have their own organizational structure in order to collect data. The schedule of such events is shown in Figure 2.4. It can be seen that it takes several weeks to cool down the RHIC ring from

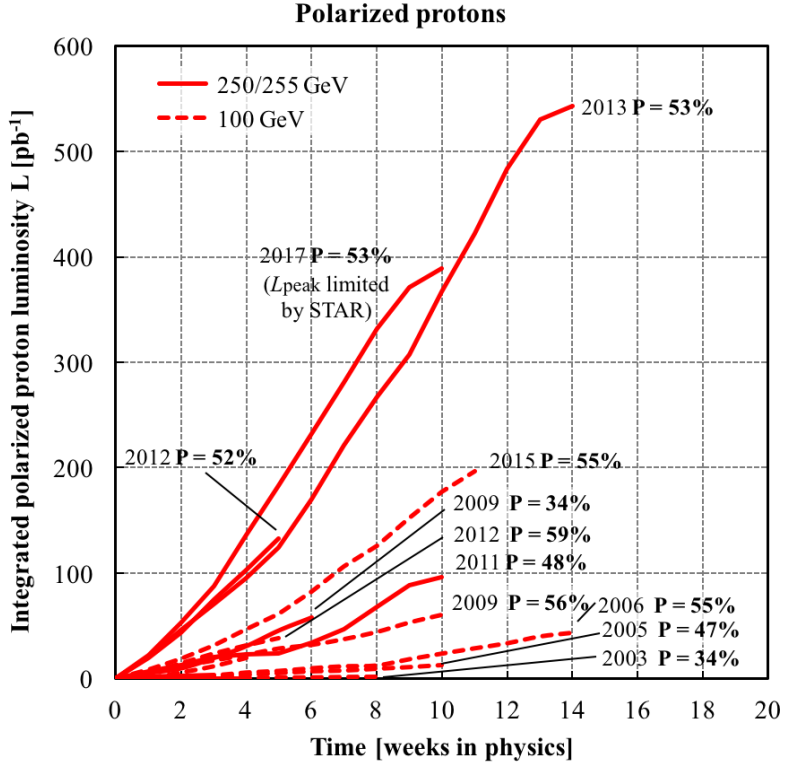


Figure 2.3: RHIC delivered luminosity of all polarized $p + p$ Runs [8].

its stand-by state as well as get to the remaining subsystems up and running.

2.2 PHENIX

PHENIX was located at the eight o'clock interaction position on the RHIC ring. It was run from 2000-2016 and was designed to study the QGP medium. It had four “arms” in which it would detect an assortment of particles including muons, electrons, hadrons and photons. The two central arms cover the rapidity, $|y| < 0.35$ with a total π azimuth (See Appendix A for an explanation of the kinematics used through out this thesis). The focus of this dissertation is a measurement made with the two muon arms which cover a rapidity

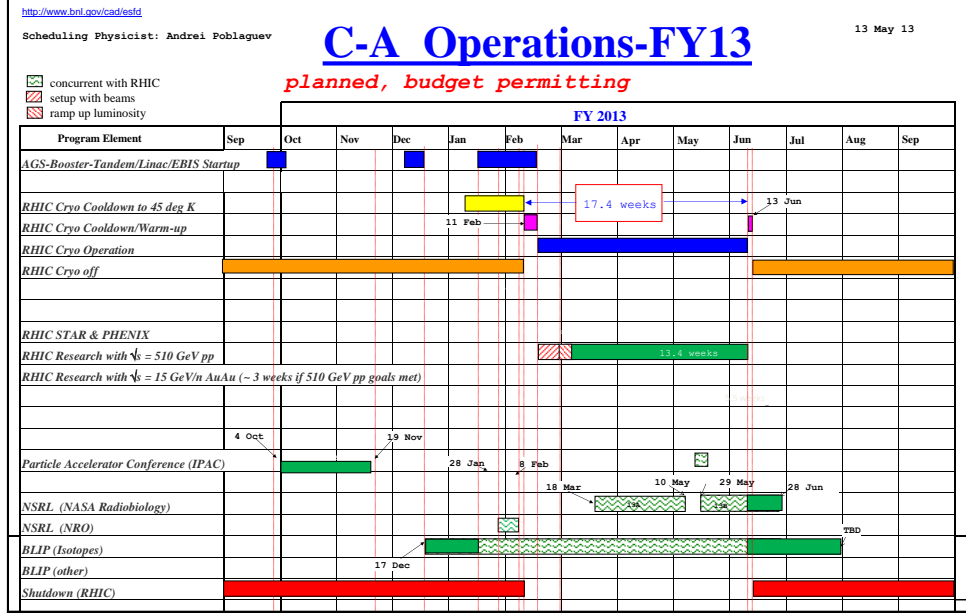


Figure 2.4: The planned CAD Run 13 schedule as of May 3, 2013.

region of $1.2 < y < 2.4$ in the north arm and $-2.2 < y < -1.2$ in the south arm covering a full 2π azimuth. A schematic of the four main arms can be seen in Figure 2.5 which shows the detector configurations as they were used in the Run 12 (2012) and Run 13 (2013) data taking periods. During the 2012 run there was beam spray which damaged, beyond use, the east VTX detector, a silicon vertex detector used to make precision tracking measurements. The damage was such that it prevented secondary vertex measurements with the 2013 data. The cartesian coordinate system of the detectors are defined as the $+z$ -axis being along the beam pipe towards the north arm, the $+x$ -axis is in the direction of the east arm, making the $+y$ -axis in the vertical direction. Nominally the Interaction Region (IR), where the collisions

occur, is at (0,0,0) but varies due to beam parameters. The beam pipe runs through the center of the detector system along the z-axis and is made of Beryllium pipe of radius 75 mm and 1.0 mm thick.

2.2.1 Beam Beam Counter

The Beam Beam Counter (BBC) detectors are global detectors used as the Minimum Bias (MB) event trigger detector. They consist of an assemblage of 64 quartz Cherenkov counters that surround the beam pipe and are located 144 cm from the nominal interaction point. See Figure 2.6. They cover a rapidity of $3.1 < |y| < 3.9$ with full 2π coverage and are used to determine the event vertex, event time and event centrality in heavy ion collisions. The event vertex is determined by calculating the timing differences between the two particles firing in the two detectors in each arm. The BBC detector has a resolution of 2 cm across the central 60 cm event vertex region along the z-axis. It can not determine the event vertex in the x,y plane.

A MB event occurs when one particle fires at least one Cherenkov detector in each arm. It provides three triggers based on the event vertex position, no vertex (record all events), $|\text{vertex}| < 30$ cm and $|\text{vertex}| < 15$ cm. Generally there is only one collision per event but it is known that multiple collisions can occur in a triggered event. With increased luminosity in the RHIC, there is increased likelihood of a second collision in an event. The possibility of a second collision must be considered during an analysis.

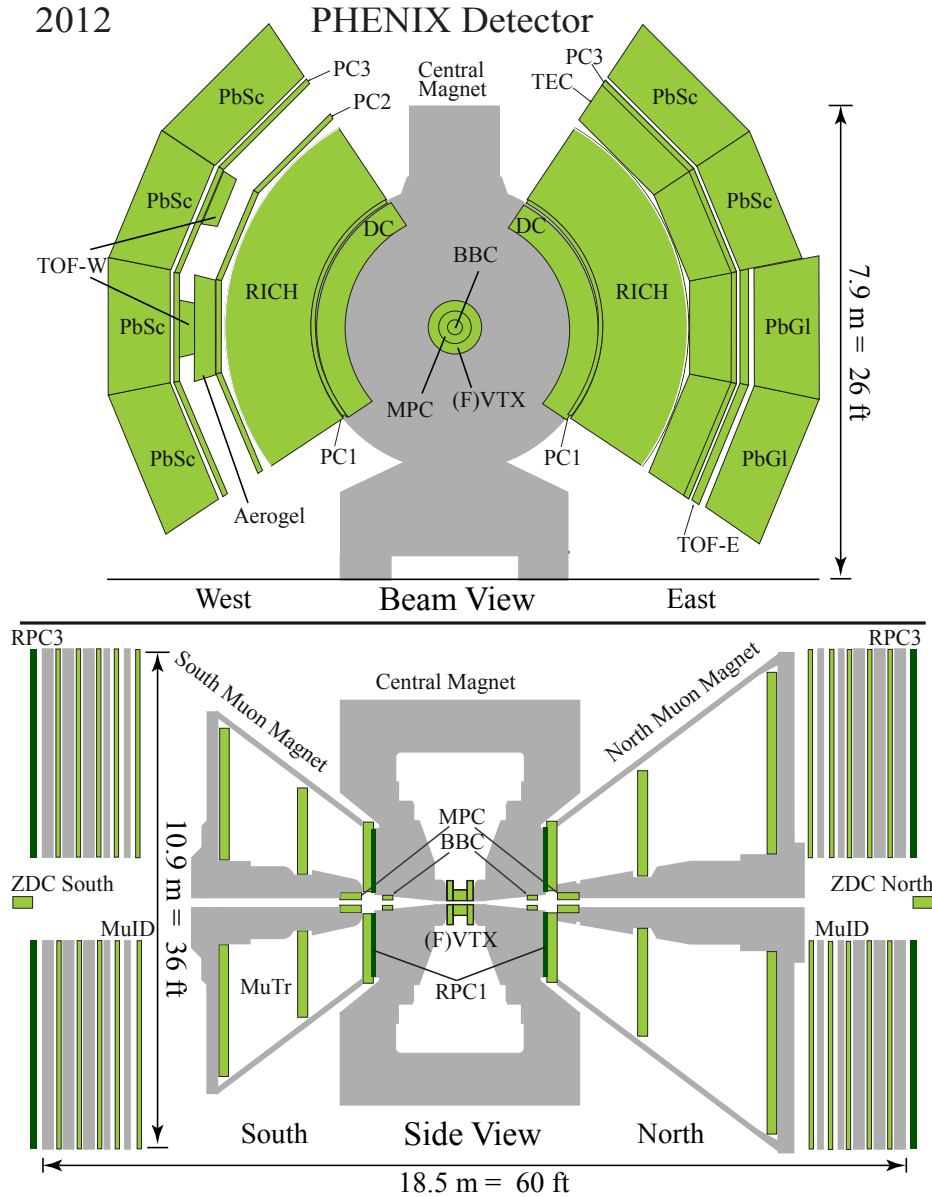


Figure 2.5: The PHENIX detector configuration for the 2012-2013 runs. The top panel is a view of the central arms as seen by looking along the axis of the beam direction. The bottom section highlights the two muon arms as seen from the side, perpendicular to the beam axis.



Figure 2.6: A drawing of one of the two BBC detectors.

2.2.2 Muon Arm Detectors

The forward muon arm spectrometers consist of three major components which will be explained in the following sections. They are the Muon Tracker (MuTr) detectors, the Muon Identifier (MuID) detectors and the Muon Arm Magnets. A complete schematic of one arm with the three components together is shown in Figure 2.7. The MuID is seen highlighted in green at the rear of the system, the magnet in yellow encompassing the MuTr and supports are shown for the complete system in cyan. The coalition of these subsystems allow for the measurement of deep penetrating muon particles while rejecting charged hadrons.

2.2.2.1 Muon Arm Magnets

The Muon Arm Magnets are a vital component for extracting momentum information about the muons. The magnetic field causes the muon to have an arced projection through the MuTr detector allowing the determination of the muon's momentum. The magnets them-

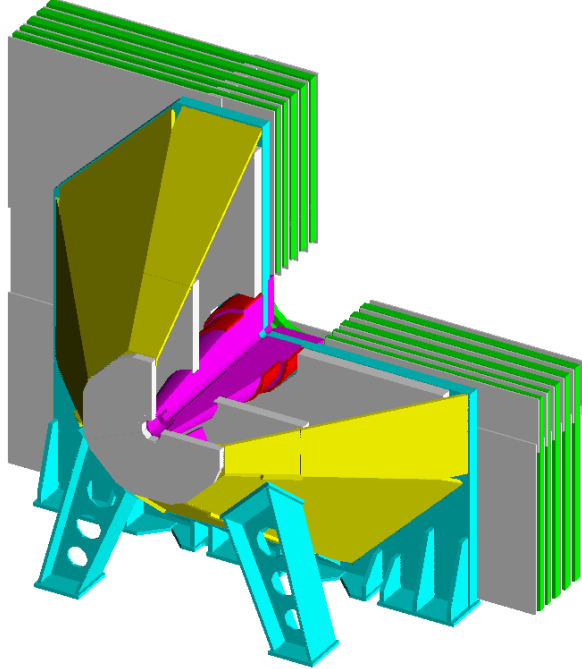


Figure 2.7: A drawing of one of the two muon arm detectors. The three components can be seen, they are the MuTr (grey), MuID (green) and Muon Arm Magnet (yellow and magenta).

selves are approximately three meters tall and have eight sides forming a frustum shape around the MuTr. There is a central piston that aligns with the beam axis with solenoidal coils wrapped around it in order to produce the magnetic field. The rear plates of the magnets serve a double purpose of being the flux return of the magnetic field as well as the first layer of the MuID detector (see Section 2.2.2.3). The central arm magnet also serves as the first layer of the hadronic absorber for the muon arm detectors. The radial magnetic field integral produced is 0.8 Tesla-meters. Ultimately, the magnets cover a kinematic region of $1.1 < |y| < 2.4$ and a full 2π in azimuth. The south arm magnet is 1.5 meters shorter than the north arm magnet which allows it to be moved for access to detectors embedded closer

to the IR (visible in Figure 2.5).

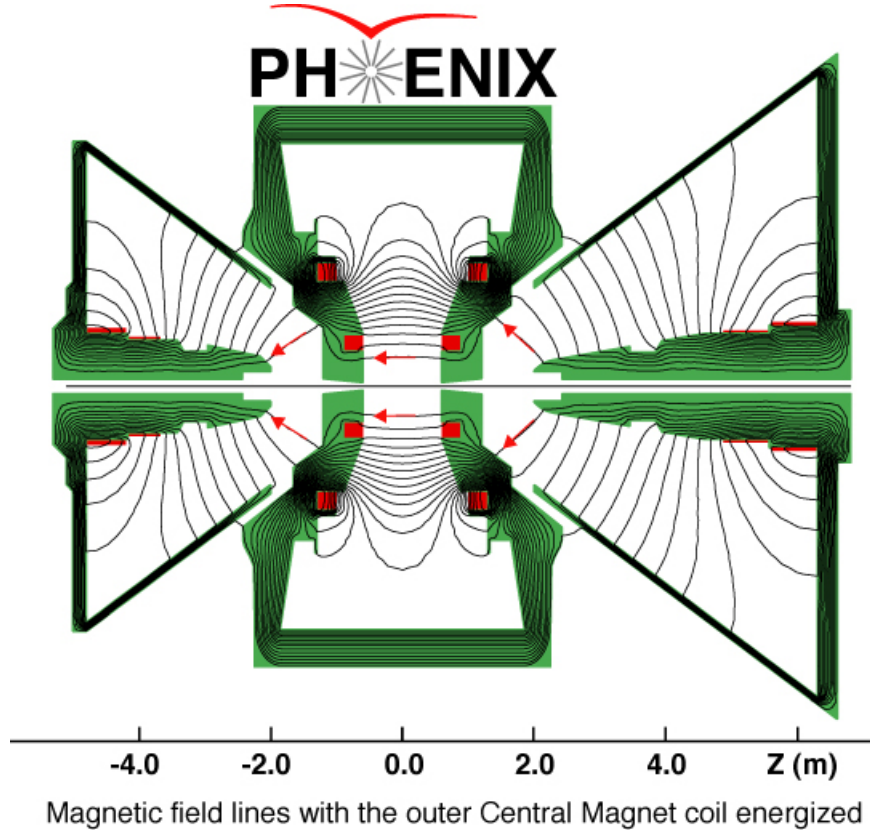


Figure 2.8: The field lines of the PHENIX magnet systems. The radial magnetic field can be seen in the Muon Arms.

2.2.2.2 Muon Tracker

After muons pass through the hadron absorbers, attached to the central magnet pole tips, muons encounter the MuTr at 1.25 meters from the nominal IR. The MuTr are made up of three stations of cathode strip chambers. Each station is increasingly larger than the previous one as can be seen in Figure 2.9 and the first station is constructed in quadrants while stations two and three are constructed in octants. Each consist of three layers of anode

wires sandwiched between cathode strips with a gas mixture of 50% $Ar + 30\% CO_2 + 20\% CF_4$ filling the chamber. The chambers are run with a high voltage of 1850 Volts and a gain $\approx 2 \times 10^4$. The three stations use an optical alignment system to keep the stations positions within $\pm 25 \mu m$ in order to maintain the desired momentum resolution of 1.5 GeV/c. The relative mass resolution ends up being $\sigma(M)/M = 6\%/\sqrt{M}$, M in GeV due to 100 μm muon position resolution [38].

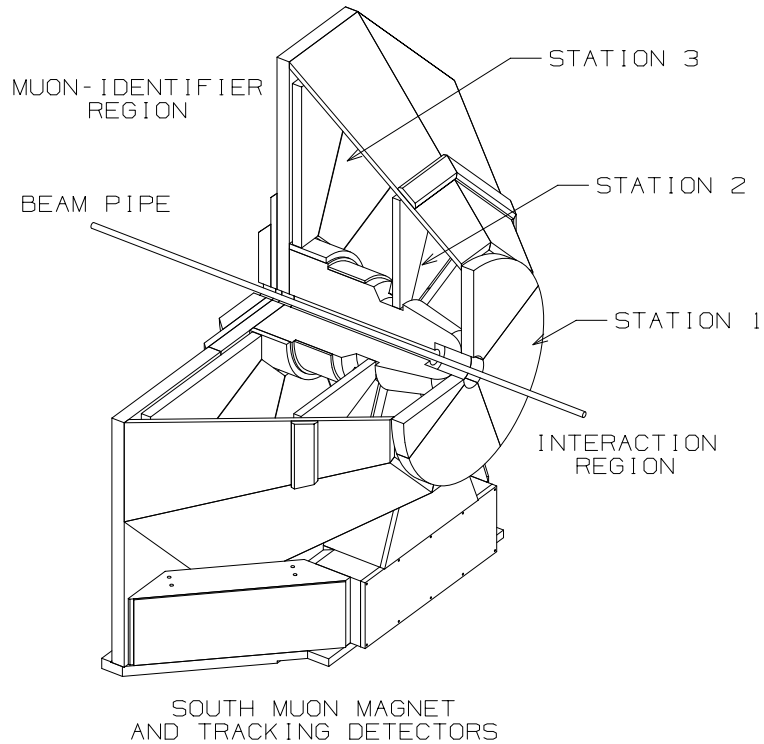


Figure 2.9: The south arm MuTr system with a cutout showing the three stations within the Muon Magnet and the beam pipe going through the center.

2.2.2.3 Muon Identifier

After muons and hadrons have penetrated through the back station of the MuTr, they encounter the MuID detector. This detector is designed to identify muon particles (and reject hadron particles in the process) serving as a trigger detector. It is made up of five alternating layers of Iarocci streamer tubes and steel absorber planes, each layer given the name “gap” and a corresponding number (0-4). The steel absorber layers are 10, 10, 20 and 20 cm thick for each steel layer between a gap (for both arms). In the north arm the magnet return plate is 30 cm, and in the south arm the return plate is 20 cm thick. There are additional steel absorbers added to the back side of the central magnet of 35 cm thickness to help reduce hadronic backgrounds. It takes a minimum muon momentum of 2.7 GeV/c to penetrate to the back of the detector [38]. Iarocci tubes are single anode wire tubes surrounded by a square cathode. They are filled with 92% CO_2 and 8% isobutane and run at a voltage of 4300-4500 Volts across them [9]. The tubes are combined into two arrays making up a “two-pack” as seen in Figure 2.10. The “two-packs” are then combined to make up six panels of each gap. They are combined so that the tubes have vertical and horizontal tubes within each panel. The panel layout of each gap can be seen in Figure 2.11. Panels 0, 2, 3 and 5 are the largest of the six and have 64 vertical and 59 horizontal two-packs. The two smaller panels, 1 and 4, consist of 26 vertical and 45 horizontal two-packs.

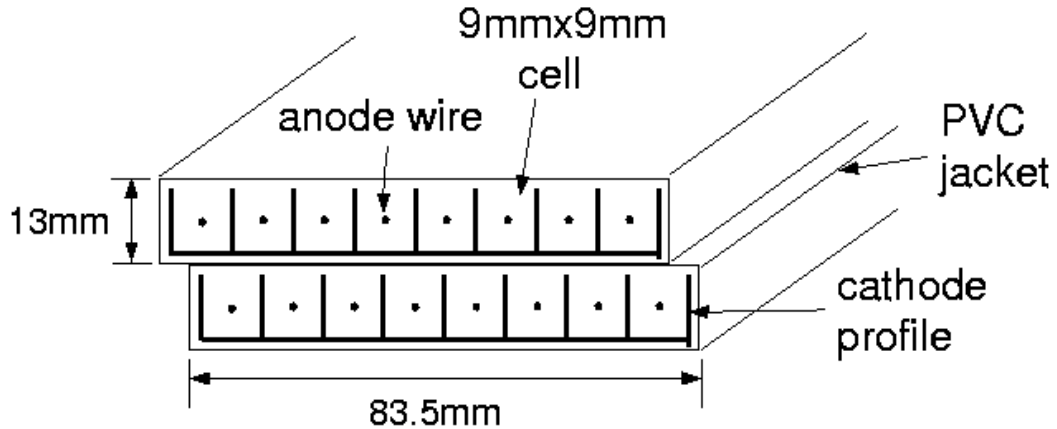


Figure 2.10: Schematic of Iarocci tubes used to makeup the MuID detector “two-pack”.

2.2.3 Data Acquisition and Processing

This section explains the data collection, triggering and processing procedure used by the PHENIX experiment. Data is collected during beam stores provided by CAD. It then needs to be converted into usable information for analyzers.

2.2.3.1 Data Acquisition

The PHENIX data acquisition (DAQ) system collects $\approx 60 - 90$ minutes worth of data at a time and assigns a “run” number to each block. The event collection rate is $\approx 6 - 9$ kHz. An

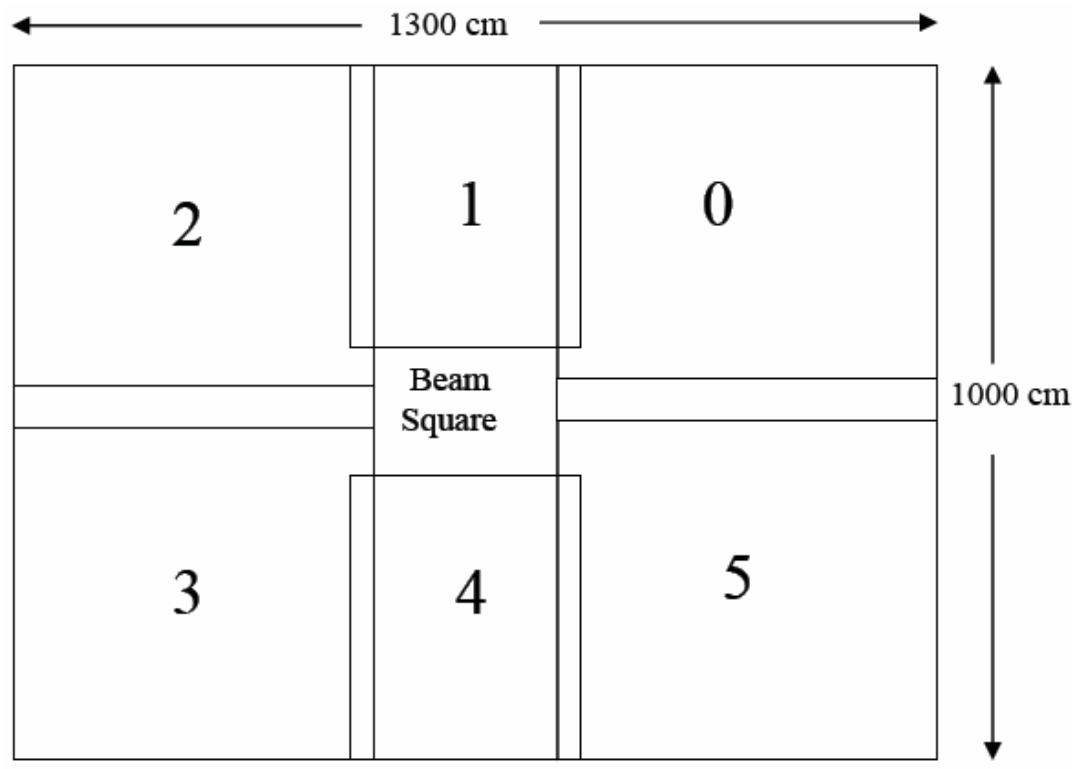


Figure 2.11: Layout of panels within the MuID detector

event is recorded when the BBC trigger is fired (see Section 2.2.1). The DAQ system was designed for both heavy ion and $p+p$ collisions which have very different event characteristics. Heavy ion collision event rates are on the kHz scale with large event multiplicity and $p+p$ collisions are on the MHz but with much smaller multiplicity. The flow of data acquisition is as follows.

The DAQ starts with the clock fed from the CAD department. Events occur in the IR and particles enter the corresponding detectors producing electronic signals. The events are then triggered on by the BBC, MuID (see Section 2.2.3.2) or other trigger system. If the

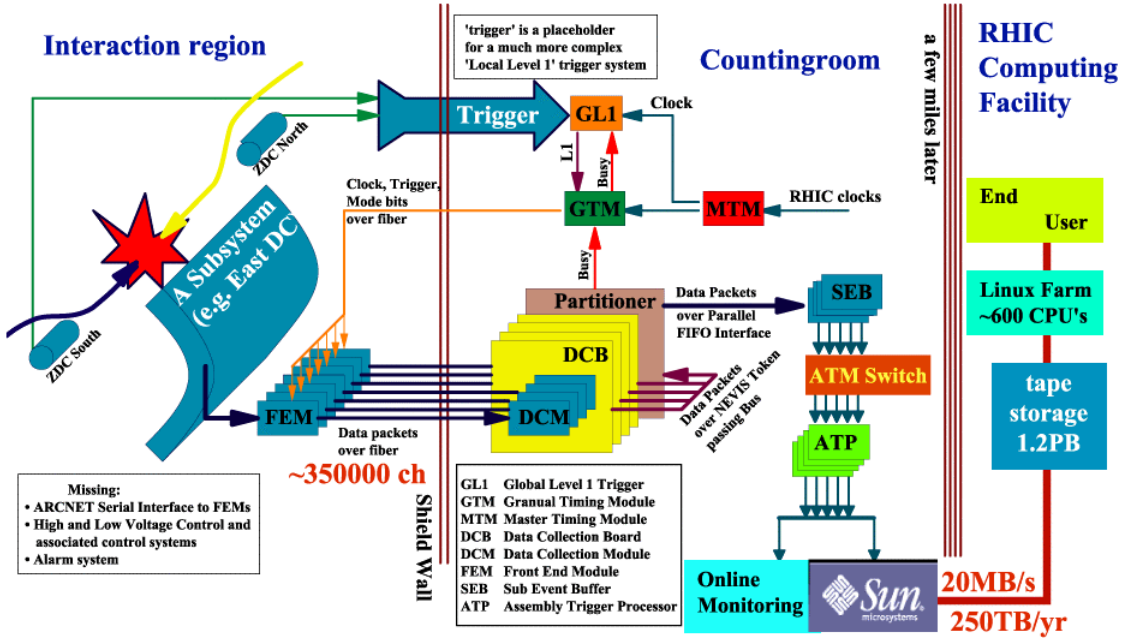


Figure 2.12: DAQ flow chart.

event is deemed good or interesting (based on specific triggers) then the event proceeds. If not, then the event is disregarded. Once the event passes the trigger(s), the analog signals from the detectors are sent to the Front End Modules (FEM) located within the IR. The FEMs collect data in real time and control the individual detector electronics. They digitize the triggered data and send it to the Data Collection Module (DCM) via optical cable into the rack room (≈ 20 meters away and behind protective concrete shielding). The DCM frees up the FEM for upcoming events and feeds the Data Collection Boards (DCB)/Partitioner the parallel subsystems event signal. The partitioner sends individual subsystem packets

in unison to the Sub Event Buffer (SEB) which holds the subsystem event. The SEB then sends an events worth of subsystems to the Assembly Trigger Processor (ATP) which builds whole event's with all the subsystems included. They are stored in PHENIX Raw Data Files (PRDF) which stores event by event information.

During data collection shift crews monitor the progress of the data collection in real time. The crew can tag good, bad and questionable runs to be considered during data production and analysis. PRDFs are also sent to storage in buffer boxes and eventually sent to RHIC computing facility to be stored (and backed up) on tape. This whole process is exhibited in Figure 2.12.

2.2.3.2 Muon Trigger

MuID Local Level One trigger (MuIDLL1) is determined using the MuID detector. It can run at 25 kHz limited only by the Front End Module (FEM) electronics (see Section 2.2.3). Information from each beam crossing is considered for the muon trigger. The trigger algorithm forms MuID “roads” (muon tracks determined from the hit pattern in each of the MuID gaps) that must point nominally at the collision vertex. The trigger accepts events that penetrate through to the back two gaps, either gap 3 or gap 4. Further requirements can include two muons to penetrate to the back of the detector in the same arm or opposite arms.

2.2.3.3 Data Production

Data is collected during runs and stored in PRDFs. These files contain raw detector hit information and need to be converted into physically meaningful particle paths through the detectors, known as tracks. PRDFs run through the PHENIX production codes producing Data Summary Tape (DST). Production is performed individually for both the central arm and the muon arm data. They can also have specific triggers applied to them. When produced, they are provided a production number for record keeping purposes. A brief description on muon data production is provided.

Muon data production starts with MuID detector information. The MuIDLL1 trigger has already removed some of the potential noise that would be seen in the MuTr before the absorbers. MuID “roads” are muon candidate tracks through the MuID detector. They are formed starting at the last gap (the back of the detector). Ideally a muon has triggered all planes of the MuID layers, (10 total, 5 layers each with x and y positioned tube planes). The MuID has no magnetic field so roads are straight trajectories. A road finding algorithm is then applied to find the best fit road to construct trajectories based on the detector hit information. The MuTr also forms muon candidate tracks and uses a seed provided by the MuID road. Hit clusters in the three tracker planes with the MuID seed are then run through the track finding algorithm. Fits to muon candidate MuTr tracks and MuID roads are then determined. The combination of tracks and roads form muon candidates which are used for analysis. Physical properties can then be determined from the candidates which are recorded in DST files and stored in central PHENIX repository. When an analyzer needs data from

the central repository they access the production through the “TAXI” which references the current analysis build (current set of PHENIX libraries).

2.2.3.4 Tracking Variables

Here is a list of some of the tracking variables that are given to muon candidates once they have been produced.

- **BBC_z(cm)** is the event vertex position along the z-axis as measured by the BBC detector.
- **DG0 (cm)** is the distance between the MuTr track and MuID road at the first MuID gap, as shown in Figure 2.13.
- **DDG0 (degrees)** is the angle difference between the MuTr road and the MuID track at the first MuID gap, as shown in Figure 2.13
- χ^2_{Tr} is the MuTr track fit quality.
- χ^2_{ID} is the MuID road fit quality.
- **N_{TrHits}** is the number of hits in the MuTr (out of a possible 16).
- **N_{IDHits}** is the number of hits in the MuID (out of a possible 10).
- **p_z(GeV/c)** is the momentum of the muon candidate along the direction of the z-axis
- **y** is the rapidity of the μ .
- **lastgap** requires that the muon candidate makes it to gap 4 of the MuID.

- $|\mathbf{DCA}_r|(\text{cm})$ is Distance of Closest Approach of the muon candidate track projection, in the radial direction, from the collision vertex.
- $|\mathbf{DCA}_z|(\text{cm})$ is the Distance of Closest Approach of the muon candidate track projection, in the z-axis direction, from the collision vertex.
- χ^2_{vtx} is the quality of fit of the dimuon candidate vertex with the event vertex.
- $\mathbf{p}_T(\text{GeV}/c)$ is the momentum of the dimuon candidate in the x-y plane of the detector system.

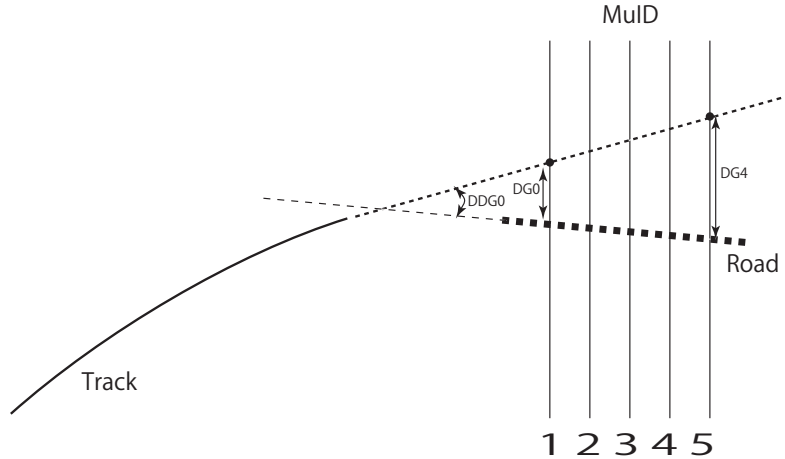


Figure 2.13: Diagram showing the definition of the DG0 and DDG0 cut parameters. The track coming from the left is from the MuTr and enters the MuID [9].

3**DATA ANALYSIS**

This chapter outlines the overall data set used, how it was studied to get a pure data sample, and how the data are corrected to account for detector effects. Also contained within the chapter is a description of how the signal is extracted. This includes an iterative combinatorial background subtraction technique and hadronic background estimations. Statistical uncertainties are represented throughout this thesis as one standard deviation of the mean. Finally, the signal is considered with different kinematic dependencies.

3.1 Dataset

This analysis is of $p+p$ data collected in 2013 at $\sqrt{s} = 510$ GeV, which was recorded between March 10 and June 10, using the PHENIX detectors. The data sample was produced using data production number 97 and has 3.6×10^9 events available on the TAXI. The TAXI was run (TAXI #12079) using the code that is found in the PHENIX CVS which are used to produce dimuon output (see Appendix B).

Dimuons were collected in the PHENIX muon arms using a dimuon trigger, which requires two muons (per event) to penetrate to the back of the MuID (gap 3 or gap 4) or that there is a muon in each arm (that makes it to gap 3 or gap 4) AND that the BBC, no vertex cut trigger is fired. The picoDST code is used to reconstruct single muons as well as make dimuon pairs. This module is also used to make the mixed-event pairs in which the single muons from different events, with similar event vertex positions, are paired together. The z-vertex used is within ± 30 cm of the origin, divided into bins with 2 cm widths and a pool

depth of four is used to mix the events (This is the default setting). Pool depth is the number of neighboring events that get mixed together. Mixed event pairs will be used to estimate combinatorial background.

The data then need to be “cleaned” to remove unwanted fake signals and portions with poor detector performance due to problems that could have occurred during data collection. A Quality and Assurance (QA) analysis is done to remove unwanted runs as well as determine a reference run which can be used for embedding simulations. Quality cuts are applied to remove unwanted noise that remains to help get the cleanest signal possible and help select pure muon candidates (and remove hadronic contributions). Finally, the data needs to be corrected to account for the loss of signal due to detector Acceptance and Reconstruction Efficiency ($A\epsilon$) of the detectors. QA, the cuts used and $A\epsilon$ are explained below in the follow Sections 3.1.1, 3.1.2 and 3.1.3, respectively.

3.1.1 Quality and Assurance

The Run 13 QA was done by the PHENIX $W \rightarrow \mu$ analysis group. They discarded runs based on the number of dead high voltage channels, hot/dead muon detector planes, and packets and based on input from the shift crew who recorded the data. Run **397293** was identified as representing “the average detector acceptance well”. This QA provided the collaboration with a list of 784 “good” runs.

An additional QA with a loose set of cuts (listed in Table 3.1) with the run list (of 784 runs) was carried out to look at dimuon event rates, north/south dimuon ratio and single muon kinematics. The distributions are shown below in Figures 3.1 through 3.13.

Considering the outcome of the second QA a new run list was obtained and these runs are listed in Appendix C. It removes runs in which a polarization measurement was made as well as runs where there was a significant deviation from the kinematics mean value. There are 601 good runs that survived all QA and were used in the analysis.

Table 3.1: Event, track and dimuon selection cuts used for the second QA

QA Cuts	North	South	
Event Cuts			
BBC_z	< 30	< 30	cm
Single Muon Selection Cuts			
DG0	< 14	< 22	cm
DDG0	< 10	< 10	degrees
χ^2_{Tr}	< 23	< 23	
N_{TrHits}	> 9	> 9	
N_{IDHits}	> 5	> 5	
p_z	> 2.4	> 2.4	GeV/c
Lastgap	> 3	> 3	
Dimuon Selection Cuts			
χ^2_{vtx}	< 5	< 5	
p_T	$0.0 < p_T < 7.0$	$0.0 < p_T < 7.0$	GeV/c

3.1.2 Data Quality and Assurance Cuts

Due to open heavy flavor being a continuum distribution in the like-sign invariant mass spectrum, it is difficult to optimize a set of quality cuts for this analysis. Therefore, the J/ψ signal is used to optimize the quality cuts that enhance the signal and reduce the signal

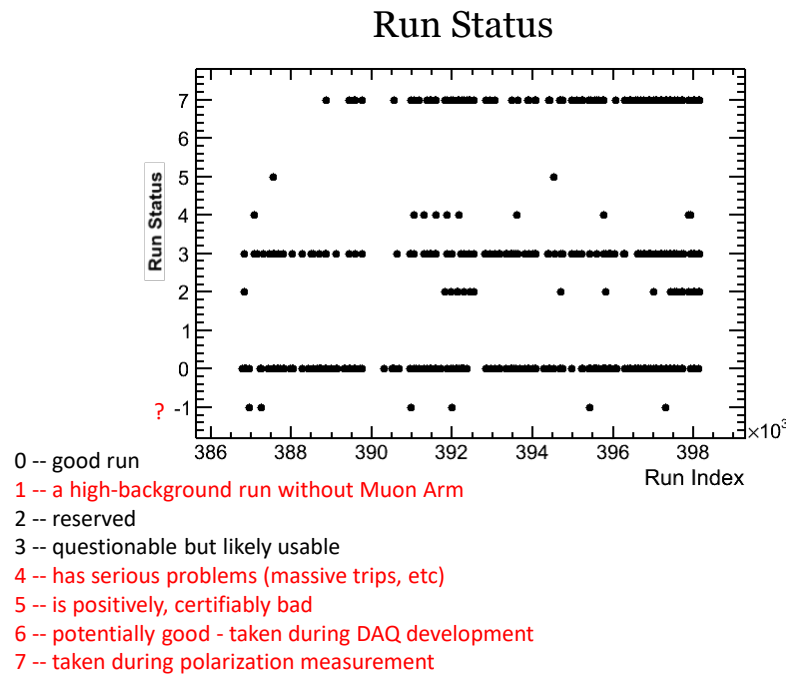


Figure 3.1: DAQ status marked by shift leader.

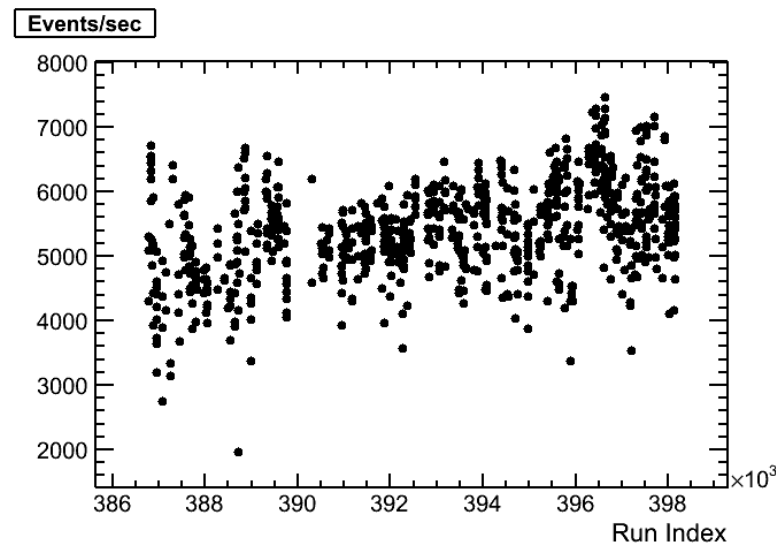


Figure 3.2: Dimuon event rate for each run.

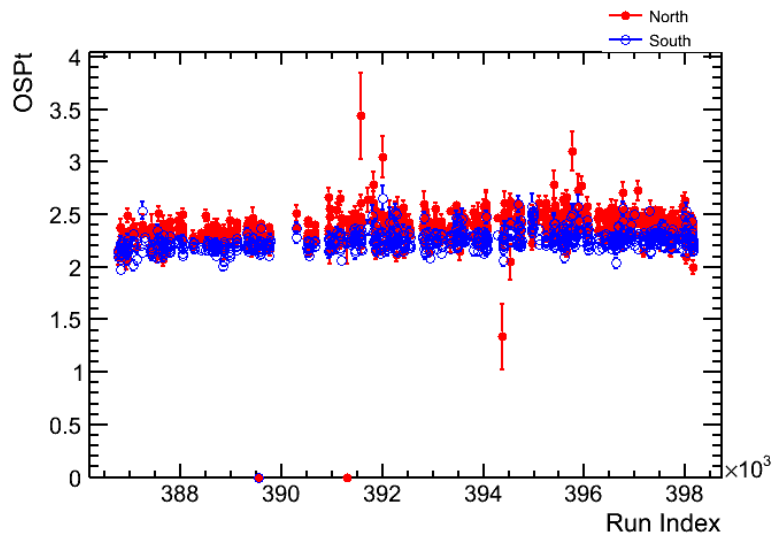


Figure 3.3: Dimuon mean p_T per run for the south arm (open blue circles) and for the north arm (closed red circles).

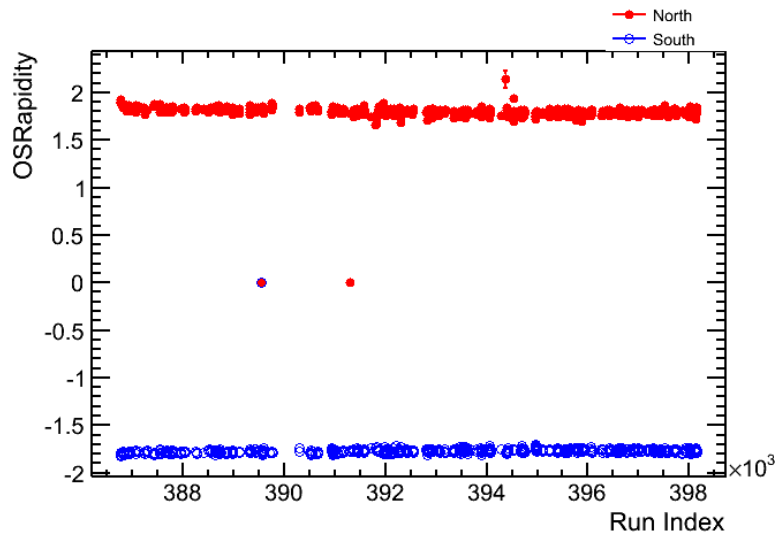


Figure 3.4: Dimuon mean y per run for the south arm (open blue circles) and for the north arm (closed red circles).

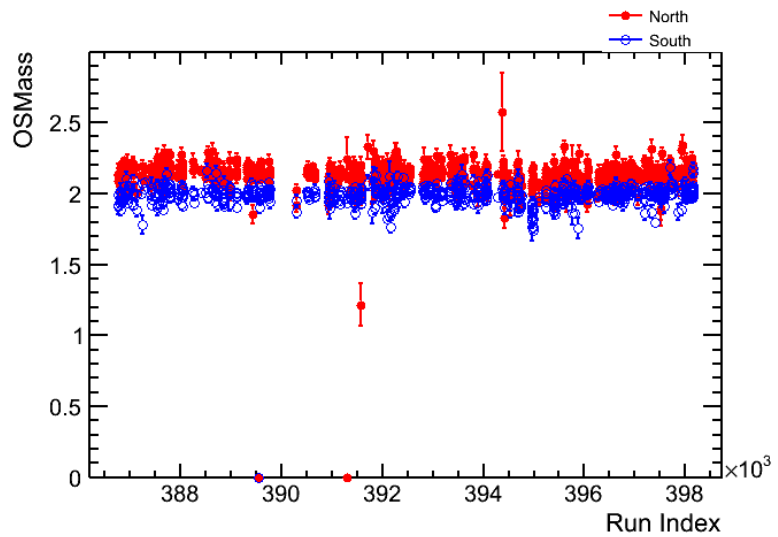


Figure 3.5: Dimuon mean mass per run for the south arm (open blue circles) and for the north arm (closed red circles).

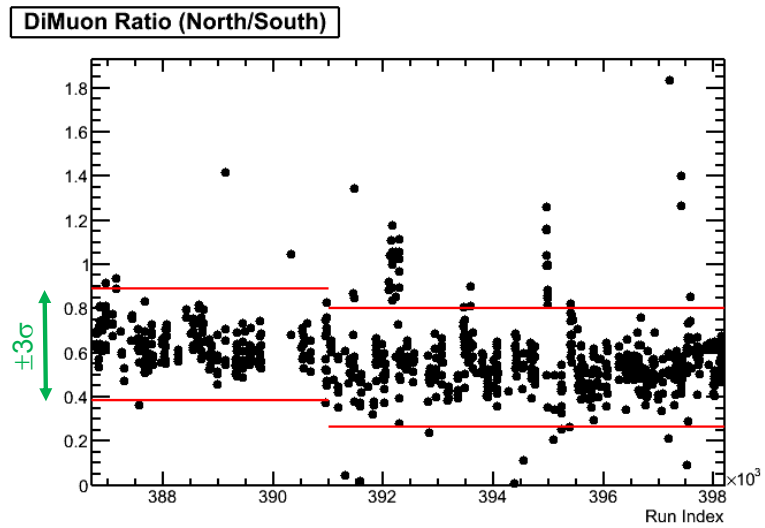


Figure 3.6: Dimuon ratio (north/south) per run.

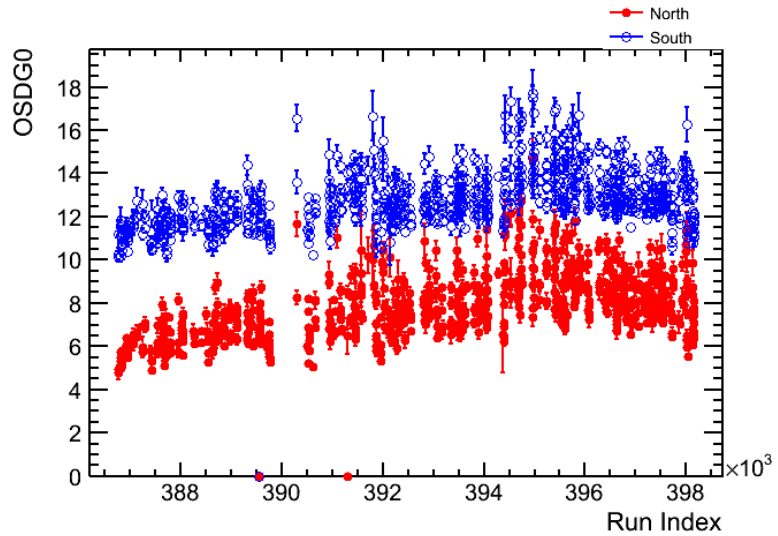


Figure 3.7: The mean of the single muon DG0 distributions for the north arm (closed red circles) and the south (open blue circles).

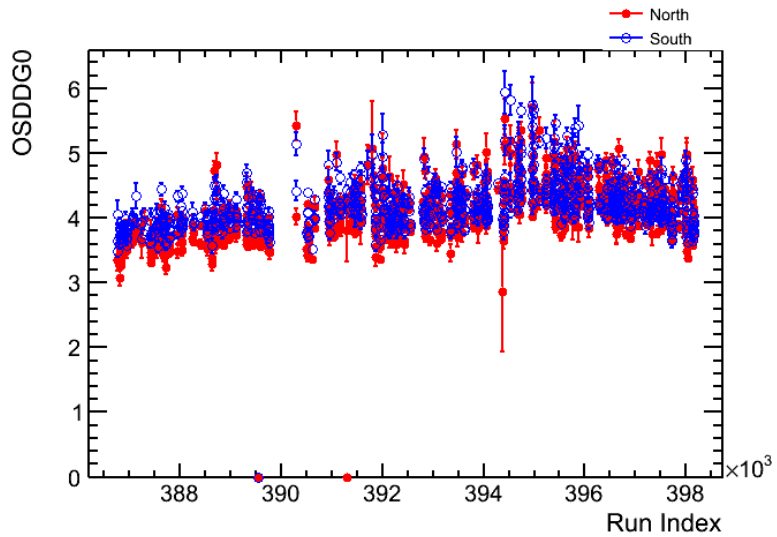


Figure 3.8: The mean of the single muon DDG0 distributions for the north arm (closed red circles) and the south (open blue circles).

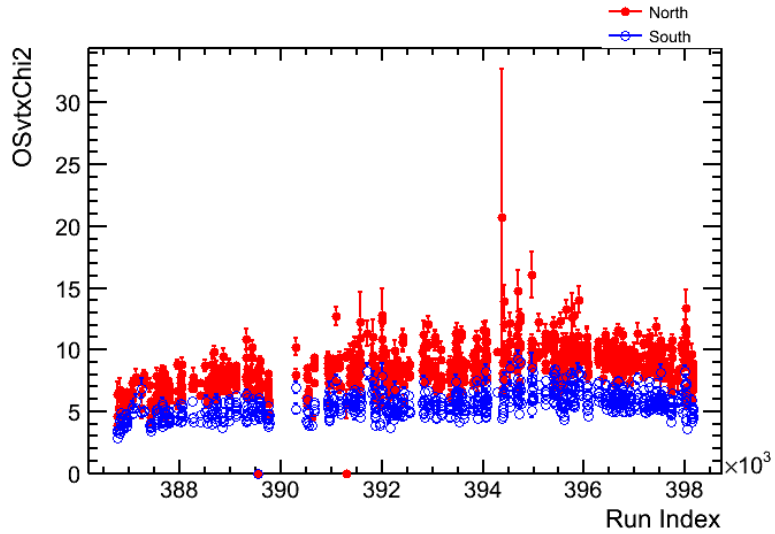


Figure 3.9: The mean of the single muon χ^2_{vtx} distributions for the north arm (closed red circles) and the south (open blue circles).

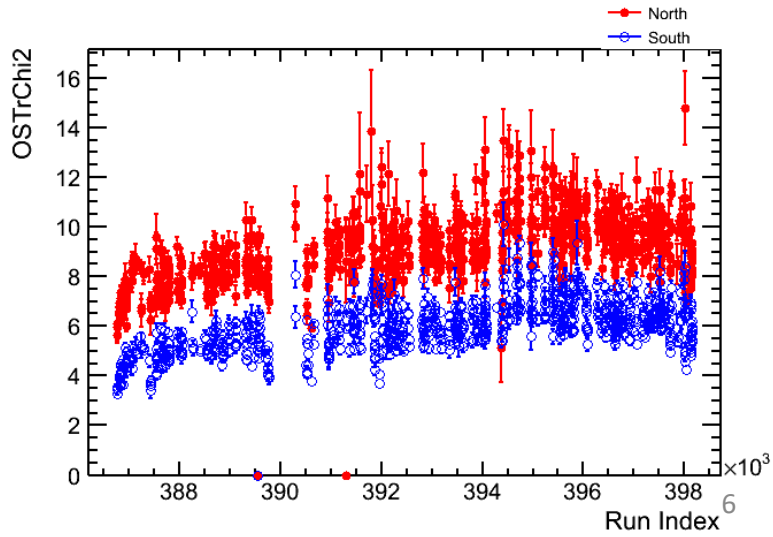


Figure 3.10: The mean of the single muon χ^2_{Tr} distributions for the north arm (closed red circles) and the south (open blue circles).

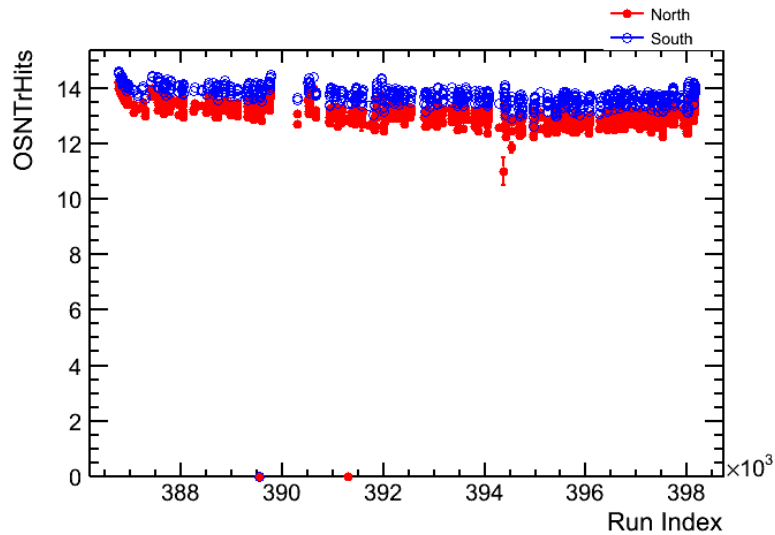


Figure 3.11: The mean of the single muon N_{TrHits} distributions for the north arm (closed red circles) and the south (open blue circles).

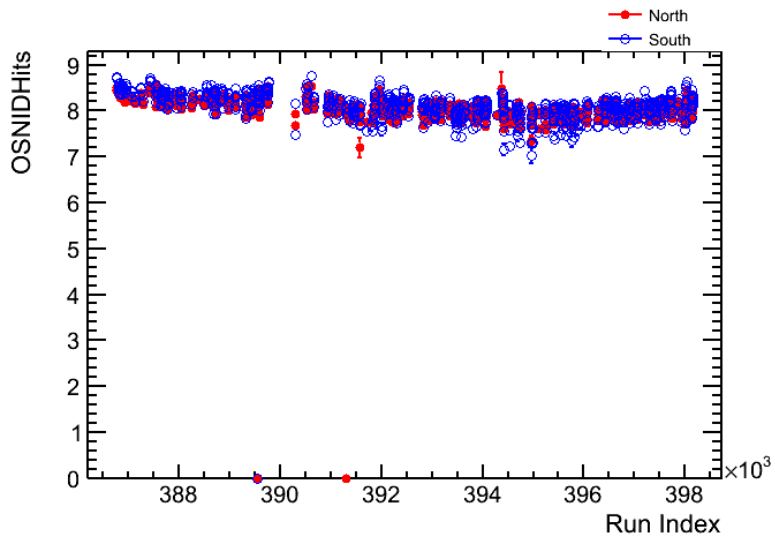


Figure 3.12: The mean of the single muon N_{IDHits} distributions for the north arm (closed red circles) and the south (open blue circles).

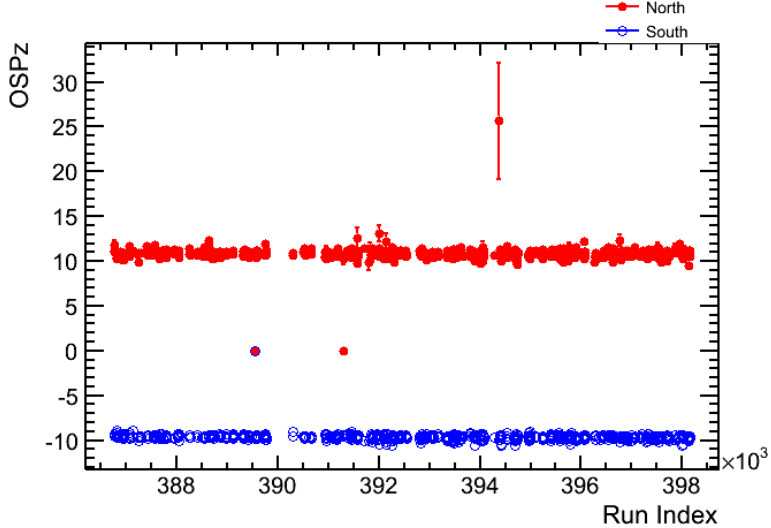


Figure 3.13: The mean of the single muon p_z distribution for the north arm (closed red circles) and the south (open blue circles).

to background ratio. The cuts were selected to keep as much of the J/ψ signal as possible ($\sim 99\%$) and were based on the impact of the cut on the resonance region yield. Those cuts were studied in both the data and PYTHIA embedding simulations (see Section 1.4). Table 3.2 summarizes the chosen cuts and Figures 3.14 through 3.23 shows how they were selected. While the determined cuts seem reasonable in relation to the signal of the J/ψ meson, they did not provide the best possible open bottom signal in the like-sign dimuon signal and the cuts were adjusted based on the like-sign dimuon yield once combinatorial background was removed. The final cuts are listed in Table 3.3.

Table 3.2: Event, track and dimuon selection cuts as determined with the J/ψ signal.

Cuts	North	South	
Event Cuts			
BBC_z	< 30	< 30	cm
Single Muon Selection Cuts			
DG0	< 14	< 28	cm
DDG0	< 11	< 10	degrees
χ^2_{Tr}	< 22	< 20	
χ^2_{ID}	< 10	< 10	
N_{TrHits}	> 9	> 9	
N_{IDHits}	> 5	> 5	
p_z	> 2.8	> 2.7	GeV/c
p_T	> 0.8	> 0.8	GeV/c
y	$1.2 < y < 2.2$	$-2.2 < y < -1.2$	
Lastgap	> 3	> 3	
Dimuon Selection Cuts			
χ^2_{vtx}	< 4	< 4	
p_T	> 0.5	> 0.5	GeV/c

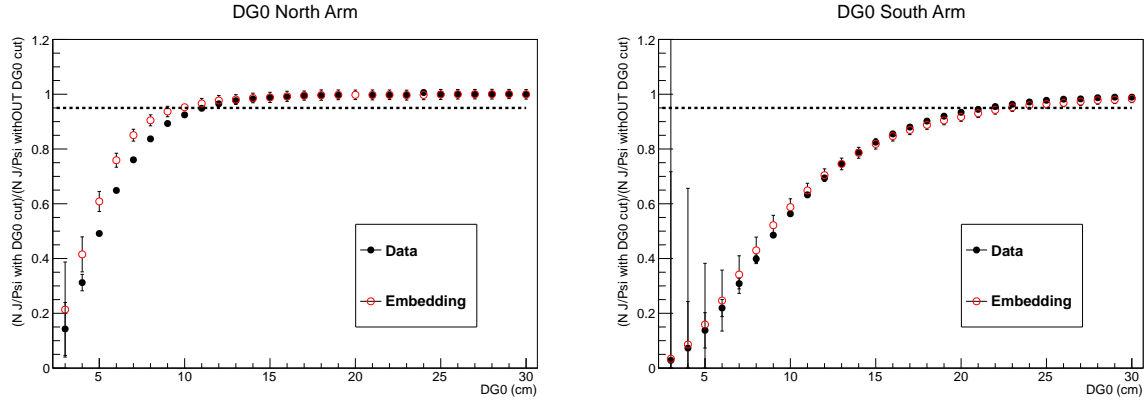


Figure 3.14: The ratio of J/ψ signal with DG0 cut to J/ψ signal without DG0 cut for the north arm (left) and south arm (right). The data are shown in solid black circles while the simulations are shown in empty red circles.

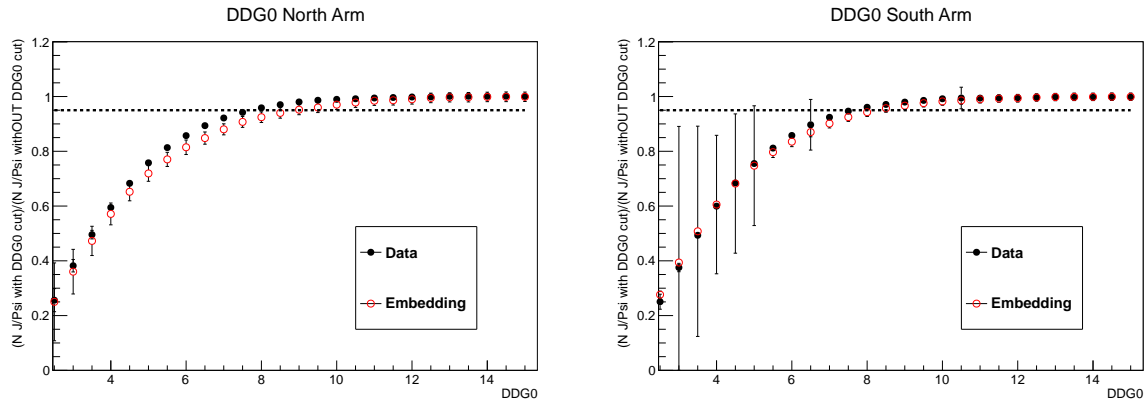


Figure 3.15: The ratio of J/ψ signal with DDG0 cut to J/ψ signal without DDG0 cut for the north arm (left) and south arm (right). The data are shown in solid black circles while the simulations are shown in empty red circles.

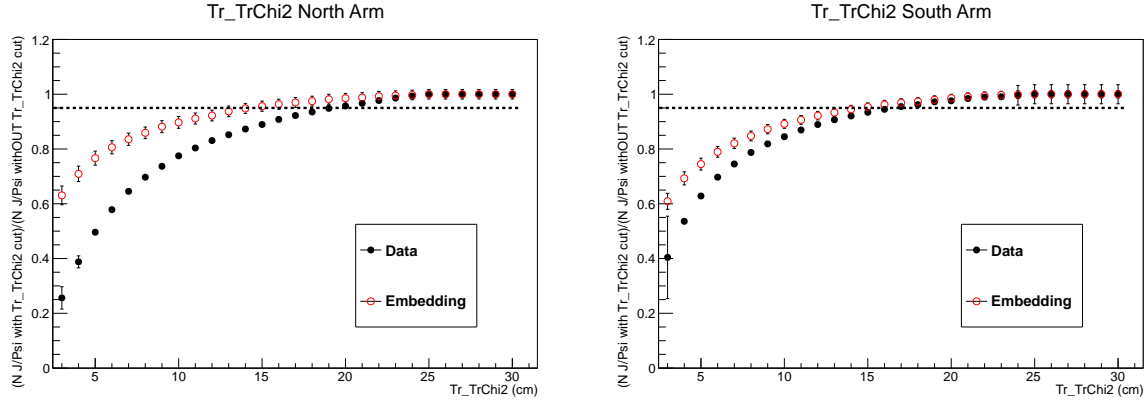


Figure 3.16: The ratio of J/ψ signal with χ^2_{Tr} cut to J/ψ signal without χ^2_{Tr} cut for the north arm (left) and south arm (right). The data are shown in solid black circles while the simulations are shown in empty red circles.

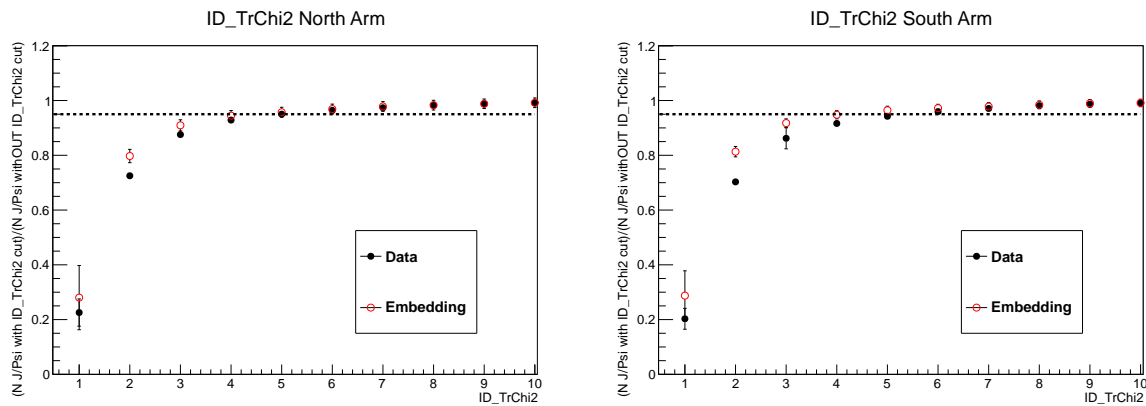


Figure 3.17: The ratio of J/ψ signal with χ^2_{ID} cut to J/ψ signal without χ^2_{ID} cut for the north arm (left) and south arm (right). The data are shown in solid black circles while the simulations are shown in empty red circles.

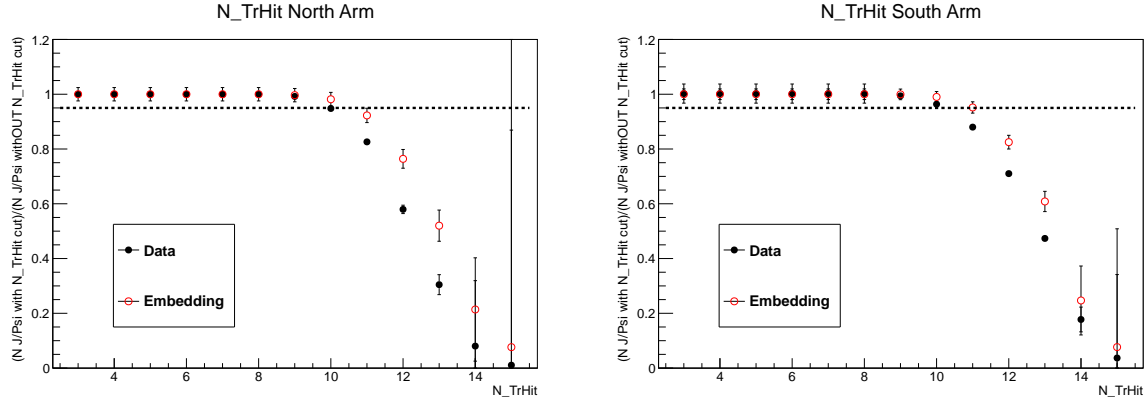


Figure 3.18: The ratio of J/ψ signal with N_{TrHits} cut to J/ψ signal without N_{TrHits} cut for the north arm (left) and south arm (right). The data are shown in solid black circles while the simulations are shown in empty red circles.

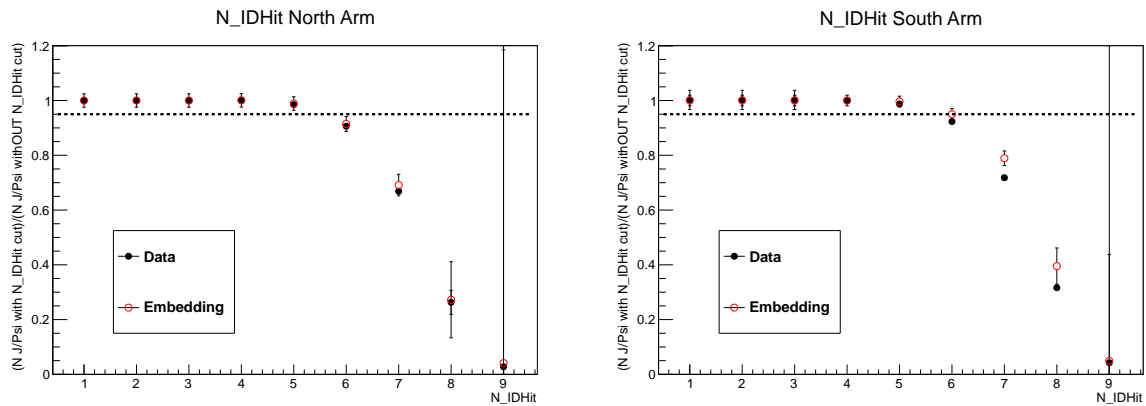


Figure 3.19: The ratio of J/ψ signal with N_{IDHits} cut to J/ψ signal without N_{IDHits} cut for the north arm (left) and south arm (right). The data are shown in solid black circles while the simulations are shown in empty red circles.

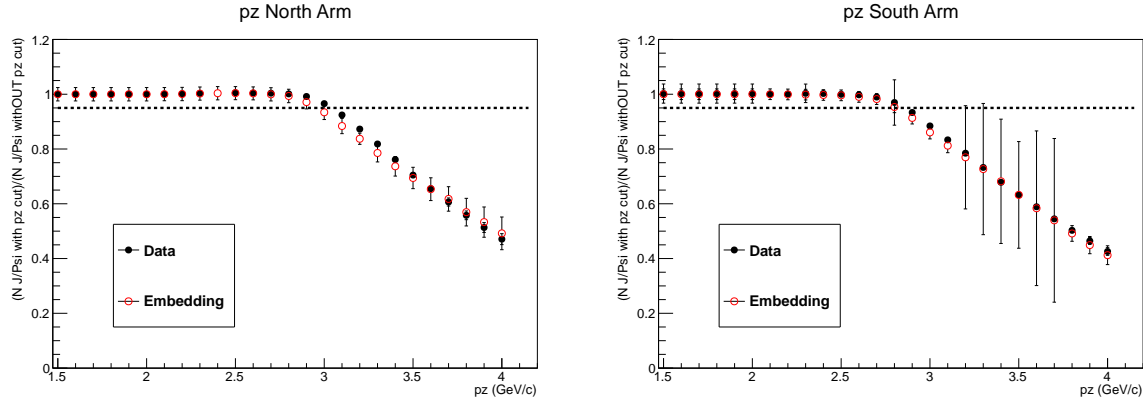


Figure 3.20: The ratio of J/ψ signal with p_z cut to J/ψ signal without p_z cut for the north arm (left) and south arm (right). The data are shown in solid black circles while the simulations are shown in empty red circles.

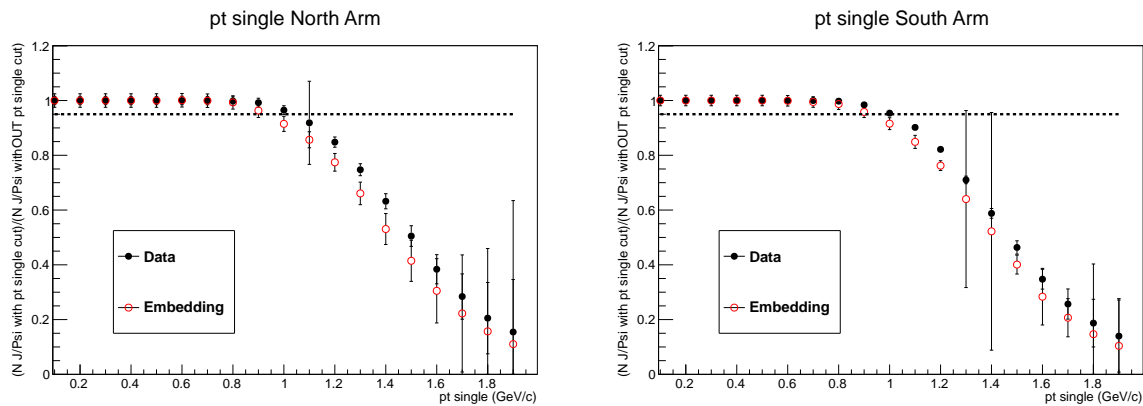


Figure 3.21: The ratio of J/ψ signal with single p_T cut to J/ψ signal without single p_T cut for the north arm (left) and south arm (right). The data are shown in solid black circles while the simulations are shown in empty red circles.

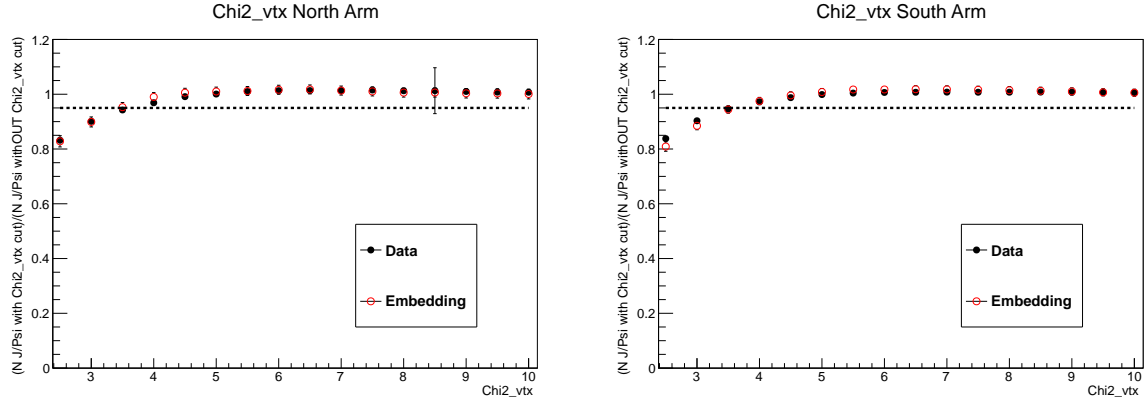


Figure 3.22: The ratio of J/ψ signal with χ^2_{vtx} cut to J/ψ signal without χ^2_{vtx} cut for the north arm (left) and south arm (right). The data are shown in solid black circles while the simulations are shown in empty red circles.

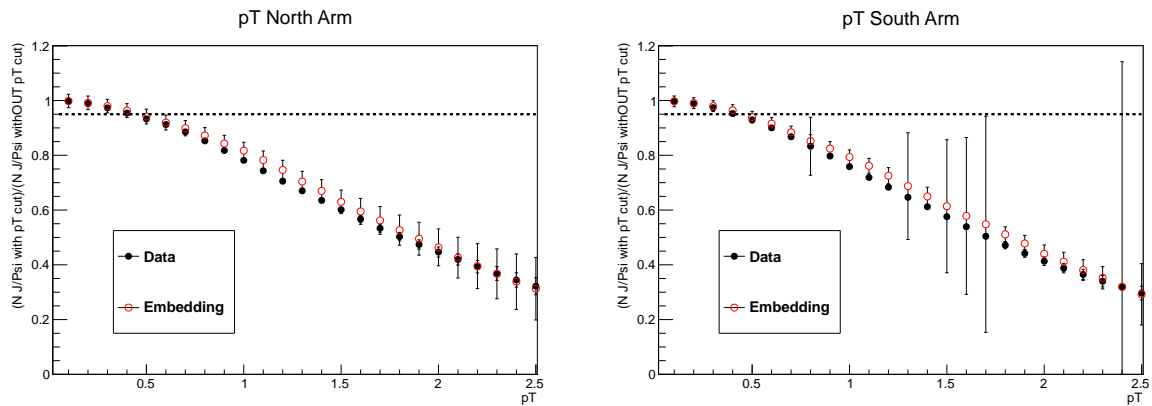


Figure 3.23: The ratio of J/ψ signal with dimuon p_T cut to J/ψ signal without dimuon p_T cut for the north arm (left) and south arm (right). The data are shown in solid black circles while the simulations are shown in empty red circles.

Table 3.3: Final event, track and dimuon selection cuts used in the analysis

Final Cuts	North	South	
Event Cuts			
BBC _z	< 30	< 30	cm
Single Muon Selection Cuts			
DG0	< 15	< 20	cm
DDG0	< 10	< 10	degrees
χ^2_{Tr}	< 23	< 23	
N_{TrHits}	> 9	> 9	
N_{IDHits}	> 6	> 6	
p_z	> 3.1	> 3.0	GeV/c
$ DCA_r $	$-5.0 < DCA_r < 10.0$	$-5.0 < DCA_r < 10.0$	cm
$ DCA_z $	< 30.0	< 30.0	cm
Lastgap	> 3	> 3	
Dimuon Selection Cuts			
χ^2_{vtx}	< 8	< 6	
y	$1.2 < y < 2.2$	$-2.2 < y < -1.2$	
p_T	$1.0 < p_T < 9.0$	$1.0 < p_T < 9.0$	GeV/c

3.1.3 Acceptance and Reconstruction Efficiency

The $A\epsilon$ of the muon spectrometers is determined by running a like-sign dimuon event generator, developed at GSU, through a full GEANT simulation of the PHENIX detector. These dimuons events were generated with flat dimuon mass distribution between 0.02-20 GeV/c² and p_T (0-15 GeV/c) and rapidity ($0.0 < |y| < 5.0$) distributions extracted from the data (see Figure 3.24). The vertex distribution was sampled based on a Run 13 BBC_z vertex distribution (see Figure 3.25). The generated events are then run through PISA (Run 13, 510 GeV detector setup) and real $p+p$ data is embedded into the simulation.

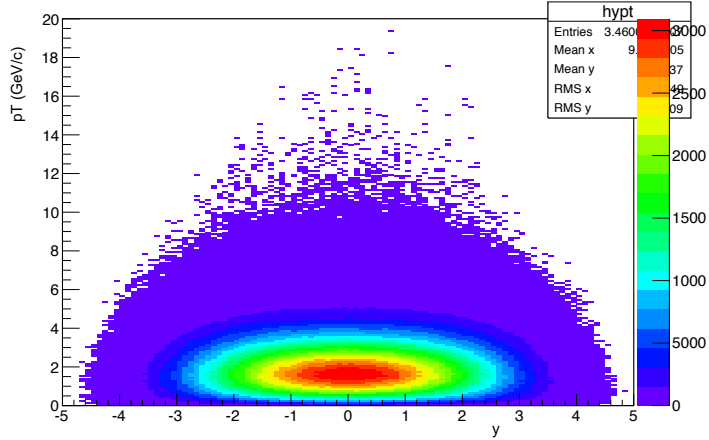


Figure 3.24: Input kinematics of dimuon generator simulation.

Run number 397293 was used for embedding which is commonly used throughout other Run 13 $p+p$ muon arm analyses. Therefore, run number 397293 detector dead maps were used since they have a reasonable description of the average detector acceptance, and vary detector hit efficiency for different collision rates. To be consistent with the real data analysis,

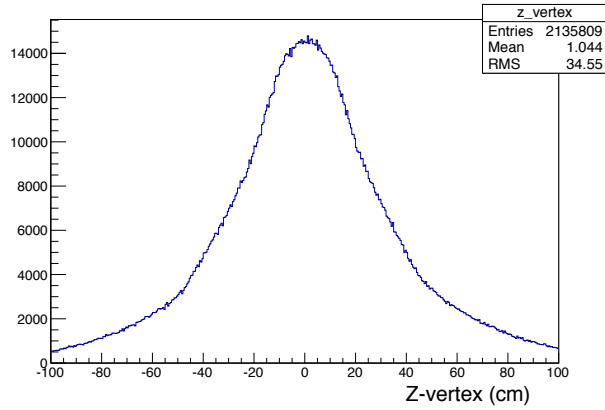


Figure 3.25: BBC_z vertex distribution from run number 397293.

the same code that was used for the real data analysis was used for the simulation analysis. The same data quality cuts were also used for the simulation. As a crosscheck, several single muon and dimuon distributions from simulation were matched to those from the data. This comparison uses the final cuts and the original run list from the $W \rightarrow \mu$ group. It shows very good agreement between data and simulation and gives us confidence in using the simulation to calculate $A\epsilon$.

The $A\epsilon$ was calculated by dividing the number of reconstructed events by the number of generated events in a given kinematic bin. The average $A\epsilon$ for like-sign pairs as a function of mass and $\Delta\phi$ is shown in Figure 3.27.

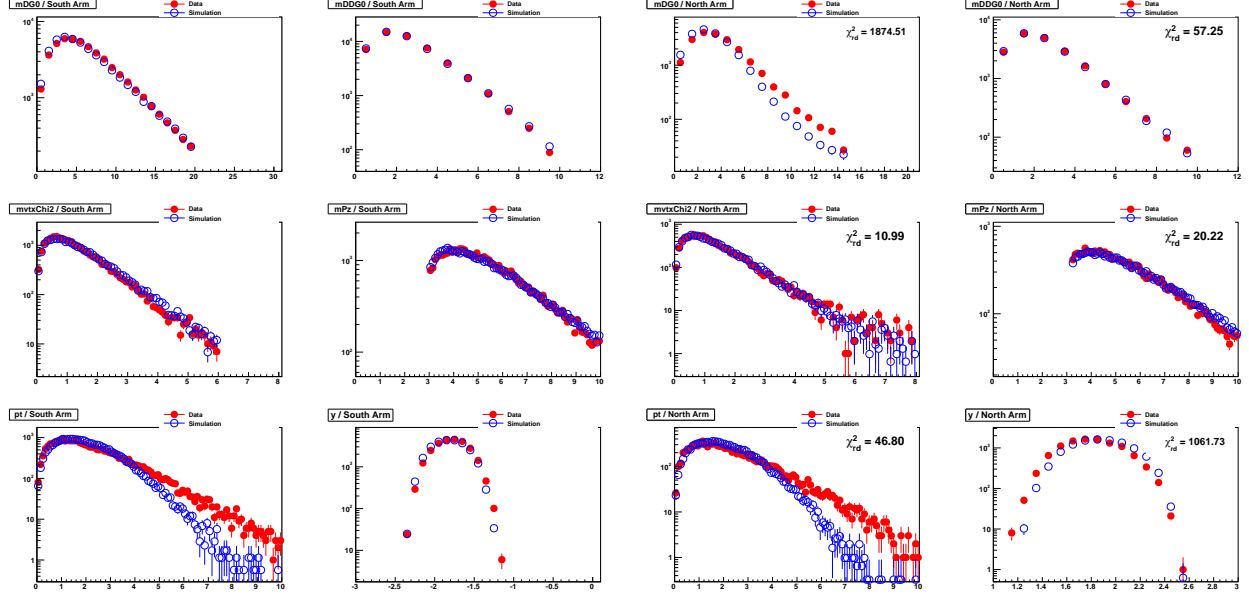


Figure 3.26: Single and dimuon kinematic distributions comparison between data (solid red circles) and embedded simulation (empty blue circles) from the north (left) and south (right) arms. These variables include DG0, DDG0, χ^2_{vtx} , p_z , p_T and y .

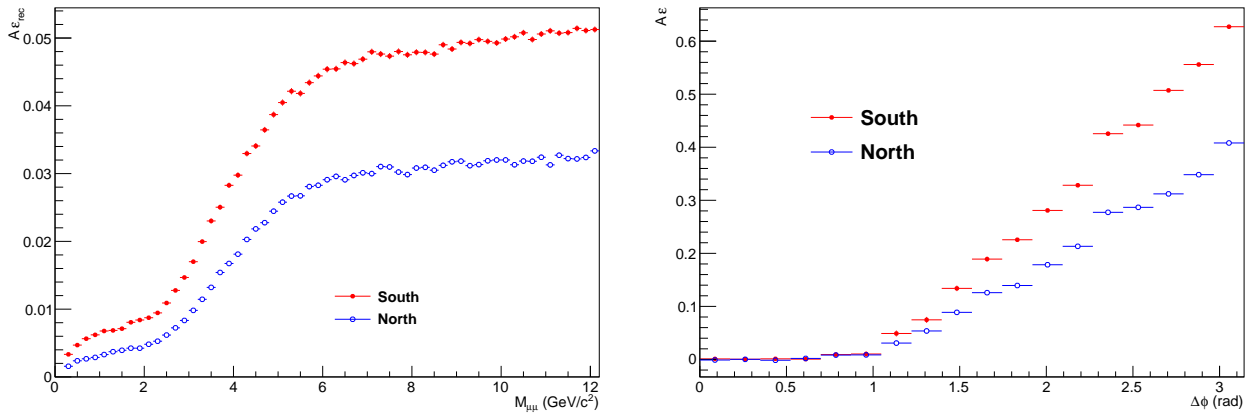


Figure 3.27: $A\epsilon$ for like-sign dimuons as a function of mass (left) and as a function of $\Delta\phi$ (right). The south arm is shown in solid red circles while the north arm is shown in empty blue circles.

3.2 Signal Extraction

The analysis focuses on the like-sign dimuon signal in the continuum mass region 5-10 GeV/c², which includes:

- bottom (signal) pairs
- charm pairs, in the low mass, low p_T kinematic region. (a negligible contribution)
- combinatorial background
- correlated hadronic backgrounds from high momentum punch through hadrons and light meson decays in which the decay occurs prior to the MuTr steel absorbers

The main goal of this analysis is to extract the $b\bar{b}$ pairs from the like-sign dimuon continuum, called the foreground. The charm pairs are negligible in the mass region of interest, 5-10 GeV/c²; the combinatorial and correlated backgrounds are have non-negligible contributions and need to be removed. The combinatorial background is subtracted using the mixed-event technique while the hadronic backgrounds are estimated with PYTHIA+PISA simulations with the simulation inputs compared to previous experimental data [39]. In this section, we summarize the procedures of treating these backgrounds.

3.2.1 Combinatorial Background

3.2.1.1 Mass dependence

The combinatorial background is emulated by event mixing. This is done by pairing muons in the current event with those of the same sign from previous events that have a similar event

vertex position (vertex bin). Because pairs are made from separate events, these are exclusively combinatorial pairs. The analysis of mixed-event pairs was performed using the same cut selections as the same event pairs (see Table 3.3). However, the mixed-event spectrum needs to be normalized before being subtracted from the like-sign foreground spectrum. This is done in the low mass region so that the contribution of correlated like-sign pairs is negligible. Since, the specific range of the low mass region where the contribution of correlated like-sign pairs is negligible is not well defined; we use four different normalization windows concentrated in the low mass region and obtain a normalization factor for each window. These windows include: [0.5,2.6], [0.5,3.6], [2.6,3.6], and [1.6,4.2] GeV/c^2 . The normalization window is not allowed to extend beyond 4.2 GeV/c^2 because the $b\bar{b}$ signal of interest is dominant in the higher mass region. The process is done iteratively and summarized in the following steps:

- First, the mixed-event spectrum is normalized by the ratio of the number of events in the foreground spectrum (N^{FG}) to those in the mixed-events spectrum (N^{BG}) in the low mass windows, N^{FG}/N^{BG} . The general normalization factor, R , that is used to normalize the mixed-events spectra, is the average of these four normalization factors. The first iteration's signal spectrum is the difference between the foreground and normalized mixed-events spectra. This first step is summarized in Equation 3.1 and the

result is shown in Figure 3.28.

$$\left. \begin{aligned} N^{FG} &= \int_{m_i}^{m_f} n_{FG} dn \\ N^{BG} &= \int_{m_i}^{m_f} n_{BG} dn \\ R_{0,j} &= \frac{N_j^{FG}}{N_j^{BG}} \\ R_0 &= \frac{R_{0,0} + R_{0,1} + R_{0,2} + R_{0,3}}{4} \end{aligned} \right\} \quad (3.1)$$

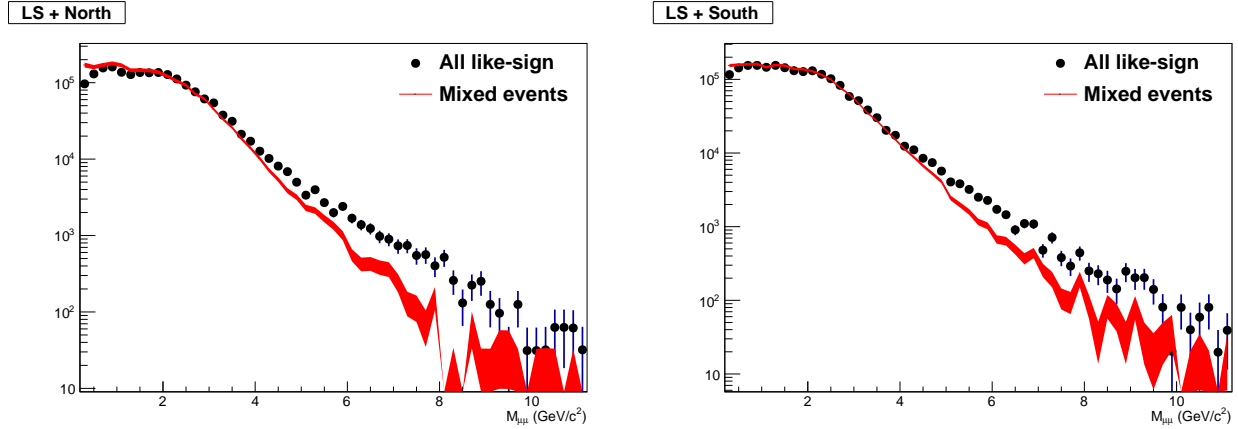


Figure 3.28: The invariant mass spectra for like-sign pairs from the same event (solid black circles) and mixed-events (red band) for the north (left) and south (right) arms after applying the normalization factor to the mixed-events spectrum.

As mentioned, the specific range where the signal of interest is negligible is not well known, and to further improve the normalization factor we utilize the $b\bar{b}$ invariant mass distribution shape from PYTHIA 8 simulation (See settings used in Appendix E). Like-sign pairs from open bottom contributions where then made with the single muon p_T cut (1 GeV/c) applied.

- Next, the $b\bar{b}$ spectrum is normalized to signal spectra in the $b\bar{b}$ signal region, 5 – 10

GeV/c². Then, the normalization factor (previously calculated as N^{FG}/N^{BG}) is adjusted ($N^{FG}/(N^{BG} - N^{BB})$, where N^{BB} is the number of events within the studied windows. This step is summarized in Equation 3.2 and the result is shown in Figure 3.29.

$$\left. \begin{aligned}
 N_{SR}^{SG} &= \int_5^{10} n_{SG} dn \\
 N_{SR}^{BB} &= \int_5^{10} n_{BB} dn \\
 R_{SG} &= \frac{N_{SR}^{SG}}{N_{SR}^{BB}} \\
 N^{BB} &= \int_{m_i}^{m_f} R_{SG} \times n_{BB} dn \\
 R_{1,j} &= \frac{N_j^{FG}}{N_j^{BG} - N_j^{BB}} \\
 R_1 &= \frac{N_{1,0} + N_{1,1} + N_{1,2} + N_{1,3}}{4}
 \end{aligned} \right\} \quad (3.2)$$

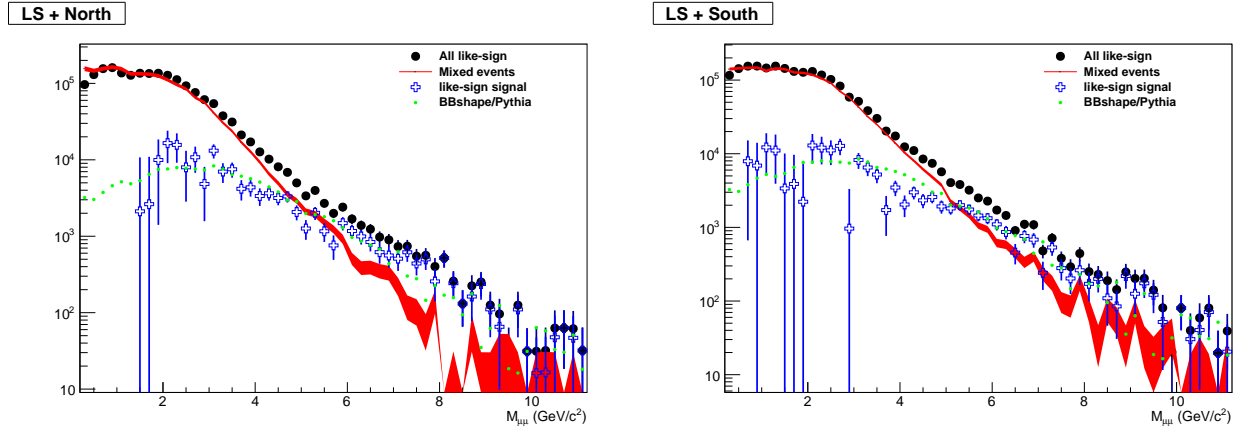


Figure 3.29: The invariant mass spectra for like-sign pairs from the same event (solid black circles) and mixed-events (red band), and the difference (empty blue sign) for the north (left) and south (right) arms after applying the normalization factor to the mixed-events spectrum. The figure also shows the $b\bar{b}$ spectrum (green points)

The second step is then repeated until the value of the mixed-events normalization factor

converges, as shown in Figure 3.30. The change in the normalization factor gets smaller after the first step and converges after the fourth iteration to the values; $R_{north} = 2.13$ and $R_{south} = 2.16$.

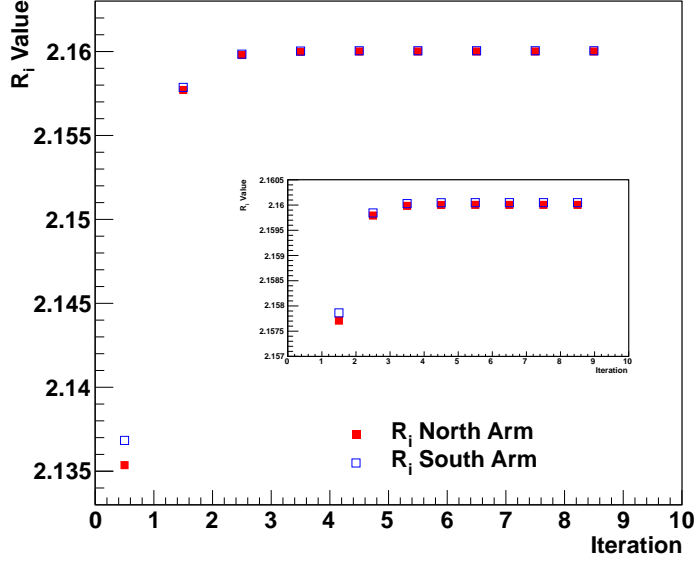


Figure 3.30: The mixed-events normalization factor, R , for the different iterations studied for the north (solid red squares) and south (empty blue squares) arms. The insert shows a zoom in on higher iterations.

The left panel of Figure 3.31 shows the results after several steps. Since the resulting spectra from the north and south arms are corrected for $A\epsilon$, they are expected to be consistent. This assumes that the hadronic background is either very small and/or the same in both arms. Figure 3.32 shows a comparison of the north and south arms signal spectra and they are quite consistent implying the assumptions on the hadronic backgrounds to be correct.

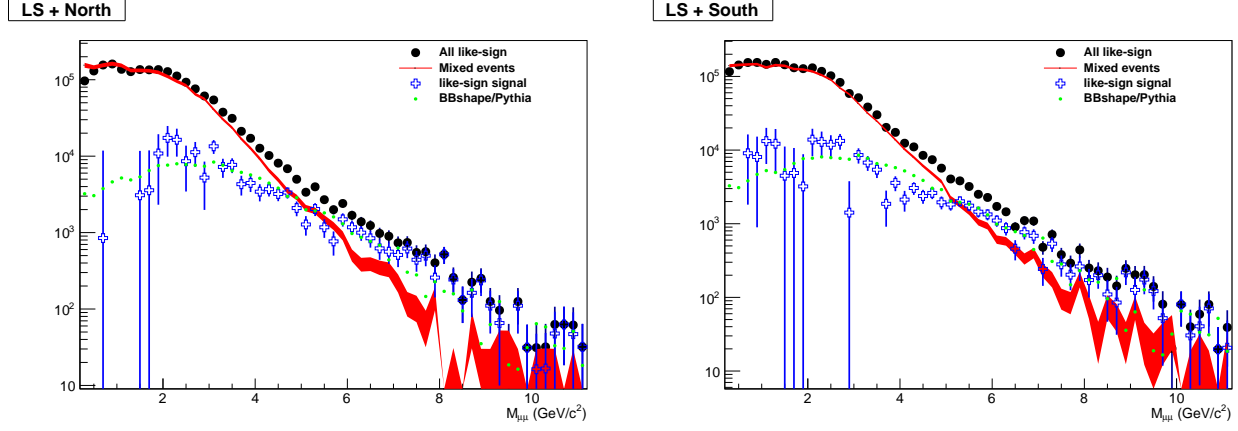


Figure 3.31: The invariant mass spectra for like-sign pairs from the same event (solid black circles), mixed-events (red band), and the difference (empty blue sign) for the north (left) and south (right) arms after applying the normalization factor to the mixed-events spectrum. The figure also shows the $b\bar{b}$ spectrum (green points).

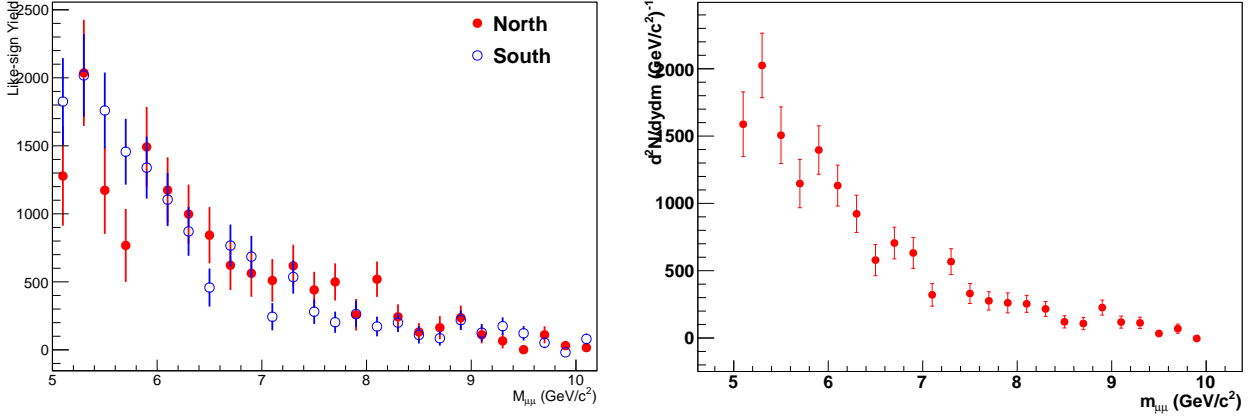


Figure 3.32: Left: Like-sign spectra after subtracting the mixed-events background for the north (solid red circles) and south (empty blue circles) arms. Right: The weighted average of the two arms.

3.2.1.2 $\Delta\phi$ dependence

The data are also sorted as a function of the azimuthal angle ($\Delta\phi$) between the two like-sign tracks. We also used the mixed-events to subtract the combinatorial backgrounds. In this case, the mixed-events spectra were normalized using the normalizing factor extracted from

the previous section (Section 3.2.1.1); $R_{north} = 2.13$ and $R_{south} = 2.16$.

Figure 3.33 shows the like-sign and normalized mixed-events spectra for the north arm in the left panel and the south arm in the right panel in the high mass window. The figure also shows the robustness of the mixed-event normalization method since at small $\Delta\phi$ we expect no $b\bar{b}$ signal and the normalized mixed-event background spectra matches the like-sign spectra below 1.5 radians for both arms as expected.

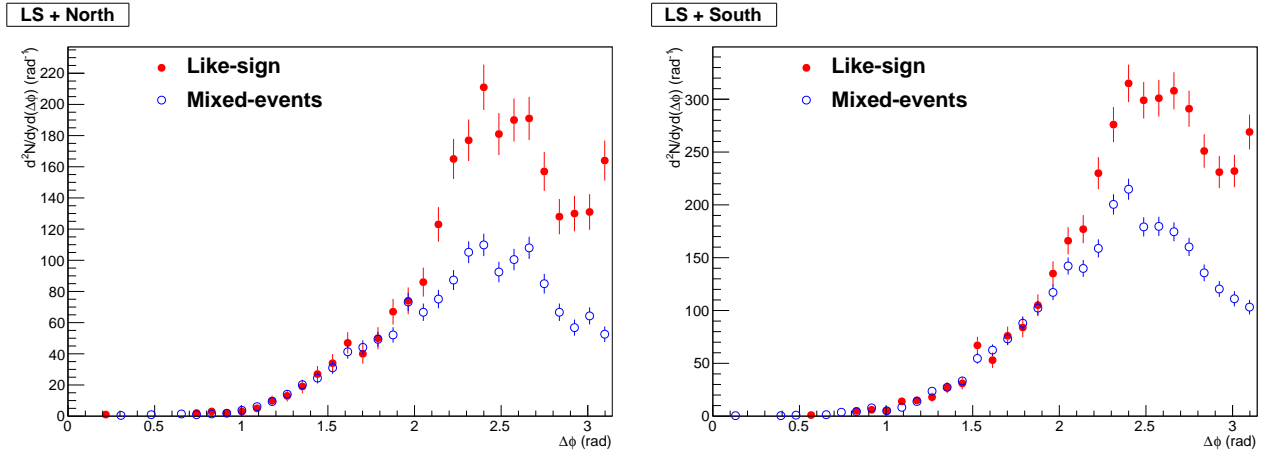


Figure 3.33: Like-sign pairs from the same event (solid red circles) and mixed-events (empty blue circles) for the north (left) and south (right) arms after applying the normalization factor to the mixed-events spectrum.

Figure 3.34 shows the like-sign spectra after subtracting the combinatorial background for the north and south arms in the left panel and the weighted average of the two arms in the right panel. Again, these are $A\epsilon$ corrected distributions so the two arms should match assuming that the hadronic background is either very small and/or the same in both arms.

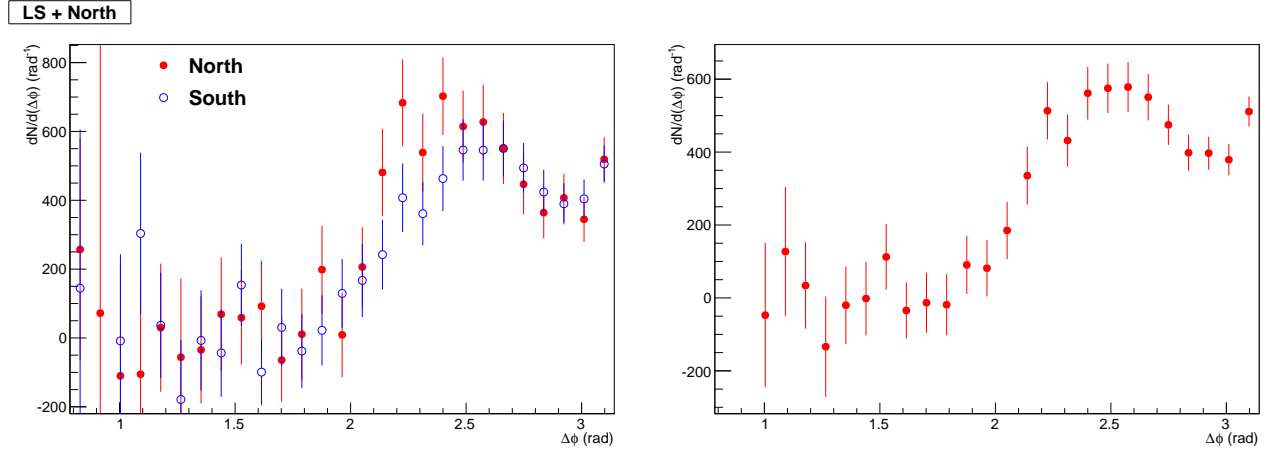


Figure 3.34: Left: Like-sign spectra after subtracting the mixed-events background for the north (solid red circles) and south (empty blue circles) arms. Right: the weighted average of the two arms.

3.2.2 Hadronic Background

The hadronic background is coming from correlated jet contributions. It is estimated by first determining the p_T -dependent survival probability that a hadron will traverse the muon arm detectors and then applying it to PYTHIA generated dihadron pairs to get the yield expected at the back of the muon arm detectors.

The hadrons (pions and kaons with PYTHIA particle codes: 211, 310, 313, 321 and, 323) are generated using PYTHIA Tune A (see Appendix D) at $0.8 < |y| < 3.0$ and within an event vertex sampled from the data (reference run 397293, see Figure 3.25). They are then run through PISA with Run 13 detector settings and reconstructed in a similar fashion to that of the data (see Section 3.1.3).

As a cross check, the generated PYTHIA pion and kaon spectra are compared to fits extracted from UA1 data [39] and the results are shown in Figure 3.36. We see PYTHIA overestimates the cross section in the high p_T region which has a relatively small contribution

to the total cross section. Overall there is a $\approx 30\%$ and $\approx 10\%$ percent error between the two cross sections for the pions and kaons, respectively. However, the total hadronic background contribution to the like-sign dimuon signal is small as will be seen in Section 5.1.1.

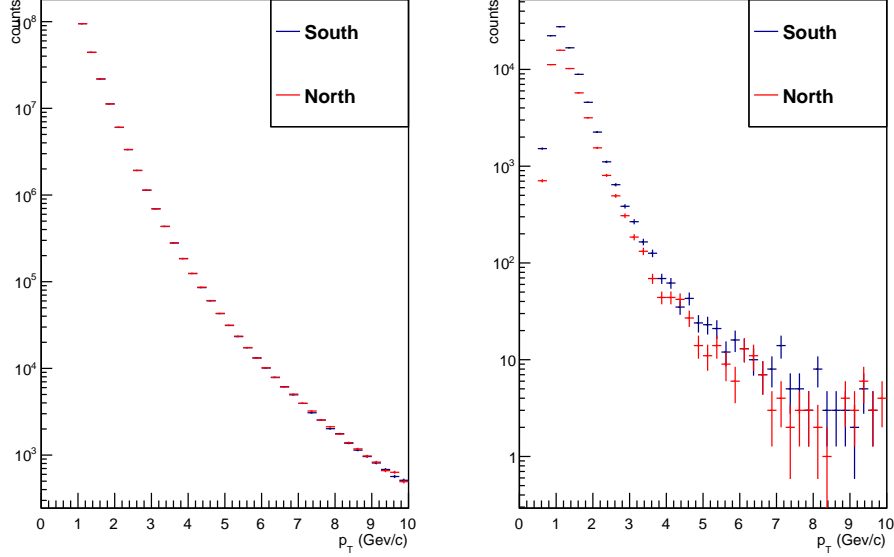


Figure 3.35: Generated single hadrons spectra (left) and reconstructed spectra (right) as a function of p_T for the north (red) and south (blue) arms.

The single hadron survival probability is determined by taking the ratio of reconstructed hadrons over generated hadrons in p_T bins within $1.2 < |y| < 2.2$. The distributions of the generated inclusive hadrons and the same hadrons that pass through the reconstruction process are shown in Figure 3.35. The single hadron survival probabilities are shown in Figures 3.37 and 3.38.

These distributions are then fit with a third order polynomial within the p_T range of 1-10 GeV/c. The fit is used to overcome any statistical fluctuations since the process re-

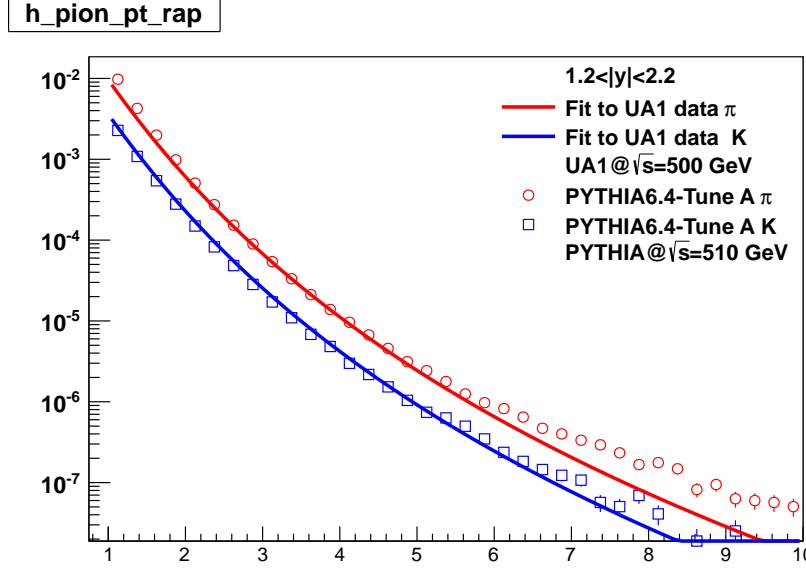


Figure 3.36: Generated hadrons spectra (empty symbols) compared with UA1 data fits (solid lines). The open red circles are for pions while the open blue squares are for kaons.

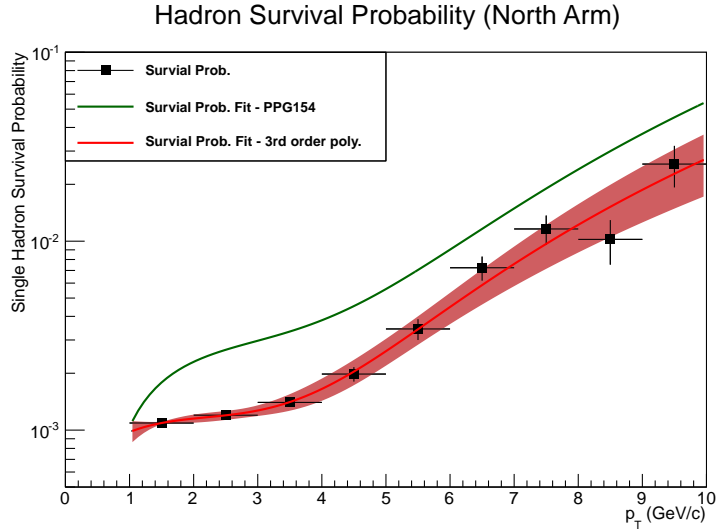


Figure 3.37: Single hadron survival probability for the north arm as a function of p_T . The red line shows a third order polynomial fit while the error band represents a 95% confidence level of the fit. The green line shows the results of a similar fit to Run 9 data.

quires lengthy running times to acquire enough statistics. For comparison, these results are compared to similar fits of Run 9 data [6] and Figures 3.37 and 3.38 show that Run 13 has

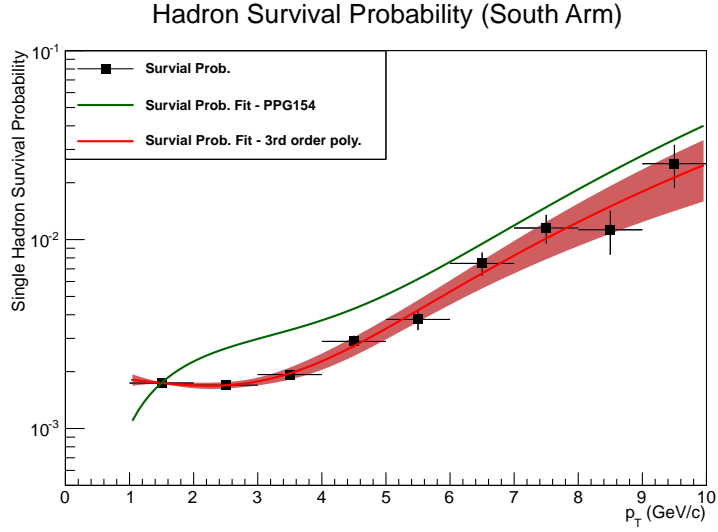


Figure 3.38: Single hadron survival probability for the south arm as a function of p_T . The red line shows a third order polynomial fit while the error band represents a 95% confidence level of the fit. The green line shows the results of a similar fit to Run 9 data.

a lower survival probability than was observed in Run 9 due to the added steel absorbers, consistent with our expectations.

3.2.2.1 Mass dependence

After estimating the survival probability, PYTHIA simulation in minimum bias mode was used to extract the hadronic background. The resulting hadrons from PYTHIA are paired in a similar manner to that used in the data; forming like-sign pairs and mixed-event pairs. During the pairing process, each hadron is weighted with the survival probability based on its p_T value. After applying the weights, the mixed-events spectrum is normalized to the like-sign pairs spectrum in the low mass region, using the first iteration in normalizing the combinatorial background (see Section 3.2.1). The mixed-events spectrum is then subtracted from the like-sign spectrum.

Figure 3.39 shows the like-sign and normalized mixed-events spectra in the panels on the left and the like-sign spectra after subtracting mixed-events in the panels on the right. The upper panels show the results from the south arm while the lower panels show the results from the north arm. Figure 3.40 shows the hadronic background for each of the arms fitted with an exponential; $e^{(p_0+p_1*mass)}$.

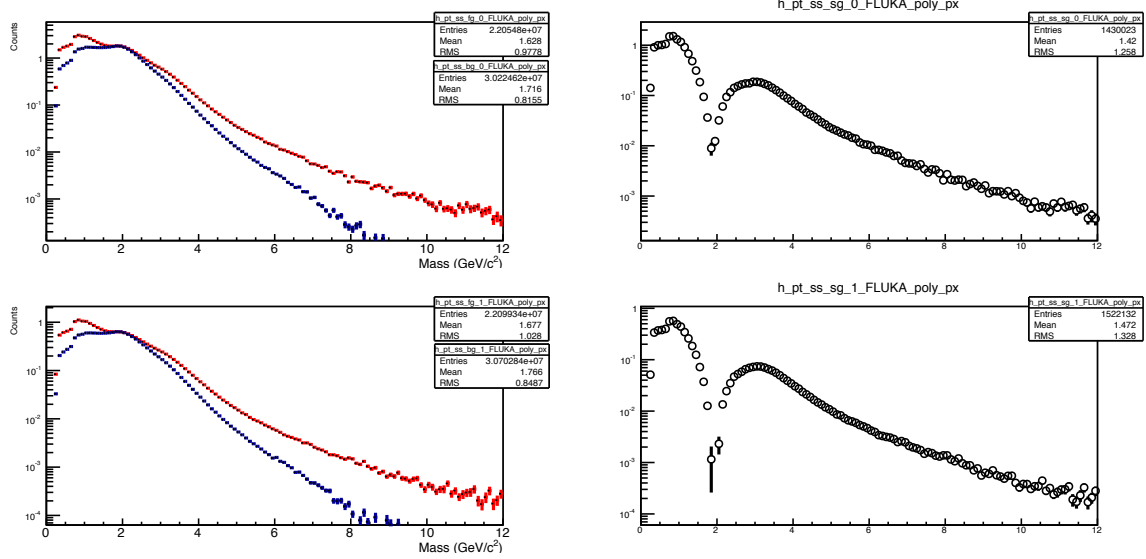


Figure 3.39: Left: Dihadron mass spectra of the foreground pairs (left) and the normalized mixed-events pairs (blue). Right: correlated dihadron pairs. The top row is for the south arm while the bottom row is for the north arm.

3.2.2.2 $\Delta\phi$ dependence

The hadronic background was also sorted in $\Delta\phi$ between the two hadrons and the normalization factors for the south and north arms from the mass case were used here. The subtracted spectra for both arms as well as the weighted average are shown in the left panel of Figure 3.41 while the right panel shows the weighted average fitted with an exponential

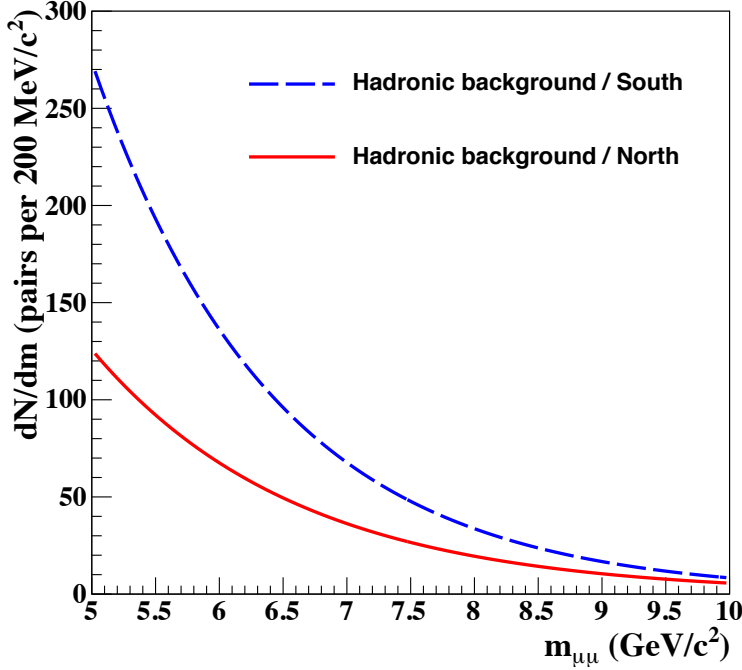


Figure 3.40: Fitted hadronic background in the north arm (solid red line) and the south arm (dashed blue line) as a function of dihadron mass.

to the power of a third order polynomial; $e^{(p_0 + p_1 * \text{mass} + p_2 * \text{mass}^2 + p_3 * \text{mass}^3)}$.

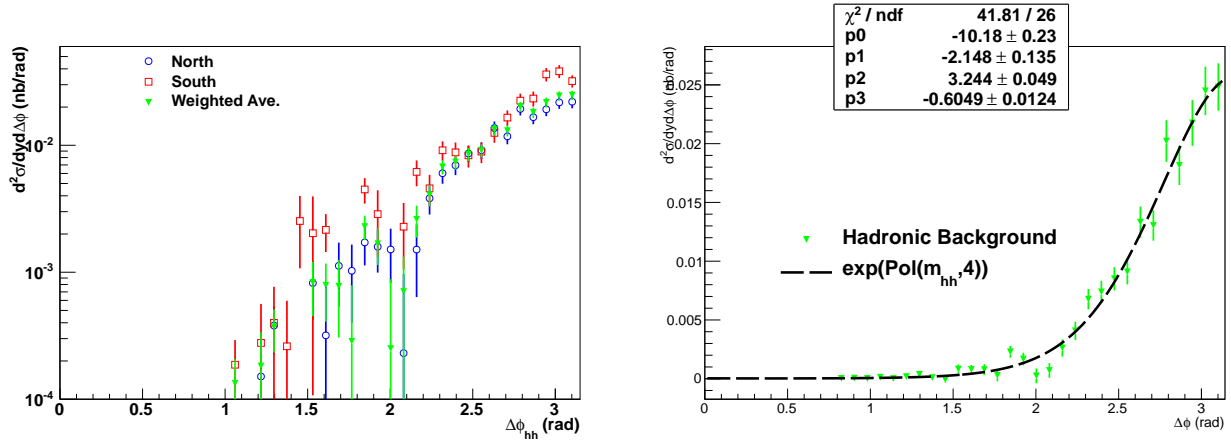


Figure 3.41: Left: Hadronic background is the north arm (empty blue circles), south arm (empty red squares) and their weighted average as a function of the dihadron mass. Right: the weighted average fitted with an exponential.

SYSTEMATIC UNCERTAINTIES

This chapter explains the systematic uncertainties that are considered with this measurement. There are several types which will be explained below and are standardized by the International Organization for Standardization [40]. They can be divided into three categories based on their effect each has on the measured result. All are reported as standard deviations.

- Type A - these are uncorrelated from point to point uncertainties which allow the data points to move independently with respect to one another and are added in quadrature with statistical uncertainties
- Type B - these are correlated from point to point, non statistical uncertainties which move the data points coherently within the quoted range
- Type C - these uncertainties are global to the measurement, scaling the value in either direction and are also point to point correlated

Table 4.1 includes a summary of all the systematics uncertainties. No systematic uncertainty of Type-A is associated with this measurement.

4.1 Acceptance and Reconstruction Efficiency

The systematics uncertainties associated with $A\epsilon$ are determined using a J/ψ PYTHIA embedding simulation. The J/ψ signal is used because it is a resonance particle in close

Table 4.1: Summary of all systematic uncertainties

Source	Value	Type
Signal Extraction	$\pm 3.3\%$	B
MuID Efficiency	$\pm 4.0\%$	B
MuTr Efficiency	$\pm 2.0\%$	B
Acceptance \times Efficiency	$\pm 9.3\%$	B
Jet Simulation	$\pm 4.3\%$	B
Fit Function	$\pm 4.3\%$	B
$\alpha(m)$	$\pm 1.9\%$	B
β	$\pm 4.5\%$	B
Total	$\pm 13.3\%$	B
BBC Efficiency	$\pm 10.0\%$	C
Simulation Input	$\pm 4.3\%$	C
Model dependence	$\pm 25.7\%$	C
Total	$\pm 27.9\%$	C

proximity with the open bottom signal region. While we try to use the most realistic description of the detector (geometry, HV channels on or off, and run by run variations, etc.) in simulations, the results are never perfect. The PYTHIA simulation settings are listed in Appendix F. The vertex distribution was based on that of Run 13 BBC_z vertex (see Figure 3.25). The generated events are then run through PISA (Run-13 510 GeV setup) and real $p+p$ data are embedded into them. The reference run used for this simulation is run number 397293.

For consistency, the same code and same quality cuts used on the data were used for the

simulation. The simulation also uses a trigger emulator tool. The efficiency of the trigger emulator tool was studied by applying the trigger emulator to data and comparing it with data using the dimuon live trigger. The spectrum can be seen in Figure 4.1. However, when looking at the trigger emulator efficiencies compared to real data efficiencies, they are consistent within 5%. The results are a difference of $< 0.5\%$ in the north arm and $< 1.5\%$ in the south arm, which are assigned as a systematic uncertainties.

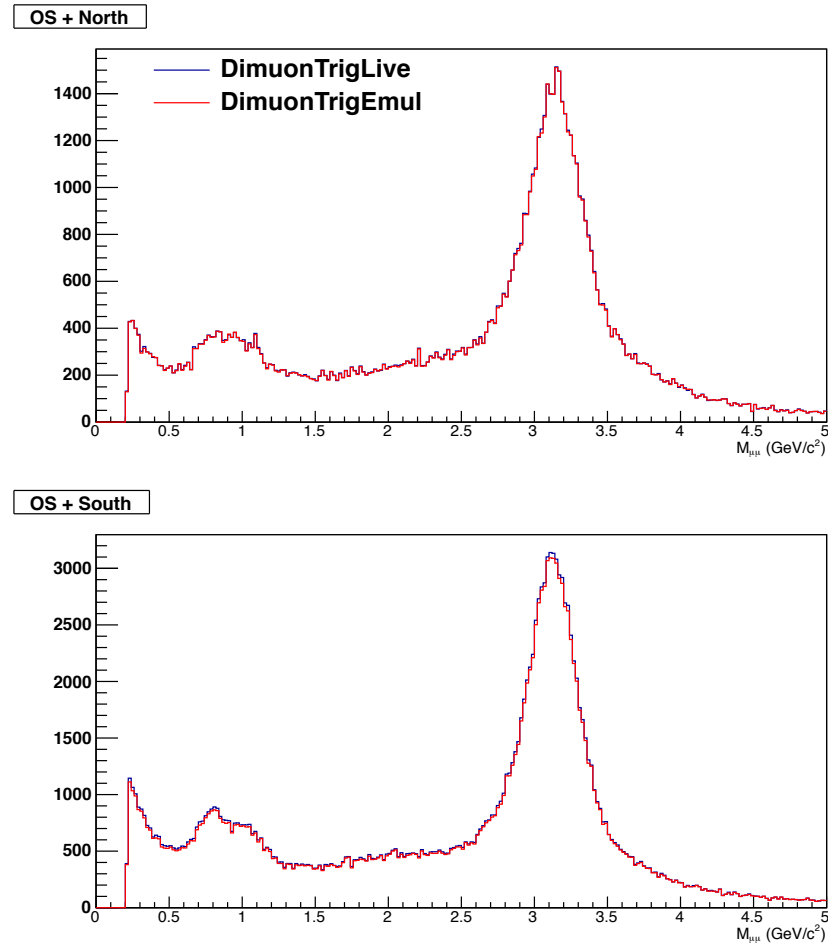


Figure 4.1: Data with both the trigger emulator and the dimuon live trigger applied.

In the J/ψ $A\epsilon$ calculations for Run 13, the difference between PYTHIA and the dimuon generator results was taken as a systematic uncertainty on the input p_T distribution. The input p_T used for the dimuon generator is from data. See Figure 4.2 for a comparison between the PYTHIA and dimuon generator $A\epsilon$ output. A systematic of $< 4.0\%$ was assigned due to these differences.

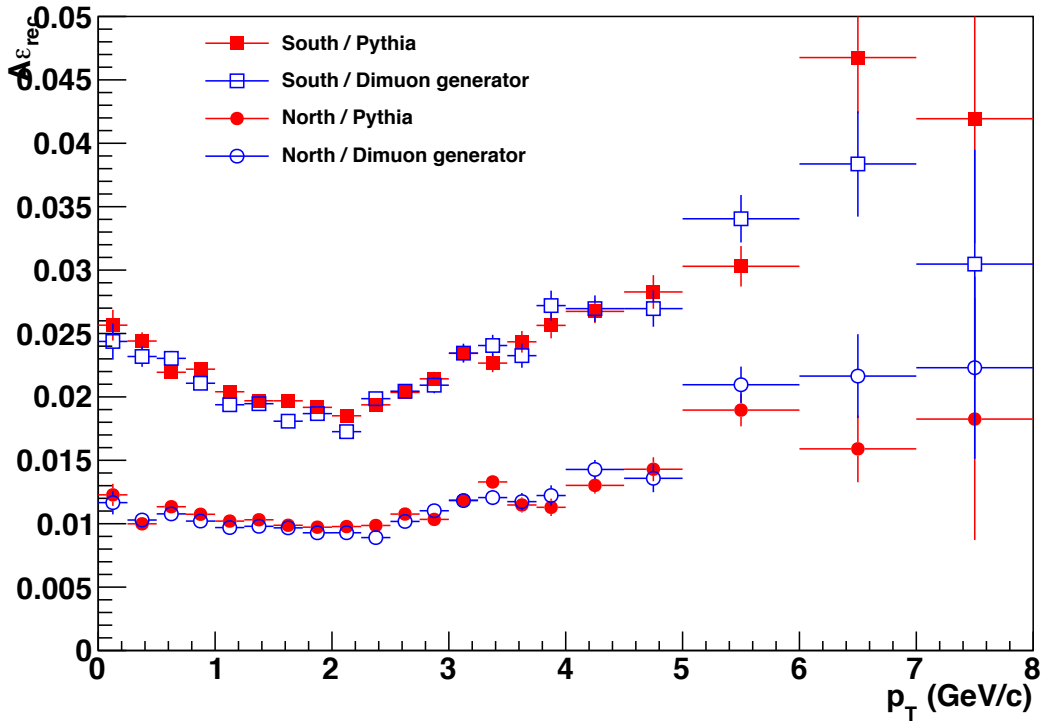


Figure 4.2: Comparison of p_T dependent J/ψ $A\epsilon$ between PYTHIA simulation and dimuon generator output.

An additional systematic is applied based on the azimuthal angles differences between data and simulation. This is evaluated to understand the uncertainty in $A\epsilon$ for single particles in a typical octant of the MuTr detector. The single track azimuthal distributions can be seen in Figure 4.3. There is no obvious selection in which octant to use as a reference point

so we calculate a RMS for each octant in reference to the other seven octants and take a weighted average of the RMS values as the systematic. We calculate a normalization factor ($R=N_{DATA}/N_{MC}$), where N_{DATA} and N_{MC} are the yields from data and simulation, respectively.

$$RMS_i = \sqrt{\frac{1}{N-1} \sum_{j \neq i}^N \left(\frac{N_{MC}^j R_i - N_{DATA}^j}{N_{MC}^j R_i} \right)^2} \quad (4.1)$$

That resulted in a 4.9% for the north arm and 6.0% for the south arm. The total systematic uncertainty associated with $A\epsilon$ is $\sim 9.3\%$. These errors are point-to-point correlated (Type-B).

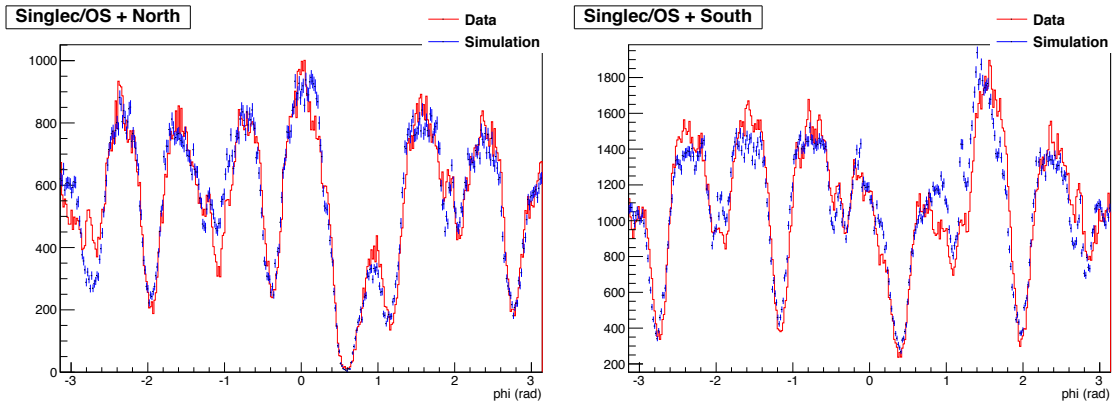


Figure 4.3: Comparison of single muon candidate tracks azimuthal distributions from J/ψ . The structure of the distributions are due to the eight octants of the MuTr detector.

4.2 Muon Arm Detector Efficiencies

Based on previous Muon Arm analyses, a $\pm 4\%$ uncertainty from MuID tube efficiency and a $\pm 2\%$ from MuTr overall efficiency were assigned. This systematic uncertainty was averaged over arms. This systematic uncertainty applies to the p_T dependent results since they were averaged over arms. These errors are point-to-point correlated (Type-B).

4.3 Signal Extraction

The error associated with the normalization factor of the mixed-events, discussed in detail in Section 3.2, was studied by comparing the resulting yields after varying the four different normalization windows $[0.5,2.6]$, $[0.5,3.6]$, $[2.6,3.6]$, and $[1.6,4.2]$ used in the analysis. The process involved using each of the windows separately and two windows at a time as well as shifting the range by a 0.5 and 1 GeV/c^2 . These windows include: $\{[0.5,2.6]\}$, $\{[0.5,3.6]\}$, $\{[2.6,3.6]\}$, $\{[1.6,4.2]\}$, $\{[0.5,2.6], [2.6,3.6]\}$, $\{[0.5,3.6], [1.6,4.2]\}$, $\{[1.0,3.1], [1.0,4.1], [3.1,4.1]\}$, $\{[2.1,4.7]\}$, $\{[0.0,2.1], [0.0,3.1], [2.1,3.1], [1.1,3.7]\}$, and $\{[1.5,3.6], [1.5,4.6], [3.6,4.6], [2.6,5.2]\}$. Then, we take the RMS value between the yields and extracted yield with the default windows. The left panel of Figure 4.4 shows the extracted signal with each of the windows selections. To get a better look at how these different windows affected the outcome the right panel shows fits of the extracted signal spectra.

This results in an uncertainty of 1.7% in the north arm and 2.9% in the south arm. Since we present the cross section as the sum of both arms, the quadrature sum is 3.3%. This is considered as a Type-B point-to-point correlated uncertainties which allows the data points

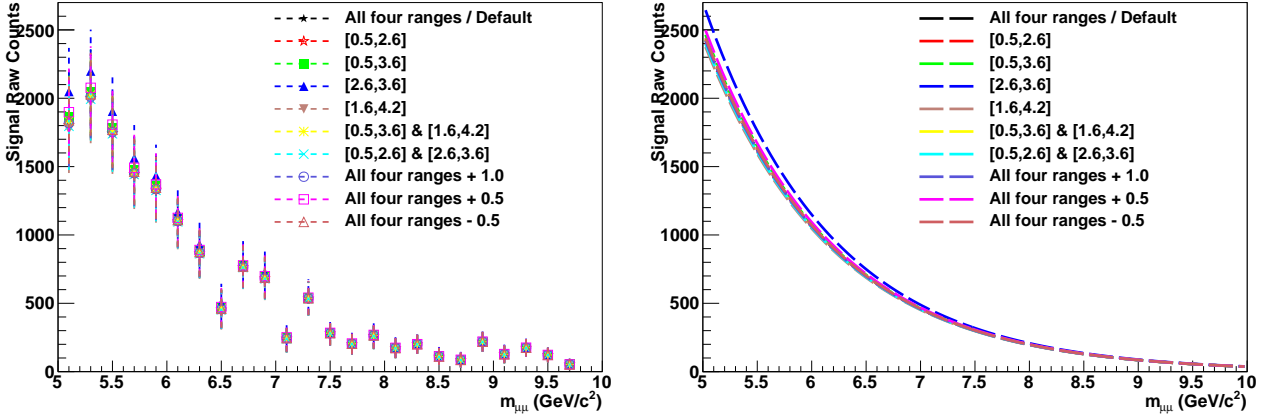


Figure 4.4: Like-sign pairs spectra after mixed-events subtraction using different normalization windows (left) and their exponential fits (right).

to move coherently within the quoted range.

4.4 BBC Event Rate

As mentioned in Section 2.2.1, the possibility of a second collision event occurring in a triggered event must be considered. This takes place due to the large beam luminosity provided by the CAD. When this happens, two collision vertexes are included in the triggered event. This allows for the possibility of the event vertex to be determined by the BBC detector as one of the two event vertices or a vertex position some where between the two collision points. The occurrence of multiple collisions increases the BBC detector multiplicity and artificially smears the dimuon invariant mass distribution because some of the reconstructed dimuon tracks are pointing back to an incorrect event vertex.

As a cross check, we looked at like-sign dimuon spectra for the north and south arms as a function of the BBC event rate. The BBC event rate was divided into two data sets for

the runs used in this analysis, see Figure 4.5. This choice was made to simply divide data into two samples with a comparable number of runs.

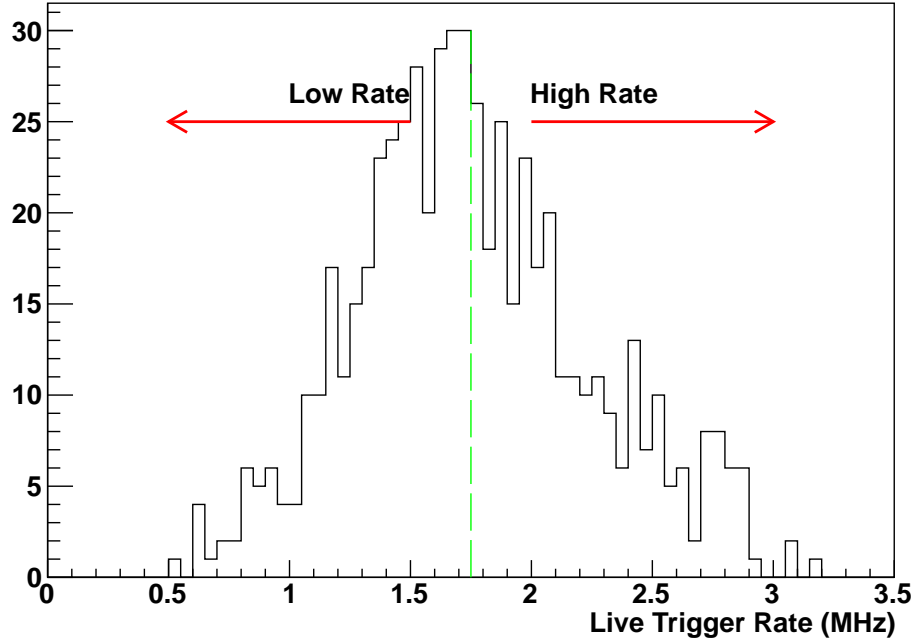


Figure 4.5: BBC rate distribution of the runs used in the analysis. The dashed green line shows where the runs are divided into low and high rate.

Figure 4.6 shows the dimuon mass spectra for the high and low BBC rate for the north arm and south arm (empty blue circles). Each spectra is normalized by its integration. It is quite clear from this simple example that there is no dependence on rate when it comes to mass distribution.

Figures 4.7 and 4.8 shows the ratio of high to low BBC rate mass spectra fitted by zeroth order polynomial and a first order polynomial, respectively. The χ^2 values in the case of zeroth order fit indicates that there is a negligible effect, but considering the σ values in each

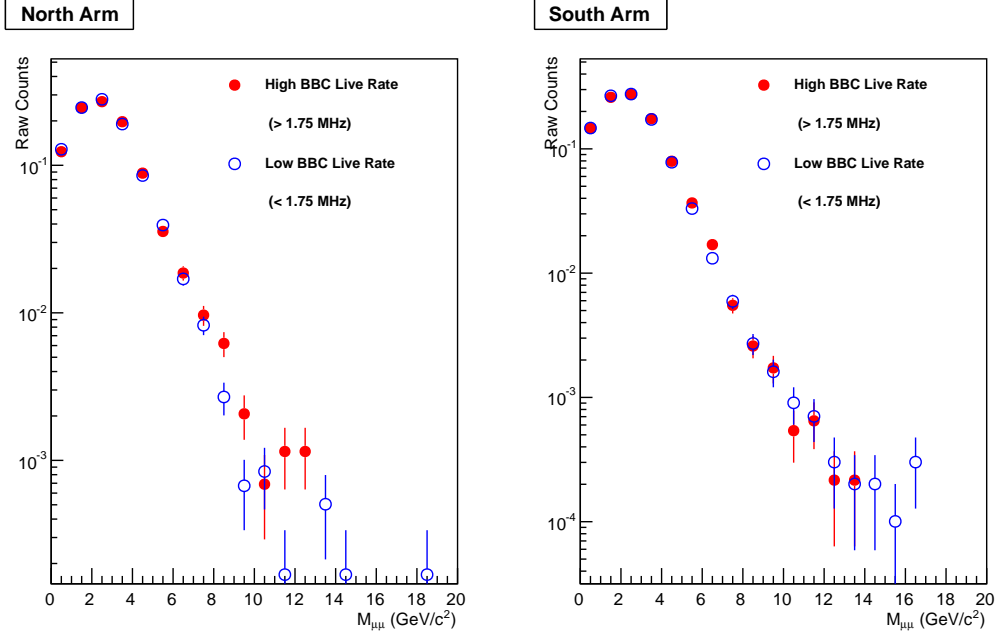


Figure 4.6: Dimuon mass spectra for high (solid red circles) and low (empty blue circles) BBC rate for the north arm (left) and south arm (right).

arm we could assign a value of $< 2\%$. However, to be more conservative in this case the first order fit is used to extract a systematic error according to the following:

$$\delta = \frac{R(m_H) - R(m_L)}{2} \quad (4.2)$$

where $R(m_H)$ and $R(m_L)$ are the rate values at the high and low mass values. This produces an effect of $< 3\%$ which is used as a systematic error due to the rate dependence over the studied mass range.

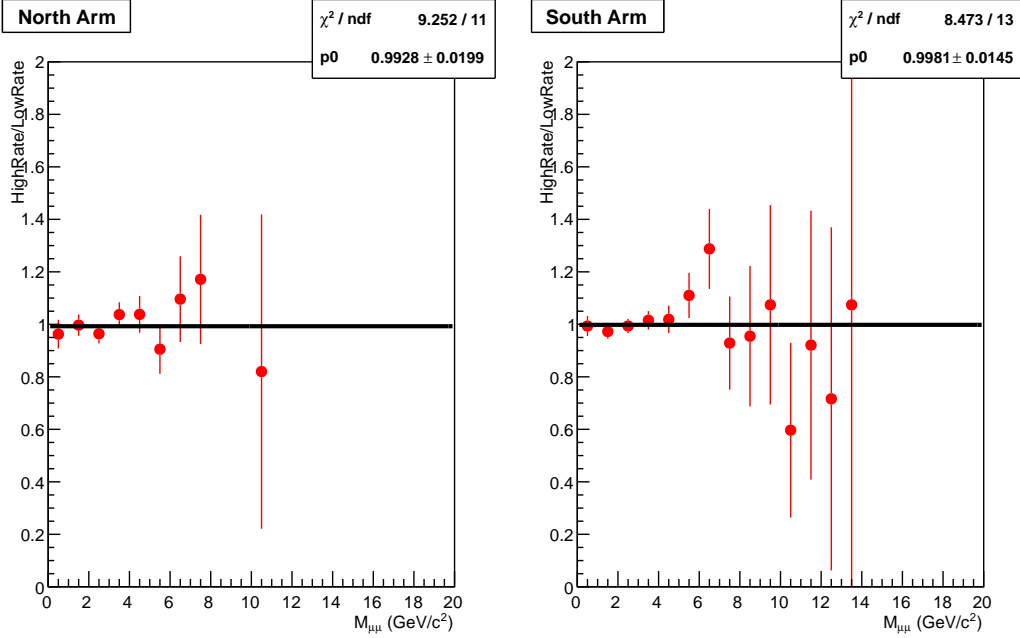


Figure 4.7: The ratio of high to low BBC rate mass spectra in the north arm (left) and south arm (right) fitted by a zeroth order polynomial.

4.5 Hadronic Background

The uncertainty associated with the hadron simulation is estimated by using two hadron interaction packages for GEANT: GHEISHA and FLUKA. For each package a hadron survival probability was determined and two fits were applied to the distributions (see Figure 4.9). The two fits (exponential with the form $e^{p_0 + p_1 * mass + p_2 * mass^2 + p_3 * mass^3}$ and a 3rd degree polynomial) were considered but the effect on the final dihadron cross section was negligible and no systematic uncertainty was applied. The different survival probabilities were then used to make weighted dihadron pairs from which the correlated dihadrons are determined. Figure 4.13 shows dimuon mass distributions of the correlated hadrons weighted with the hadron survival probabilities using FLUKA and GEISHA. The average of FLUKA and GEISHA was

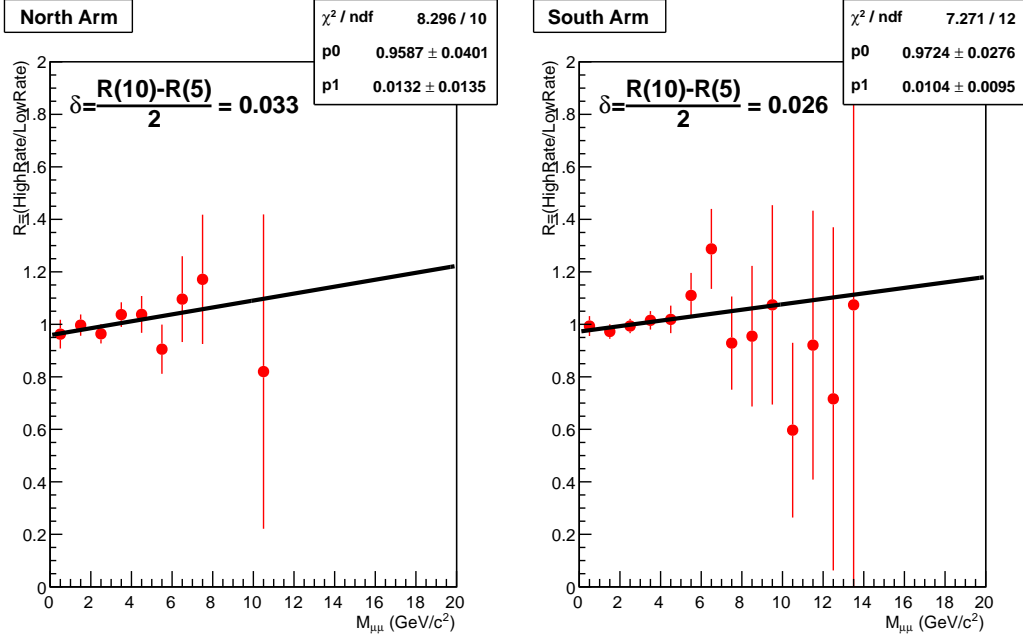


Figure 4.8: The ratio of high to low BBC rate mass spectra in the north arm (left) and south arm (right) fitted by a zeroth order polynomial.

used as the hadronic background while the difference between the two was used as a systematic uncertainty. Differences of up to 22% and 30% between FLUKA and GEISHA were observed in the north and south arms, respectively. However, since the hadronic background amounted to less than 10% of the signal the systematic uncertainty from the hadronic background estimates is an order of magnitude less. Figure 4.13 shows the mass dependent systematic uncertainties associated with the cross section. Differences between the slopes of the two packages contribute a Type-B uncertainty to the cross section of $\pm 3.8\%$ in the south arm and $\pm 2.1\%$ in the north arm. The combined systematic is $\pm 4.3\%$.

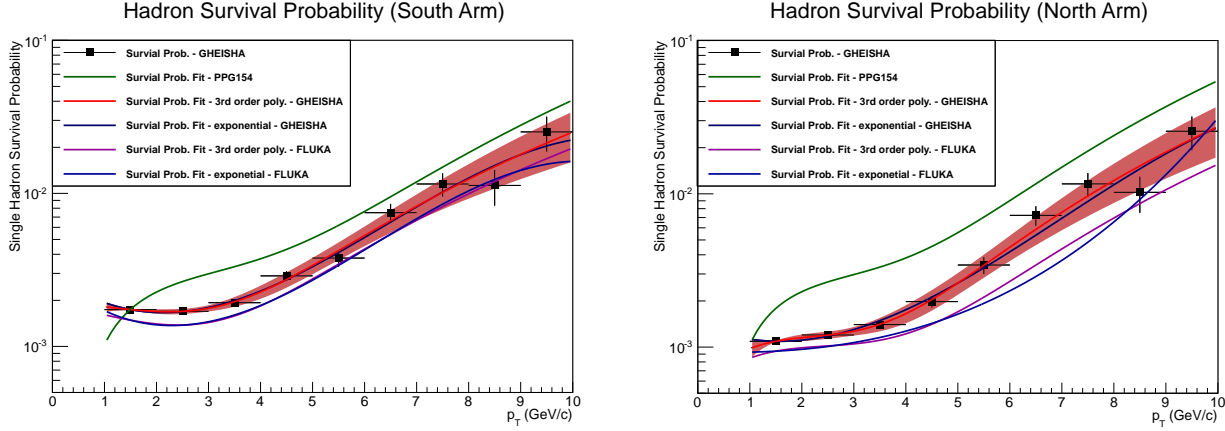


Figure 4.9: Hadron survival probabilities. The points are the probability as determined using the GHEISHA package with a fit (red curve, with statistical error band). The remaining curves are determined with the combination of interaction package and fit function. The green curve is the survival probability as determined with the Run 9 simulation set up. On the left hand is the probability as determined for the south arm and the right is for the north arm.

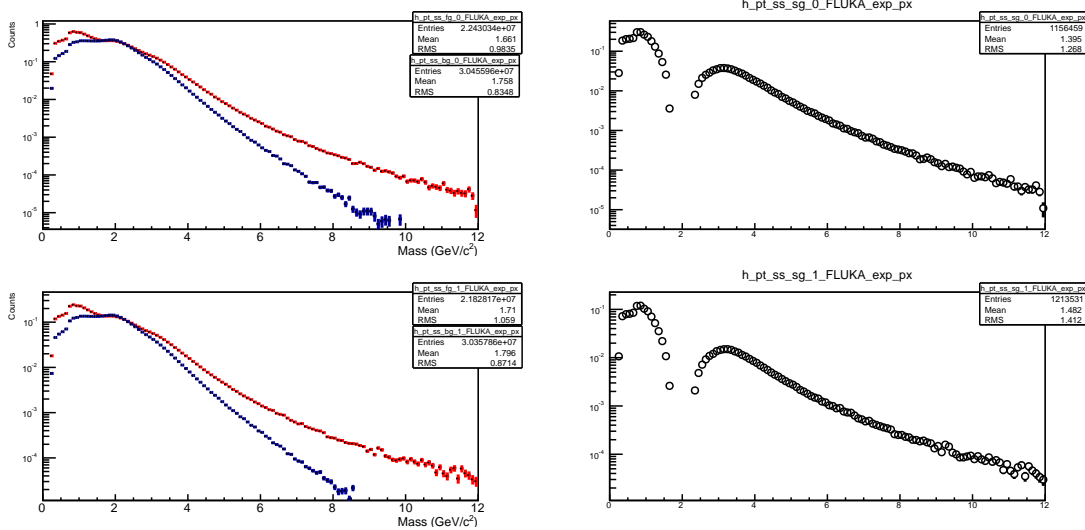


Figure 4.10: Weighted dihadron pairs using the FLUKA hadronic interaction package and an exponential fit to the single hadron survival probability. The left is the foreground pairs in red and the mixed-event background pairs in blue. The right is the correlated pairs. The top is for the south and the bottom for the north arm.

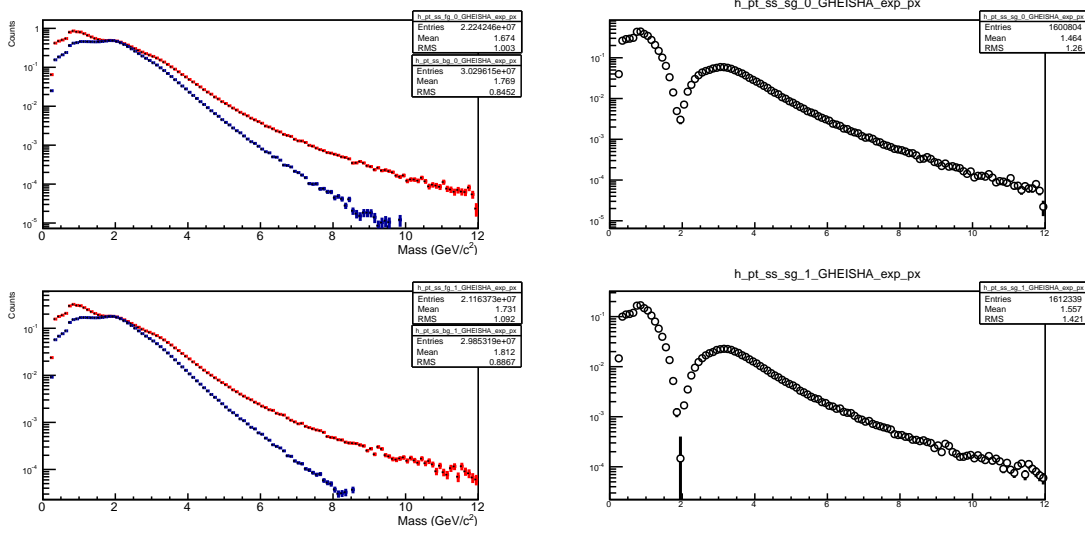


Figure 4.11: Weighted dihadron pairs using the GHEISHA hadronic interaction package and an polynomial fit to the single hadron survival probability. The left is the foreground pairs in red and the mixed-event background pairs in blue. The right is the correlated pairs. The top is for the south and the bottom for the north arm.

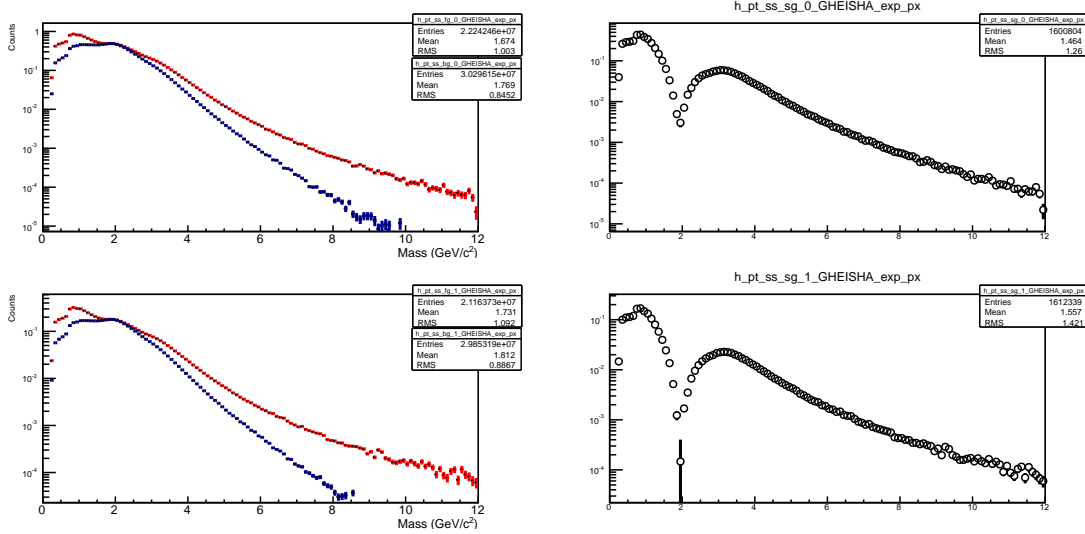


Figure 4.12: Weighted dihadron pairs using the GHEISHA hadronic interaction package and an exponential fit to the single hadron survival probability. The left is the foreground pairs in red and the mixed-event background pairs in blue. The right is the correlated pairs. The top is for the south and the bottom for the north arm.

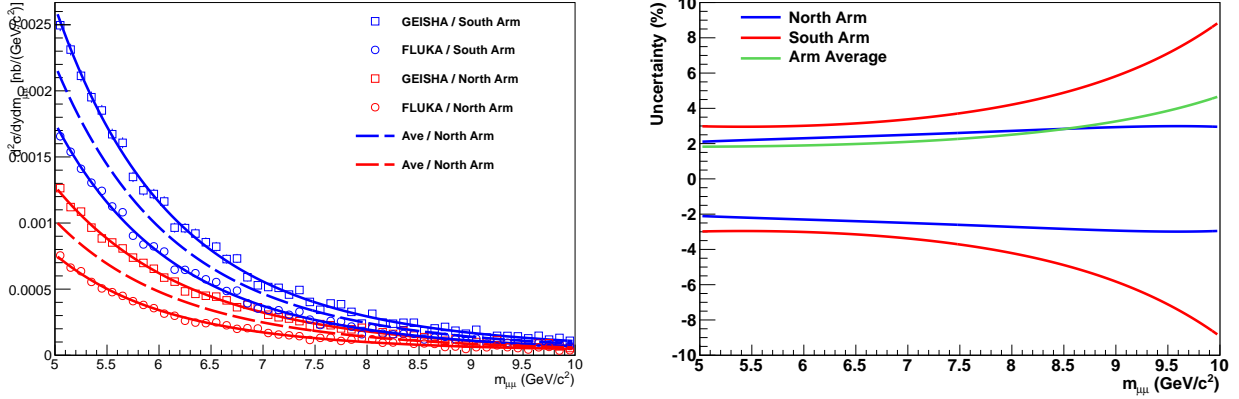


Figure 4.13: Left: Fits to different correlated dihadrons as determined through single particle survival using different hadronic interaction packages: FLUKA and GHEISHA. Right: The mass dependent systematic uncertainties associated with the cross section.

4.6 Fit Function

The line shape of the like-sign dimuons from open bottom decay and jet background are not precisely known. Therefore, to assign an error on the cross section associated with the line shape, we recalculate the fits after varying the slope of each component by 10%. In addition, we use several other fit functions including an exponential with different form $p_0 * e^{(p1 * mass_{\mu\mu})}$ and polynomials of the second, third and fourth orders. Figure 4.14 shows these function after fitting compared with default one. This results in a Type-B uncertainty of 4.3%. These errors are point-to-point correlated (Type-B).

4.7 Simulation Inputs: $\alpha(m)$ and β

These simulation input parameters are used to extract and extrapolate the $b\bar{b}$ signal. See Section 5.1.1.

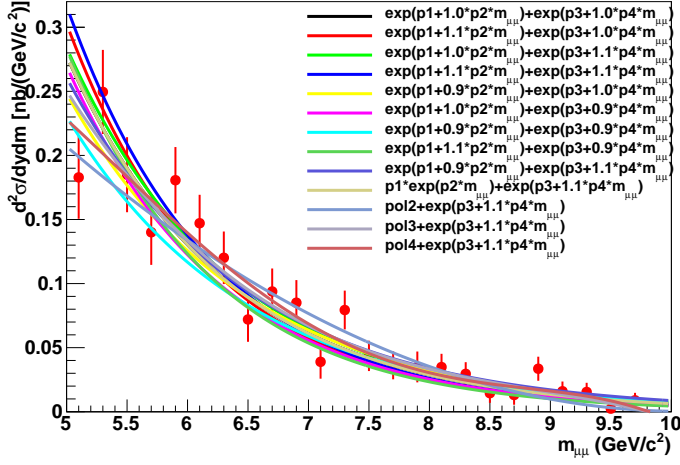


Figure 4.14: Different fits to the like-sign dimuons from open bottom decay.

4.7.1 $\alpha(m)$

$\alpha(m)$ is defined as the ratio of like-sign dimuon pairs from primary-primary decays of B mesons that oscillate to the total yield of like-sign dimuon pairs from B mesons which includes primary-primary and primary-secondary decay processes. It is a mass dependent quality and a fit is used in the analysis. The three parameters in the second order polynomial function that fits the ratio of like-sign from oscillation to all like-sign dimuons are highly correlated. We therefore use the covariance matrix to calculate the uncertainty on the fit. When using the covariance matrix the uncertainty must be calculated for each mass bin. The uncertainty in each bin is then weighted by the percent of counts from data in each mass bin. This results in a Type-B uncertainty of $\pm 1.9\%$. This uncertainty is due to the fit parameters.

4.7.2 β

β is defined as the ratio of like-sign dimuon pairs from primary-primary decays of B mesons that oscillate to the total yield of all-sign dimuon pairs from B mesons. β is determined using PYTHIA 6, PYTHIA 8 and MC@NLO (Using the default $b\bar{b}$ settings and CTEQ5M PDF) simulations by fitting the mass distribution (See Figure 4.15) with a zeroth order polynomial and listed in Table 4.2. The distributions for PYTHIA 8 and MC@NLO are shown in Figure 4.15. The error of β is the standard deviation of the three model calculations which represents the model-dependent uncertainty. This is a Type-B uncertainty of $\pm 4.5\%$.

Table 4.2: Values of β as found using PYTHIA 6, PYTHIA 8 and MC@NLO

Simulation	β
PYTHIA 6 (CTEQ6LL)	0.21
PYTHIA 8 (CTEQ6LL)	0.22
MC@NLO (CTEQ5M)	0.23
RMS Value	0.22 ± 0.01

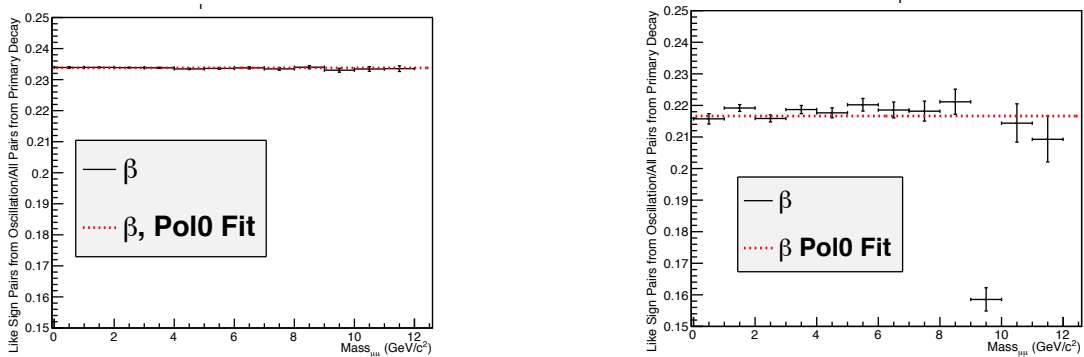


Figure 4.15: β shown as a function of mass in the MC@NLO (left) and PYTHIA8 (right).

4.8 BBC Efficiency

An uncertainty of $\pm 10\%$ was assigned for the overall BBC efficiency. This is a global (Type-C) uncertainty that allows the data points to move together by a common multiplicative factor.

4.9 Scale Factor

The scale factor is used to scale the measured cross section up to a total cross section and is further discussed in Section 5.2. The model dependent and PDF variation uncertainties of the scale factor are determined by comparing simulated events generated with PYTHIA 6 (CTEQ6LL) and PYTHIA 8 (CTEQ6LL) and [41,42] to those generated from PS PYTHIA 6 (CTEQ5M1), PYTHIA 6 Tune A (CTEQ5L) and MC@NLO (CTEQ5M). In this case, all four event generators are using CTEQ PDFs. The difference in the scale factor due to the different models and PDFs are considered a global Type-C uncertainty and amounts to $\pm 25.7\%$.

Table 4.3: Values of the scale factor as found using PYTHIA 6, PYTHIA 8 and MC@NLO

Simulation	Scale Factor
PYTHIA 6 (CTEQ6LL)	0.002067
PYTHIA 8 (CTEQ6LL)	0.002096
MC@NLO (CTEQ5M)	0.001126
PYTHIA 6 (CTEQ5M1)	0.002546
PYTHIA 6 (CTEQ5L)	0.001506
RMS Value	0.001933 \pm 0.000501

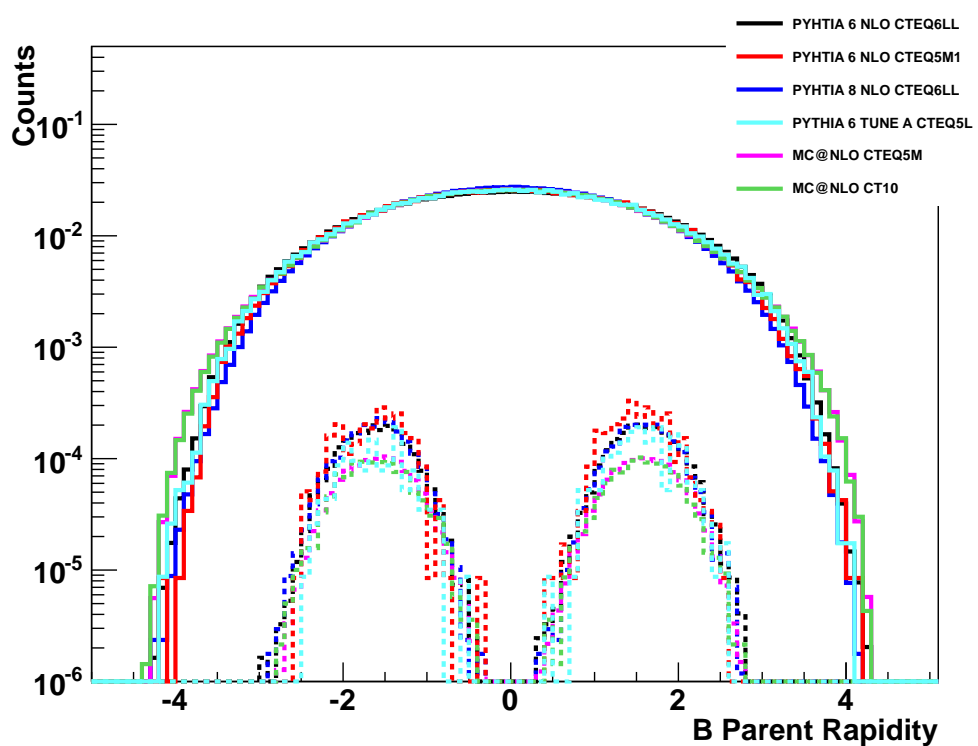


Figure 4.16: Distributions used to determine the scale factor.

5

RESULTS

After extracting the like-sign yields (see Section 3.2), the differential yields and differential cross sections are calculated as a function of mass and azimuthal angle ($\Delta\phi$) according to the following relations:

$$\frac{d^2N}{dydm} = \frac{N_{l.s.}}{\Delta y \Delta m} \frac{1}{A\varepsilon(\Delta y \Delta m)} \frac{1}{N_{MB}^{BBC}} \frac{\varepsilon_{MB}^{BBC}}{\varepsilon^{BBC}} \quad (5.1)$$

$$\frac{d^2\sigma}{dydm} = \frac{d^2N}{dydm} \sigma_{total} \quad (5.2)$$

$$\sigma_{total} = \sigma_{BBC} / \varepsilon_{MB}^{BBC} \quad (5.3)$$

where σ_{BBC} is the BBC cross section, $32.5 \pm 3.2\%$ mb, which is determined using the Van der Meer scan technique [43]. ε_{MB}^{BBC} is the MB efficiency, 0.53 ± 0.02 , and ε^{BBC} is the efficiency of MB trigger for events containing hard scattering, 0.91 ± 0.04 . It is the ratio of high p_T photon triggered events, as triggered by the BBC, to those not triggered by the BBC. N_{MB}^{BBC} is the number of MB events, and $N_{l.s.}$ is the yield of like-sign pairs. $A\varepsilon$ is the detector's acceptance and reconstruction efficiency (see Section 3.1.3). It was also observed that the dimuon trigger has a much lower livetime, $\sim 72.6\%$, than that of the BBCLL1 trigger at $\sim 91.6\%$ and the $b\bar{b}$ yield is scaled by the factor $0.916/0.726$ to account for this.

5.1 Differential Cross Section

The yields extracted in Section 3.2 still include correlated hadronic background pairs. The hadronic background is extracted as a differential cross sections from simulation and is subtracted from the like-sign differential cross section.

5.1.1 Mass dependence

The dimuon mass dependent differential cross section is calculated according to Equations 5.1 and 5.2 using the yield in Figure 3.32 and the result is shown in the left panel of Figure 5.1. The differential cross section at this point still includes the hadronic background so the right panel of Figure 5.1 shows the dimuon mass dependent differential cross section after subtraction of the hadronic background. Since the two arms are very consistent (See the right panel of Figure 5.1) and to reduce statistical fluctuations the weighted average between the two arms is used and is shown in Figure 5.2.

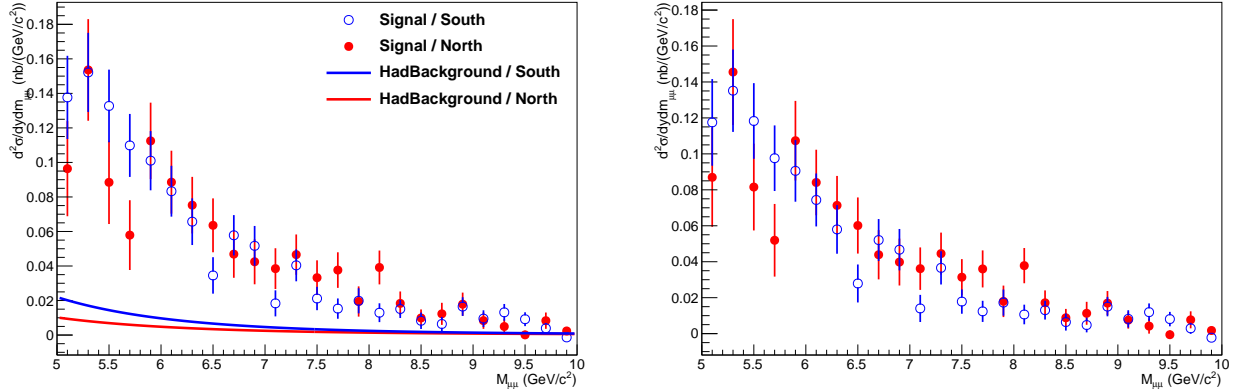


Figure 5.1: Left: The dimuon mass dependent differential cross section before subtracting the hadronic background. Right: The dimuon mass dependent differential cross section after subtracting the hadronic background. The open blue circles are for the south arm and the closed red circles are for the north arm.

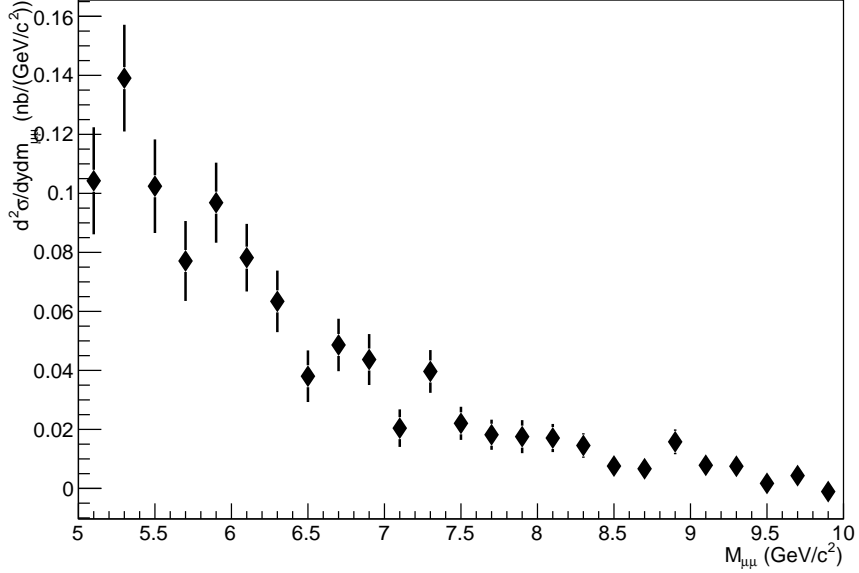


Figure 5.2: The weighted average of the differential cross section from the north and south arms as a function of dimuon mass.

The differential cross section of like sign dimuons, shown in Figure 5.1, results from semi-leptonic decays of open bottom mesons and to obtain the differential cross section of all bottom pairs we do the following two steps:

- multiplying by the ratio of like-sign dimuons at mass m from primary-primary decays, due to B^0 oscillation, to like-sign muon pairs resulting from primary-primary or a mixture of primary-secondary decays, $\alpha(m)$, and it is defined as:

$$\alpha(m) = \frac{b\bar{b} \rightarrow B\bar{B} \rightarrow \mu^\pm\mu^\pm(\text{osc})}{b\bar{b} \rightarrow B\bar{B} \rightarrow \mu^\pm\mu^\pm} \quad (5.4)$$

- dividing by the ratio of primary-primary like-sign dimuons due to B^0 oscillation to all B meson pairs that decay into primary-primary dimuons with all possible muon charge

pairs (+ +, - - and + -), that is called β . It is defined as:

$$\beta = \frac{b\bar{b} \rightarrow B\bar{B} \rightarrow \mu^\pm \mu^\pm(\text{osc})}{b\bar{b} \rightarrow B\bar{B} \rightarrow \mu\mu} \quad (5.5)$$

$\alpha(m)$ is obtained using open bottom events from three model calculations: MC@NLO (CTEQ5M), PS PYTHIA 6 (CTEQ6LL) and PYTHIA 8 (CTEQ6LL) as shown in Figure 5.3. The red line is a fit with a second-order polynomial with χ^2/ndf of 3.8/4 to the RMS average of the three models. The shaded boxes represent the uncertainty based on the three model calculations.

β is calculated in 4π space and has a flat mass distribution. It converts the number of muon pairs from oscillation into all B meson pairs. The value of β is 0.22 ± 0.01 which is the calculated RMS value from the three model simulations described above. The error on β is the standard deviation of the three model calculations which represents the model-dependent uncertainty. $\alpha(m)$ and β are applied to the differential cross section and the result is shown in Figure 5.4. Figure 5.5 shows the differential cross section fitted by an exponential $e^{(p_0 + p_1 * \text{mass})}$ that results in a total cross section of $d\sigma_{b\bar{b} \rightarrow \mu\mu}/dy = 0.37 \pm 0.02$ nb. The differential cross section including systematic uncertainties from Chapter 4, represented as one standard deviation, is shown in Figure 5.6, and amount to, $d\sigma_{b\bar{b} \rightarrow \mu\mu}/dy = 0.37 \pm 0.02(\text{stat}) \pm 0.05(\text{syst})$ nb.

5.1.2 Event Rate dependence

We also studied the BBC event rate effect on the mass dependent differential cross section. We compared the differential cross sections for the two data sets, divided based on their BBC

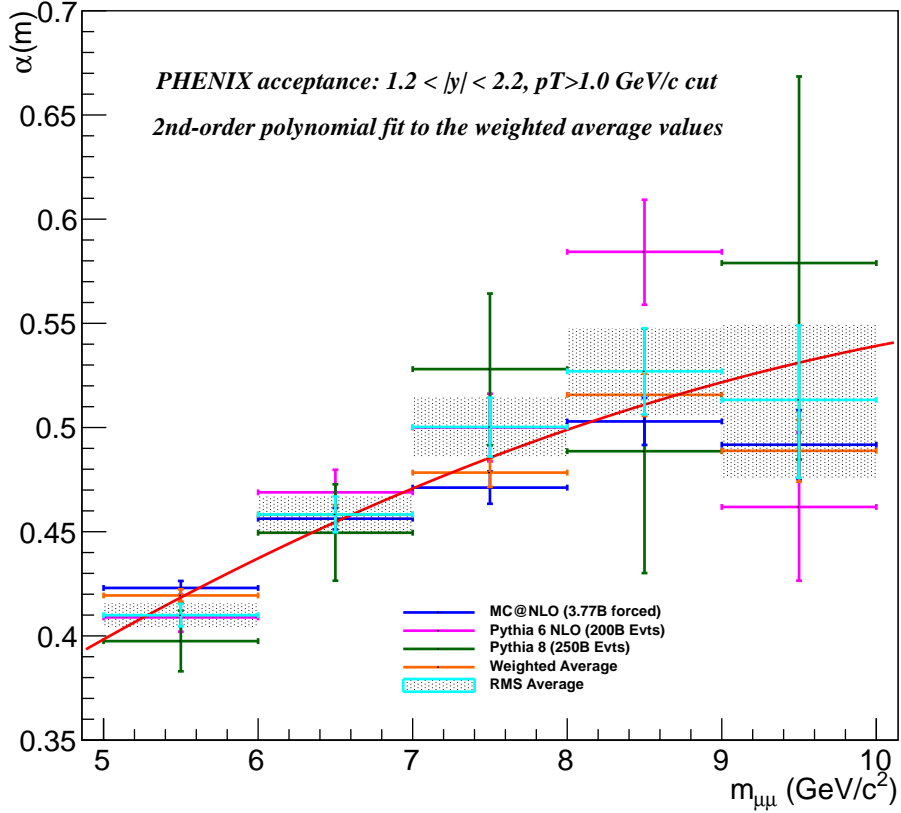


Figure 5.3: Fraction of like-sign dimuons from B^0 meson oscillation ($\alpha(m)$) from MC@NLO (blue points), PYTHIA 6 (magenta points) and PYTHIA 8 (green points) within the PHENIX Muon Arms acceptance. Cyan data points are the RMS average of the three model calculations. The shaded boxes are the associated errors based on the three model calculations. The red curve is a second-order polynomial fit to the RMS data points.

event rates, as described in Section 4.4. The results of this study are shown in Figure 5.7 and the data samples seem to be consistent within uncertainties. However, to measure the level of consistency, we use the following:

$$\delta = \frac{X(H) - X(L)}{\sqrt{\sigma_H^2 - \sigma_L^2}} \quad (5.6)$$

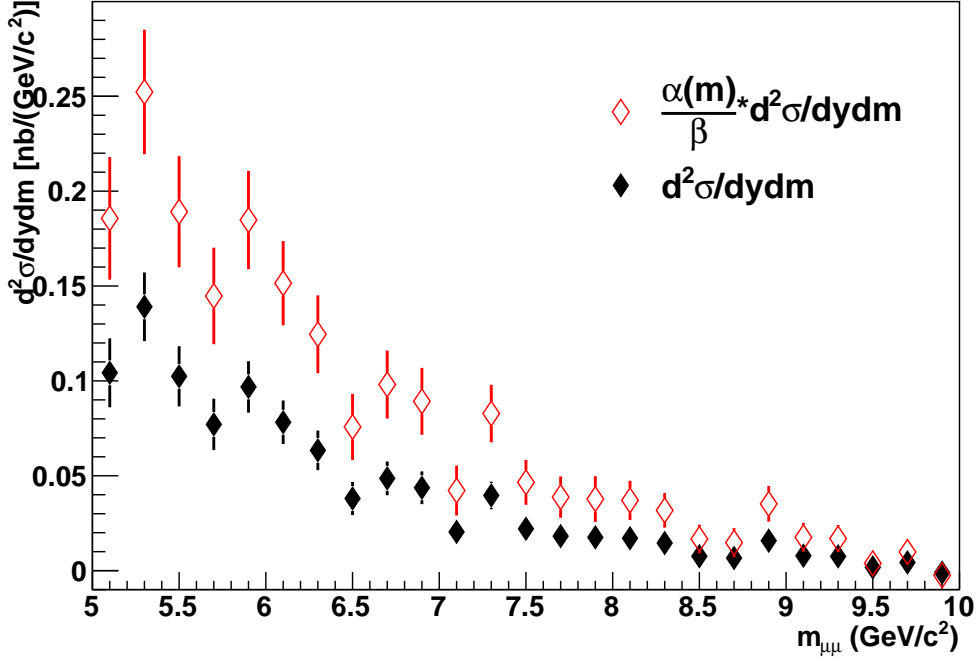


Figure 5.4: The differential cross section multiplied by $\alpha(m)/\beta$ (open red diamonds) compared to the differential cross section before multiplying by $\alpha(m)/\beta$ (black diamonds).

where $X(H/L)$ stands for $d^2\sigma/dydm$ for high/low rate data set. The results are shown in Figure 5.8. The statistical box shows that the mean of the distribution is $(0.2 \pm 0.1)\sigma$ from zero with a width of 0.8σ indicating that within the statistical uncertainties there is no observed effect.

5.1.3 $\Delta\phi$ Dependence

The dimuon $\Delta\phi$ dependent differential cross section is calculated according to Equations 5.1 and 5.2 using the yield in Figure 3.34 and the result is shown in the left panel of Figure 5.9. The differential cross section at this point still includes the hadronic background so the right panel of Figure 5.9 shows the dimuon $\Delta\phi$ dependent differential cross section after

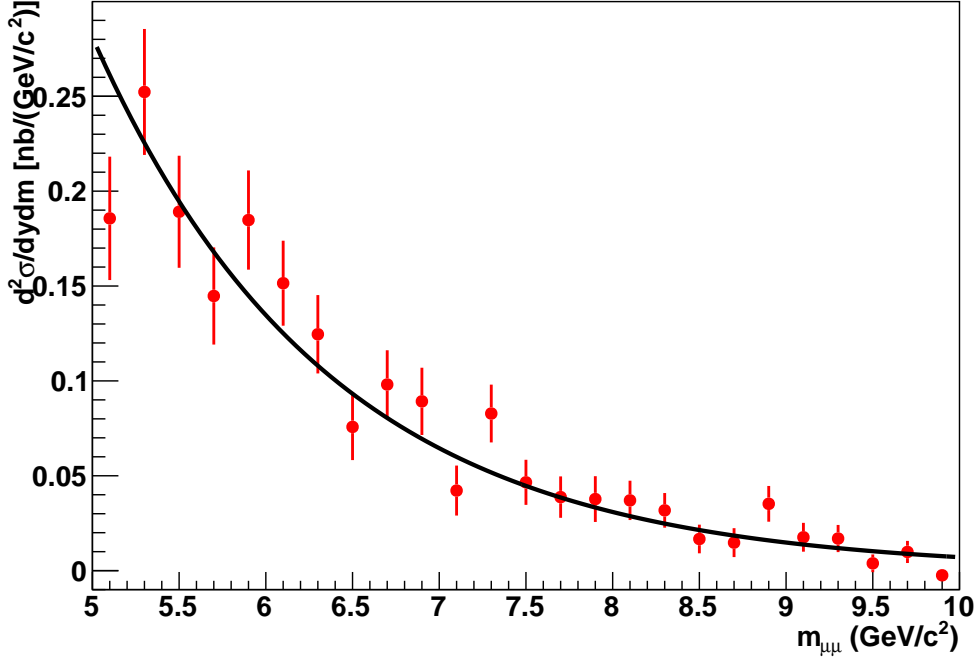


Figure 5.5: The differential cross section multiplied by $\alpha(m)/\beta$ fitted by an exponential to extract the total cross section.

subtraction of the hadronic background.

5.2 Total Cross Section

To extrapolate from the differential cross section of dimuons for $b\bar{b}$ decay to the total $b\bar{b}$ cross section the differential cross section is scaled by the ratio of B pairs that decay to dimuons through the primary-primary decay channel within the measured region to those over the entire kinematic range. This method is similar to that use in Ref. [44]. The total cross section is extrapolated and corrected for the semi-leptonic branching ratio in the following

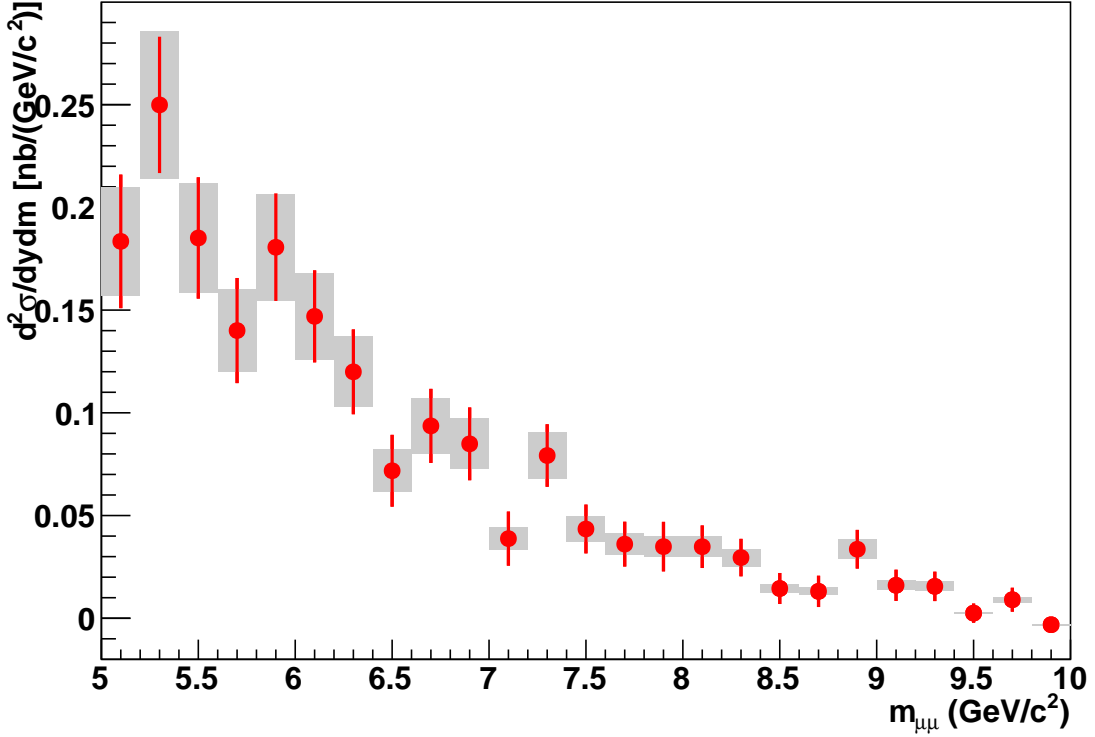


Figure 5.6: The differential cross section as a function of dimuon mass. The shaded boxes show the associated systematic uncertainties.

way:

$$\sigma_{b\bar{b}} = \frac{d\sigma_{b\bar{b} \rightarrow \mu\mu}}{dy} \times \frac{1}{scale} \times \frac{1}{(BR_{B \rightarrow \mu})^2} \quad (5.7)$$

where $BR_{b\bar{b} \rightarrow \mu\mu}/dy$ is the branching ratio of B to muon through the primary decay channel ($=10.95\%$), and $scale$, defned as:

$$scale = \frac{b\bar{b} \rightarrow \mu\mu(1.2 < |y| < 2.2; 5 < m_{\mu\mu} < 10)}{b\bar{b} \rightarrow \mu\mu(all)}, \quad (5.8)$$

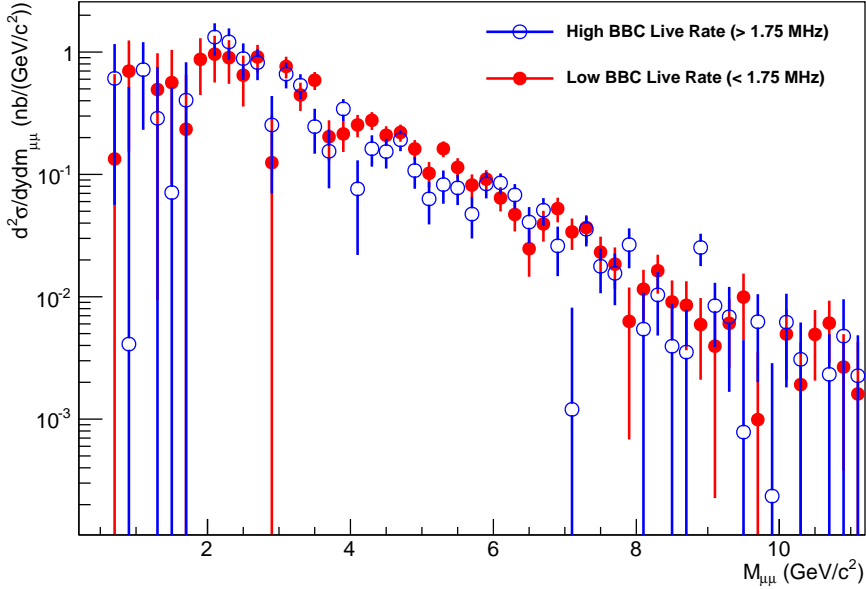


Figure 5.7: The differential cross section as a function of dimuon mass for the high (empty blue circles) and low (solid red circles) rates.

is used to convert from the visible kinematic region to full phase space. The scale factor is determined from PYTHIA and MC@NLO simulations. In this analysis, we only measured the dimuons with mass between 5 and 10 GeV/c^2 where both muons must fall within the same muon arm rapidity acceptance ($-2.2 < y < -1.2$ or $1.2 < y < 2.2$). The simulations show that of the $B\bar{B}$ pairs that decay to dimuons through the primary-primary decay channel, only 0.21% fall within the measured kinematic region although they do cover a substantial part of the rapidity range. The total cross section after applying the *scale* factor is $14.9 \pm 0.7 \mu\text{b}$ and is shown against pQCD theory, alongside other world data, in Figure 5.10.

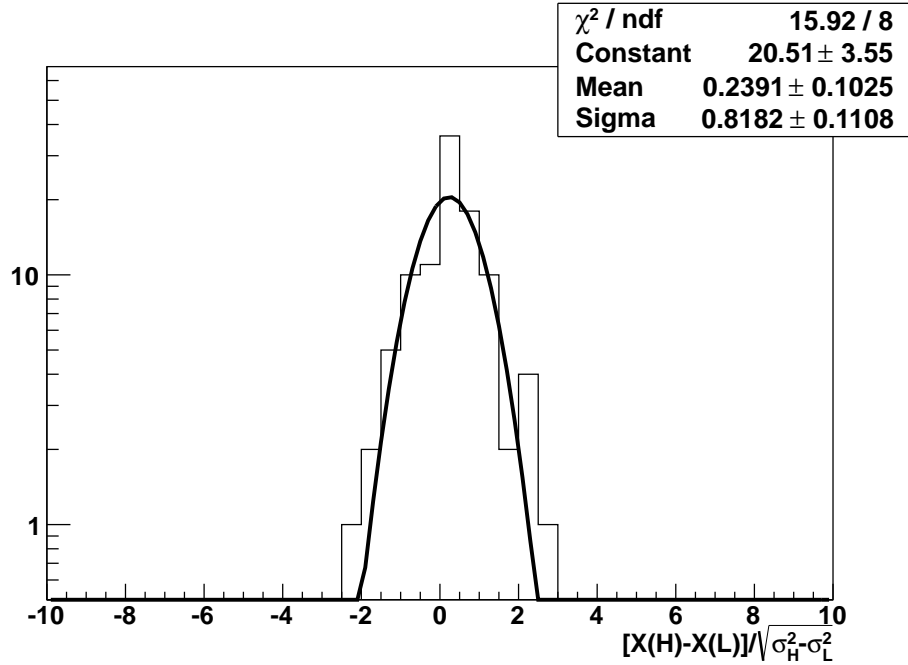


Figure 5.8: The difference between the differential cross sections of the high and low rate data sets.

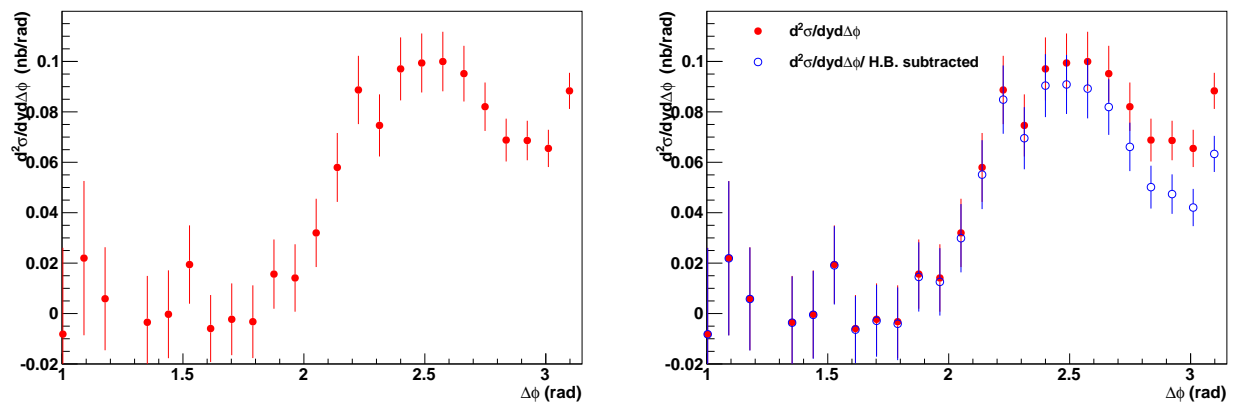


Figure 5.9: Left: The dimuon $\Delta\phi$ dependent differential cross section before subtracting the hadronic background. Right: The dimuon $\Delta\phi$ dependent differential cross section before (solid red circles) and after (empty blue circles) subtracting the hadronic background.

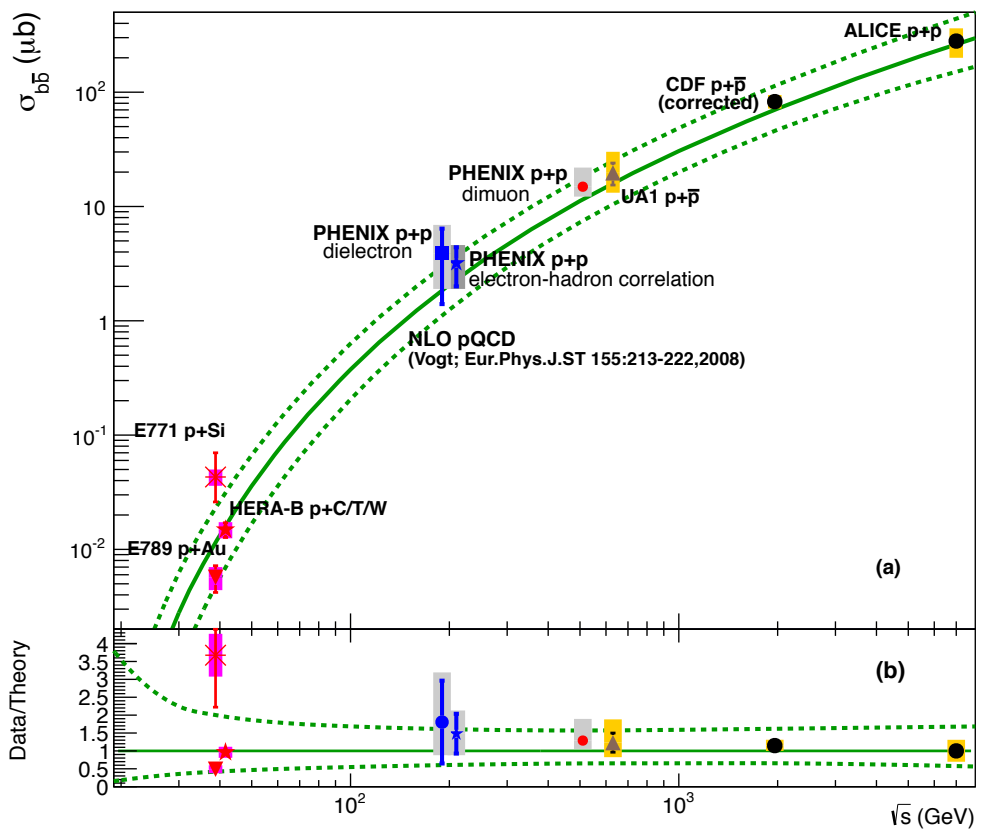


Figure 5.10: Panel a shows world data of the total bottom cross section shown alongside pQCD calculation. Panel b shows the ratio of the measurements to the pQCD calculation [5, 10–17].

6

SUMMARY

We measured $d^2\sigma_{b\bar{b}\rightarrow\mu\mu}/dydm$, $d^2\sigma_{b\bar{b}\rightarrow\mu^\pm\mu^\pm}/dyd\Delta\phi$, $d\sigma_{b\bar{b}\rightarrow\mu\mu}/dy$ and, ultimately the total $\sigma_{b\bar{b}}$ at $\sqrt{s} = 510$ GeV. This was accomplished through the like-sign dimuon decay channel with the PHENIX detectors. By taking advantage of the kinematics of the like-sign pairs in the high mass region, we are able to separate out the open bottom signal from B^0 meson oscillation. The like-sign signal is void of backgrounds from quarkonia and Drell-Yan pairs making high mass like-sign pairs a powerful method to extract the open bottom signal. The total cross section is $\sigma_{tot,b\bar{b}} = 14.9 \pm 0.7(stat) \pm 2.0(type\ B\ sys.) \pm 3.4(type\ C\ sys.)$ [μb]. This is in agreement with pQCD calculations, $\sigma_{tot,b\bar{b}} = 11.2_{-3.9}^{+6.4}$ [μb] (at $\sqrt{s} = 500$ GeV), within the uncertainties. The angular correlations, $\Delta\phi$, of the dimuon pairs in the $5-10$ GeV/c^2 mass region have also been measured. The production mechanisms are being probed by comparing the individual contributions in PYTHIA simulation to the measured angular correlations.

These measurements, as well as those at $\sqrt{s} = 200$ GeV [24] will help constrain pQCD calculations. This method can be directly applicable to heavy ion collisions. This cross section measurement serves as a baseline to investigate the effects of CNM (in small asymmetric collisions) and to study the HNM effects (in larger collision systems) on bottom quark production. This will provide further insights into the QGP and the universe.

Appendices

A Kinematics

Here is an explanation of the kinematic variables used through out this thesis.

1 *Transverse Momentum, p_T*

p_T is the momentum components in the x-y plane and is in units of GeV/c . This is a Lorentz invariant quantity.

$$p_T = \sqrt{p_x^2 + p_y^2} \quad (1)$$

2 *Invariant Mass, m*

In the case of this thesis, m is the mass of the two particle (dimuon) system and is in units of $\text{GeV}c^2$. The mass of the muon is $m_\mu = 0.106 \text{ GeV}/c^2$. This is also a Lorentz invariant quantity.

$$m_{\mu\mu} = \sqrt{2(m_\mu^2 + E_1 E_2 - \vec{p}_1 \cdot \vec{p}_2)} \quad (2)$$

3 *Rapidity, y and Pseudorapidity, η*

y is defined as:

$$y = \frac{1}{2} \ln \left(\frac{E + p_z}{E - p_z} \right) \quad (3)$$

η is defined as:

$$\eta = -\ln \left[\tan \left(\frac{\theta}{2} \right) \right] \quad (4)$$

Where θ is the angle the particle trajectory makes in reference to the $+z$ -axis. As speeds approach the speed of light, c , and with relatively small masses $y \approx \eta$. See Figure A.1.

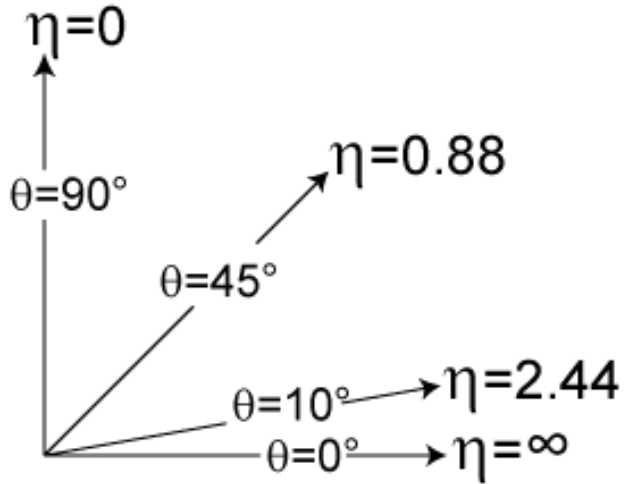


Figure A.1: Pseudorapidity, η . $\eta = 0$ is in the $+y$ -axis direction at PHENIX and the beam pipe is along $\eta \rightarrow \infty$ [18].

B PHENIX CVS code locations

offline/AnalysisTrain/pat/macro/Runpp2013lvm.C

offline/AnalysisTrain/picoDSTobject

Using the **((MUIDLL1_N2D||S2D)|(N1D&&N2D)&&BBCLL1(noVtx))** trigger.

C List of Runs Used

386775 386776 386777 386825 386826 386828 386829 386830 386833 386838 386839 386841
386843 386844 386881 386882 386883 386884 386941 386942 386943 386946 386947 386948
386951 386952 387070 387077 387078 387139 387227 387247 387290 387292 387414 387430
387431 387433 387436 387539 387541 387543 387550 387560 387566 387571 387649 387651
387658 387659 387660 387661 387668 387669 387670 387672 387673 387674 387676 387710
387719 387724 387725 387784 387785 387787 387790 387792 387793 387802 387803 387808
387809 387963 387967 387968 388019 388021 388022 388023 388038 388039 388042 388047
388050 388051 388052 388261 388263 388265 388266 388404 388405 388495 388536 388539
388540 388541 388547 388548 388632 388633 388634 388638 388640 388692 388693 388694
388697 388698 388699 388700 388720 388721 388724 388726 388743 388837 388838 388840
388859 388860 388862 388863 388865 388866 388978 388980 388981 388984 388985 388986
389119 389120 389121 389123 389124 389126 389320 389322 389323 389324 389326 389327
389334 389335 389336 389338 389339 389424 389434 389436 389444 389445 389446 389471
389560 389570 389571 389573 389575 389577 389578 389579 389586 389587 389589 389590
389702 389703 389752 389756 389758 389759 389761 389762 389766 389767 389768 390510
390518 390519 390537 390538 390540 390541 390542 390615 390667 390669 390670 390674
390942 390943 390944 390954 390958 390959 390963 390964 390965 391036 391041 391047
391051 391169 391170 391174 391177 391291 391371 391374 391377 391442 391445 391446
391465 391466 391470 391471 391566 391569 391579 391583 391588 391722 391813 391815
391860 391861 391873 391875 391876 391966 391968 391969 391982 392015 392027 392028

392226 392267 392292 392293 392297 392299 392359 392415 392418 392420 392422 392428
392429 392540 392541 392542 392545 392548 392811 392814 392818 392819 392821 392838
392840 392842 392846 392848 392922 392926 392928 392934 392942 392947 393051 393054
393056 393061 393062 393066 393067 393164 393167 393175 393176 393177 393178 393180
393341 393342 393343 393345 393349 393351 393458 393461 393462 393464 393469 393471
393478 393481 393483 393484 393485 393486 393487 393529 393530 393531 393534 393574
393575 393576 393577 393581 393627 393677 393795 393798 393805 393809 393810 393883
393885 393888 393890 393891 393898 393901 393905 394002 394003 394004 394005 394048
394049 394050 394054 394055 394057 394060 394061 394062 394065 394066 394067 394068
394069 394072 394272 394388 394389 394391 394398 394400 394402 394417 394420 394421
394423 394526 394538 394539 394676 394679 394682 394683 394684 394698 394700 394701
394702 394704 394739 394742 394744 394745 394750 394962 394980 395099 395228 395230
395231 395233 395238 395239 395244 395389 395396 395397 395402 395405 395407 395408
395411 395412 395413 395420 395432 395526 395527 395544 395545 395550 395551 395553
395587 395588 395590 395591 395592 395594 395595 395599 395639 395640 395641 395643
395645 395646 395731 395732 395769 395771 395775 395777 395808 395809 395811 395813
395816 395817 395882 395884 395899 395901 395907 395908 395939 395940 396048 396049
396054 396056 396058 396065 396066 396073 396074 396075 396268 396274 396277 396279
396280 396363 396366 396412 396415 396418 396433 396434 396437 396438 396440 396544
396545 396546 396549 396552 396560 396612 396614 396616 396617 396618 396619 396627
396628 396629 396630 396631 396633 396634 396635 396636 396677 396678 396681 396682

396683 396684 396760 396761 396764 396765 396766 396767 396768 396785 396790 396799
396802 396803 396887 396889 396891 396910 396914 396919 396921 396993 396994 397000
397049 397066 397069 397070 397176 397178 397181 397184 397201 397208 397290 397291
397294 397297 397313 397315 397317 397318 397319 397322 397401 397402 397431 397432
397433 397434 397437 397438 397511 397513 397517 397519 397524 397525 397526 397527
397531 397532 397534 397535 397581 397587 397588 397589 397692 397700 397705 397708
397710 397711 397712 397715 397735 397738 397866 397933 397934 397938 397989 397990
398005 398007 398009 398011 398013 398014 398018 398019 398020 398026 398119 398122
398123 398124 398125 398130 398133 398137 398138 398142 398144 398145 398146 398147
398148 398149

D PYTHIA 6 Tune A Hadron Simulation Set Up

Table D.1: PYTHIA Tune A configuration used to extract hadronic contributions from MB simulation

roots	510	
proj	p	
targ	p	
frame	cms	
msel	1	Turn on all QCD processes
mtsp	51 7	CTEQ5L, leading order PDF
parp	67 4.0	Set hard scattering scale μ^2
parp	82 2.0	Turn off p_T for multiparticle interactions
parp	84 0.4	Radius of core Gaussian matter
parp	85 0.9	Probability two gluons are produced with colors connected to nearest neighbors
parp	86 0.95	Probability two gluons are produced with PARP(85) conditions or closed loop
parp	89 1800	Reference energy scale of the turn off p_T
parp	90 0.25	Energy dependence of the turn off p_T
parp	91 1.5	Primordial k_T Gaussian width
ckin	3 1.5	Lower cutoff on \hat{p}_\perp

E PYTHIA 8 MB Simulation Set Up

The simulation ran 250 Billion MB events and recorded single muon particles with their ancestral record. `SoftQCD:nonDiffractive = on`

`Beams:idA = 2212 // p`

`Beams:idB = 2212 // p`

`Beams:eCM = 500. // energy`

`SigmaProcess:Kfactor = 3.4 // K factor`

`SigmaProcess:renormScale1 = 1 // Set Q2 scale(s) = sHat`

`SigmaProcess:renormScale2 = 4 //default value for 2 --> 1 processes`

`PartonLevel:FSR = off //switch off final-state radiation`

`PDF:pSet = 7 //PDF pSet = 7 --> CTEQ6L1 NLO`

`BeamRemnants:primordialKT = on //set kT values`

`BeamRemnants:primordialKTsoft = 1.5`

`BeamRemnants:primordialKThard = 1.5`

`BeamRemnants:halfScaleForKT = 1.5`

`BeamRemnants:halfMassForKT = 1.5`

`4m0 = 1.275 // c quark mass`

`5m0 = 4.18 // b quark mass`

F PYTHIA 6 J/ψ Embedding Simulation Set Up

Table F.1: PYTHIA 6 J/ψ configuration file used for the $A\epsilon$ embedding study.

```

roots 510
proj  p
targ  p
frame cms
msel  0           Turn on all processes manually
msub  86  1        $g + g \rightarrow J/\psi$ 
pmas  4   1       1.25 charm quark mass GeV/cs
mdme  858 1       0    $J/\psi \rightarrow ee$  turned off
mdme  859 1       1    $J/\psi \rightarrow \mu\mu$  turned on
mdme  860 1       0    $J/\psi \rightarrow \text{random}$  turned off
mstp  51  10041   CTEQ6LL
mstp  52  2       Use LHAPDF
parp  92  2.2     set intrinsic  $k_T$  value

```

REFERENCES

- [1] Wikipedia The Free Encyclopedia. Standard model of elementary particles. Online, May 2018.
- [2] Wikipedia The Free Encyclopedia. Weak decay. Online, May 2018.
- [3] Particle Data Group. The particle adventure: The fundamentals of matter and force. Online, May 2018.
- [4] Brookhaven National Lab. How low can rhic go? Online, May 2018.
- [5] R Vogt. The total charm cross section. *European Physics J Special Topics*, 155:213–22, 2008.
- [6] L. Patel. *Cross Section of Bottom Quark Production in $p + p$ Collisions at $\sqrt{s} = 500$ GeV Using Like-Sign Dimuons at PHENIX*. PhD thesis, Georgia State University, 2013.
- [7] U.S. Department of Energy. User facilities: Relativistic heavy ion collier (rhic). Online, 2018 May.
- [8] Brookhaven National Lab. Run overview of the relativistic heavy ion collider. Online, 2018 May.
- [9] Hideyuki Oide. *Measurement of longitudinal spin asymmetry in production of muons from W/Z boson decays in polarized $p+p$ collisions at $\sqrt{s} = 500$ GeV with the PHENIX detector at RHIC*. PhD thesis, The University of Tokyo, 2012.

- [10] Jansen D M and et al. Measurement of the bottom-quark production cross section in 800 gev/c proton-gold collisions. *Physics Review Letters*, 74:3118–21, 1995.
- [11] T Alexopoulos and et al. (E771 Collabortaion). Measurement of the $b\bar{b}$ cross section in 800 gev/c proton-silicon interactions. *Physics Review Letters*, 82:41–4, 1999.
- [12] Abt I and et al. (E771 Collabortaion). Improved measuremnt of the $b\bar{b}$ cross section in 920 gev fixed-target proton-nucleus collisions. *Physics Review D*, 73:052005–22, 2006.
- [13] A Adare and et al. (The PHENIX Collaboration). Measurement of bottom versus charm as a function of transverse momentum with electron-hadron correlations in $p + p$ collisions at $\sqrt{s} = 200$ gev. *Physics Review Letters*, 103:082002–9, 2009.
- [14] A Adare and et al. (The PHENIX Collaboration). Dilepton mass spectra in $p + p$ collisions at $\sqrt{s} = 200$ gev and the contribution from open charm. *Physics Letters B*, 670:313–20, 2009.
- [15] C. Albajar and et al. (UA1 Collaboration). Beauty production at cern in $p\bar{p}$ collider. *Physics Letters B*, 256:121–8, 1991.
- [16] D. Acosta and et al. (CDF Collaboration). Measurement of the j/ψ meson b -hadron production cross section in $p\bar{p}$ collisions at $\sqrt{s} = 1960$ gev. *Physics Review D*, 71, 2005.
- [17] Abelev B and et al. (ALICE). 2013 measurement of electrons from beauty hadron decays in pp collisions at $\sqrt{s} = 7$ tev. *Physics Letters B*, pages 13–23, 2013.
- [18] The Free Encyclopedia Wikipedia. Pseudorapidity. Online, June 2018.

- [19] O. W. Greenberg. Spin and unitary-spin independence in a paraquark model of baryons and mesons. *Physics Review Letters*, 13(20), November 1964.
- [20] P. W. Anderson. Plasmons, gauge invariance, and mass. *Physical Review*, 130(1), April 1963.
- [21] Albert Einstein. Theory of relativity and the application of this theory in astronomy. *Preussische Akademie der Wissenschaften*, November 1915.
- [22] The PHENIX Collaboration. Measurements of $\mu\mu$ pairs from open heavy flavor and drell-yan in $p + p$ collisions at $\sqrt{s} = 200$ gev. *arXiv:1805.02448v1 [hep-ex]*, May 2018.
- [23] Aaij R and et al. (LHCb). Measurement of b meson production cross-sections in proton-proton collisions at $\sqrt{s} = 7$ tev. *Journal of High Energy Physics*, 117, 2013.
- [24] The PHENIX Colaboration. Correlations of $\mu\mu$, $e\mu$ and ee pairs in $p + p$ collisions at $\sqrt{s} = 200$ gev and implications for $c\bar{c}$ and $b\bar{b}$ production mechanisms. *arXiv:1805.04075 [hep-ex]*, May 2018.
- [25] C. Patrignani and et al. (Particle Data Group). Ckm quark-mixing matrix. *Chin. Phys. C* 40 100001, 2016 and 2017.
- [26] Makoto Kobayashi and Toshihide Maskawa. Cp-violation in the renormalizable theory of weak interaction. *Progress of Theoretical Physics*, 49(2), February 1973.
- [27] S. W. Herb and et al. (E288). Observation of a dimuon resonance at 9.5 gev in 400-gev proton-nucleus collisions. *Physics Review Letters*, 39:252–255, August 1977.

- [28] C. Patrignani and et al. (Particle Data Group). Production and decay of b -flavored hadrons. *Chin. Phys. C* 40 100001, 2016 and 2017.
- [29] C. Patrignani and et al. (Particle Data Group). $b^0 - \bar{B}^0$ mixing. *Chin. Phys. C* 40 100001, 2016 and 2017.
- [30] K. Adcox and et al. (The PHENIX Collaboration). Formation of dense partonic matter in relativistic nucleus–nucleus collisions at rhic: Experimental evaluation by the phenix collaboration. *Nuclear Physics A*, 757(1):184 – 283, 2005. First Three Years of Operation of RHIC.
- [31] C. Patrignani and et al. (Particle Data Group). 2017 review of particle physics. *Chin, Phys C*, 40(100001), 2016-2017.
- [32] Torbjörn Sjöstrand, Stephen Mrenna, and Peter Skands. Pythia 6.4 physics and manual. *Journal of High Energy Physics*, 2006, May 2006.
- [33] Torbjörn Sjöstrand, Stephen Mrenna, and Peter Skands. A brief introduction to pythia 8.1. *Computer Physics Communications*, 178, June 2008.
- [34] Stefano Frixione, Fabian Stoeckli, Paolo Torrielli, Bryan R. Webber, and Chris D. White. The mc@nlo 4.0 event generator. *arXiv:1010.0819[hep-ph]*, October 2010.
- [35] D. Barton and et al. Electron beam ion source pre-injection project (ebis) conceptual design report. Technical report, Brookhaven National Lab: Collider-Accelerator Dept., September 2005.

- [36] IEEE Service Center. *Heavy ion program at BNL: AGS, RHIC*, 1987.
- [37] International Particle Accelerator Conference. *RHIC polarized proton operation for 2013*, Shanghai, China, 2013.
- [38] H. Akikawa and et al. (The PHENIX Collaboration). Phenix muon arms. *Nuclear Instruments and Methods in Physics Research*, 499:537–548, March 2003.
- [39] C. Albajar and other. A study of the general characteristics of proton-antiproton collisions at $\sqrt{s} = 0.2$ to 0.9 TeV. *Nuclear Physics B*, 335:261, 1990.
- [40] Uncertainty of measurement - part 3: Guide to the expression of uncertainty in measurement. Online, 2008.
- [41] Stefano Frixione and Bryan R. Webber. Matching NLO QCD computations and parton shower simulations. *Journal of High Energy Physics*, 2002:029, 2002.
- [42] Stefano Frixione, Paolo Nason, and Bryan R. Webber. Matching NLO QCD and parton showers in heavy flavour production. *Journal of High Energy Physics*, 2003:007, 2003.
- [43] A Adare and et al. (The PHENIX Collaboration). Cross section and parity-violating spin asymmetries of w^\pm boson production in polarized $p + p$ collisions at $\sqrt{s} = 500$ gev. *Physics Review Letters*, 106(062001), 2011.
- [44] The ZEUS collaboration. Measurement of beauty production from dimuon events at HERA. *Journal of High Energy Physics*, 2009:032, 2009.